The Dissertation Committee for Christopher Michael Mirabito
certifies that this is the approved version of the following dissertation:

Analysis, Implementation, and Verification of a Discontinuous Galerkin Method for Prediction of Storm Surges and Coastal Deformation

Committee:

Clint N. Dawson, Supervisor

Leszek F. Demkowicz

Irene M. Gamba

Omar Ghattas

Wonsuck Kim

Analysis, Implementation, and Verification of a Discontinuous Galerkin Method for Prediction of Storm Surges and Coastal Deformation

by

Christopher Michael Mirabito, B.S. Math., M.S. C.A.M.

DISSERTATION

Presented to the Faculty of the Graduate School of

The University of Texas at Austin

in Partial Fulfillment

of the Requirements

for the Degree of

DOCTOR OF PHILOSOPHY

THE UNIVERSITY OF TEXAS AT AUSTIN

August 2011

To my family, with pride, gratitude, and love.

Acknowledgments

This dissertation is the product of five years of study, thought, persistence, and determination. It represents the culmination of my research efforts during this time. Computational science, engineering, and mathematics has brought me much happiness and joy, and has truly awakened me to the possibilities of interdisciplinary research. None of this would have been possible without the help of many people, who I wish to thank below.

First, I would like to thank my adviser, Clint Dawson, first for introducing me to the subject matter of this dissertation, and then for directing and guiding me once I joined his research group. His assistance with navigating the vast jungle of literature and technical details is appreciated, and will not be forgotten. His unwavering support and incredible patience were always on full display during our countless meetings, which helped to motivate me throughout my time here. Certainly, without his help, this dissertation would not have come to fruition.

I also want to thank the committee members, namely Leszek Demkowicz, Irene Gamba, Omar Ghattas, and Wonsuck Kim, for graciously volunteering their time to meet with me both before and during candidacy, suggesting improvements to this document (and correcting errors!), offering constructive advice and criticism, and helping me locate additional reference material. They encouraged me to interpret my research problem from several viewpoints, which has proven valuable.

Throughout my studies, I have benefited from discussions with numer-

ous other investigators, both within and outside the Institute. Ethan Kubatko offered (much needed) help in understanding the ADCIRC model implementation, especially during the early stages of work. Corey Trahan, Craig Michoski, Jennifer Proft, and Troy Butler each provided me with some additional perspective on the problem at hand, which helped reinforce my understanding (and resolve any misunderstanding) of the background material. My fellow students (*friends*, really) helped me grasp the analysis and results from the literature, proofread some of my work, taught me miscellaneous computing tricks, or simply offered encouragement; I will sorely miss them all after leaving Austin.

I am very grateful to the Institute for Computational Engineering and Sciences (ICES), as well as the University of Texas, for giving me the opportunity to work with such kind, thoughtful, and well-respected researchers. Their support has made both my graduate career and my stay in Austin an unforgettable one.

Lastly, and perhaps most of all, I would like to thank my family for their unconditional love and support they have given me throughout all these years. Their encouraging me from a young age to pursue a career in science has been the ultimate inspiration. It is my sincerest hope that this work will come to symbolize the realization of not only my hopes and dreams, but theirs as well.

Christopher Michael Mirabito

The University of Texas at Austin
August 2011

Analysis, Implementation, and Verification of a Discontinuous Galerkin Method for Prediction of Storm Surges and Coastal Deformation

Publication No. _____

Christopher Michael Mirabito, Ph.D.
The University of Texas at Austin, 2011

Supervisor: Clint N. Dawson

Storm surge, the pileup of seawater occurring as a result of high surface stresses and strong currents generated by extreme storm events such as hurricanes, is known to cause greater loss of life than these storms' associated winds. For example, inland flooding from the storm surge along the Gulf Coast during Hurricane Katrina killed hundreds of people. Previous storms produced even larger death tolls. Simultaneously, dune, barrier island, and channel erosion taking place during a hurricane leads to the removal of major flow controls, which significantly affects inland inundation. Also, excessive sea bed scouring around pilings can compromise the structural integrity of bridges, levees, piers, and buildings.

Modeling these processes requires tightly coupling a bed morphology equation to the shallow water equations (SWE). Discontinuous Galerkin finite element methods (DGFEMs) are a natural choice for modeling this coupled

system, given the need to solve these problems on large, complicated, unstructured computational meshes, as well as the desire to implement *hp*-adaptivity for capturing the dynamic features of the solution.

Comprehensive modeling of these processes in the coastal zone presents several challenges and open questions. Most existing hydrodynamic models use a fixed-bed approach; the bottom is not allowed to evolve in response to the fluid motion. With respect to movable-bed models, there is no single, generally accepted mathematical model in use. Numerical challenges include coupling models of processes that exhibit disparate time scales during fair weather, but possibly similar time scales during intense storms.

The main goals of this dissertation include implementing a robust, efficient, tightly-coupled morphological model using the local discontinuous Galerkin (LDG) method within the existing Advanced Circulation (ADCIRC) modeling framework, performing systematic code and model verification (using test cases with known solutions, proven convergence rates, or well-documented physical behavior), analyzing the stability and accuracy of the implemented numerical scheme by way of *a priori* error estimates, and ultimately laying some of the necessary groundwork needed to simultaneously model storm surges and bed morphodynamics during extreme storm events.

Table of Contents

List of Tables

List of Figures

Chapter 1

Introduction

1.1 Background, Motivation, and Challenges

Modeling fluid flow and transport in coastal waters requires a detailed knowledge of winds, waves, currents, sediment transport, and, ultimately, the resulting morphological changes in the seabed that occur as a result of these processes. The erosion and deposition of bed sediment can have a major detrimental impact on the coastal population, infrastructure, and environment. For example, the US Army Corps of Engineers (USACE) maintains more than 12,000 miles of waterways for transportation, which carry approximately one-sixth of US inter-city freight [183]. Maintenance of these waterways through dredging and backfilling operations represents a significant cost to the USACE as well as other agencies and industries. As another example, excessive seabed scouring around pilings can compromise the structural integrity of bridges, levees, piers, and buildings; scouring has been cited as one of the most common causes of bridge failures in coastal regions [123]. Also, dune, barrier island, and channel erosion during a hurricane leads to the removal of major flow controls, which significantly affects inland inundation. In addition to these infrastructure-related issues, there exists a host of environmental concerns, such as beach erosion and the transport of pollutants with sediment, which may act as a source or sink for contaminants depending on the surrounding physico-chemical conditions [45].

Collectively, the various flow and transport processes that lead to morphological changes in the sea bed form an interdependent physical system in which the fluid motion, due to both waves and currents, drives the transport of sediment, which dictates the evolution of the sea bed. In turn, the fluid motion itself is then directly affected by the morphological changes in the bed that it induces. Comprehensive modeling of these processes in the coastal zone presents several challenges and open questions. Most existing hydrodynamic models use a fixed-bed approach; the fluid-bed interface is not allowed to evolve in response to the fluid motion. With respect to movable-bed models, there is no single, generally accepted mathematical model in use, with descriptions of the fluid-bed interface region varying from simple single interface models to more complex three-phase approaches that consist of fluid, fluid-sediment, and sediment phases; see, for example, [74]. Once an appropriate mathematical model has been formulated, there exists the numerical challenge of coupling models of various processes that exhibit disparate time scales—both within the fluid motion itself and between the fluid and bed motion. The evolution of the bed is typically on a much slower time scale compared to even the slowest time scale of the fluid motion; a situation where this may not be the case is during an extreme event, such as a hurricane.

In this dissertation, the focus is on the coupling of shallow water hydrodynamics with sediment transport described as bed load, and the application of an *hp* Runge–Kutta local discontinuous Galerkin (RKLDG) approximation to this coupled system. The mathematical model under consideration consists of the depth-averaged (two-dimensional) shallow water equations (SWE) and the well-known Exner equation [70], which describes the bed morphology. The models are coupled in the sense that the sediment flux depends

on the current, while the transport of sediment induces dynamic bathymetry, which affects the water depth. In addition, the fact that bathymetry is now an unknown in the model rather than a known fixed quantity gives rise to a nonconservative product in the momentum equations, which requires special treatment.

The RKDG method is an extension of finite volume methods (FVMs) which allows for arbitrary order of approximation in space and is applicable to general unstructured meshes. A number of researchers have studied FVMs for circulation/sediment transport/bed morphology models of various levels of complexity, in one and two space dimensions [25, 27, 32, 74, 88, 89, 123, 124, 164]. These papers shed light on approaches for coupling the equations in both space and time, including the development of numerical fluxes appropriate for DG discretizations.

Recently, Tassi *et al.* [172] have examined river bed evolution in shallow water flow using the RKDG method. The DG spatial discretization that is used is an extended approach developed by Rhebergen *et al.* [153] to handle the nonconservative product that is introduced when coupling the Exner equation to the SWE. This approach is followed here, but the focus is on the development, analysis, and verification of the RKLDG method in both h (mesh spacing) and p (polynomial order), and on the application of the model to a number of coastal engineering problems, emphasizing the effects of h- and p-refinement in these examples.

1.2 A Literary and Historical Review

In this section, a brief review of previous research and results on the subject of shallow water modeling, sediment transport modeling, and discon-

tinuous Galerkin methods is conducted. An attempt has been made to summarize the development of these subjects in chronological order as terms were added to the SWE, as new empirical expressions for the sediment discharge rate were formulated, and as different numerical solution methods were proposed.

1.2.1 Shallow Water Models

The "modern" development of shallow water models has a fairly lengthy history, spanning several centuries. This is because one of their most important applications, namely oceanic tidal modeling and prediction, has attracted the interest of mankind since ancient times. As a result, the earliest developments of shallow water models are closely associated with advances in the study of tides. For an excellent and very comprehensive account on the history of tidal studies, the reader is urged to consult Cartwright [28]. Also, much of the development is tied to advances made in fluid mechanics, and to a lesser extent, turbulence modeling. The connection between these research topics is explained below.

During the Copernican Revolution, numerous theories were proposed by various researchers, including the likes of Galilei, Kepler, and Descartes, to explain the tides. These were largely unscientific in nature, and it was not until 1687 that the first physically consistent account was published [28, 93, 96]. This theory was offered by Newton [137], and was stated as a consequence of his gravitational theory (between the Earth, Moon, and Sun) presented in [136]. This development eventually led to the idea, due primarily to Daniel Bernoulli (1740), of the so-called equilibrium theory of tides, which remained the conventional wisdom on the subject until Laplace (1775) proposed a new

dynamic theory in [56] and expanded upon it in [57]. Of interest here are equations (6), (7), and (9) from [57], which when translated into modern notation read:

$$\frac{\partial \zeta}{\partial t} = -\frac{1}{R\cos\varphi}\left[\frac{\partial}{\partial \varphi}(vH\cos\varphi) + \frac{\partial}{\partial \lambda}(uH)\right], \tag{1.2.1}$$

$$\frac{\partial u}{\partial t} + 2\omega v \sin\varphi = -\frac{g}{R\cos\varphi}\frac{\partial}{\partial \lambda}[\zeta - \delta U - U], \tag{1.2.2}$$

$$\frac{\partial v}{\partial t} - 2\omega u \sin\varphi = -\frac{g}{R}\frac{\partial}{\partial \varphi}[\zeta - \delta U - U], \tag{1.2.3}$$

where ζ is the elevation "above the surface of the sea considered in an equilibrium state that would be reached in the long-term, without the action of the Sun and the Moon"[1], assumed to coincide with $r = R$, the mean radius of the Earth; u and v, the eastward (λ) and northward (φ) velocities, respectively; H, the depth of the seawater column; ω, the mean rotation rate of the Earth; g, the gravitational constant; δU, the potential due to self-attraction and solid Earth tides, and U, the astronomical tide-generating potential.

Equations (1.2.1)–(1.2.3), now known as Laplace's tidal equations, can arguably be considered the earliest, most specialized form of the SWE in spherical coordinates. The momentum equations contain only the Coriolis forcing term[2], gravity term, and tidal potential terms; no advection or friction terms are present [187], although linear friction terms were later added by Laplace.

Meanwhile, Euler (1755) derived the basic laws of incompressible fluid motion and energy using differential forms, introducing a pressure term but

[1] Approximate translation from the original French: "...au-de∫∫us de la ∫urface de la mer con∫idérée dans l'état d'équilibre auquel elle ∫eroit parvenue depuis long-temps, ∫ans l'action du Soleil & de la Lune." [57]

[2] This term was first formulated by d'Alembert (1747), and appears to have been well known prior to the 1792 birth of Coriolis [28].

ignoring friction [68]. A major advance in fluid mechanics, and consequently shallow water models, was achieved by Navier (1822), who additionally considered forces between molecules by appending a stress tensor to Euler's equations [133]. By considering friction, Stokes (1845) formulated the "no-slip" boundary condition and proceeded to re-derive Navier's equations [169]. However, it was Barré de Saint-Venant (1843) who first produced a correct derivation of what would become known as the Navier–Stokes equations for viscous flow [13], identifying viscosity as a multiplying factor of ∇u [90]. Thus, by the middle of the nineteenth century, a vastly improved description of shallow water flow was available.

A link between the three-dimensional Navier–Stokes equations and the SWE was discovered in 1871 by Boussinesq [18] and independently by Barré de Saint-Venant [14]. Boussinesq assumed a constant density in the Navier–Stokes equations (except in the gravity term), and subsequently eliminated the vertical momentum equation after integrating over depth, with the intent of obtaining an approximate solution for a solitary wave [187]. Moreover, he later postulated that when turbulent effects were considered, the resulting stress tensor could be reformulated using an effective turbulent eddy viscosity [19]. This result proved useful in handling the closure problem which occurred when Reynolds, who recognized that viscosity was a controlling factor in eddy formation [150], spatially-averaged the Navier–Stokes equations [151]. Barré de Saint-Venant posed the SWE essentially in their modern form, complete with advection terms, a pressure term, a generic bottom friction term, and diffusion terms with an eddy viscosity. However, the SWE still did not contain stress terms due to wind and short waves; these would not be developed until well into the twentieth century, and even then in a somewhat *ad hoc* manner (see

[76] and [125]).

A separate line of research focused on the development of U in equations (1.2.2) and (1.2.3). Laplace (1776) was among the first to decompose this term into a harmonic series containing three main species. Ferrel (1874) accounted for tidal friction in his expansion, taking into account second-order terms previously neglected by Laplace [72]. He produced a small listing of the dominant tidal constituents. Darwin (1884) listed additional ones, and developed the naming convention (*e.g.*, M_2 and S_2) which is still in use today [50]. Doodson (1921) published a comprehensive listing of nearly 400 constituents [61], although his analysis was based on Brown's (1919) now-obsolete lunar theory [23]. In short, these results allowed the tidal potential term to be conveniently decomposed into series of long-period, diurnal, and semi-diurnal species, with each series being sums of many individual harmonic constituents.

The term δU, which accounts for the self-attraction effect and solid Earth tides, was first expanded as a series by Laplace in the nineteenth century. Love (1911) introduced the coefficients $\mathfrak{h}$ and $\mathfrak{k}$ to the harmonic constituents to account for these effects [28]; the quantity $1 - \mathfrak{h} + \mathfrak{k}$ is sometimes referred to as the Earth tide reduction factor. Henderschott (1981) adopted a constant value for $1 - \mathfrak{h} + \mathfrak{k}$ when distinguishing between the theoretical and observed free surface elevations [84], while Wahr (1981) adopted constituent-specific values (most noticeably in the diurnal species) to account for resonance caused by the Earth's core [28, 188].

It was known since the time of Laplace that except in very simple cases, analytic solutions to the SWE in closed form are not generally available. However, with the advent of the earliest electronic computing systems in the

1940s, solving the 2-D SWE numerically suddenly became tractable. Some early numerical work of note is that of Charney *et al.* (1950) for an atmospheric simulation [34], and Hansen (1956) for a coastal sea model [82]. The former work is also noted for its calling for investigation of the BCs, a problem which remains unresolved [101, 187]; the latter work is notable as an early attempt to numerically predict sea levels.

Most early numerical shallow water models employed finite difference methods (FDMs), based on the available theory and relative ease of implementation. However, it was realized by the end of the 1950s that these schemes were prone to spurious $2h$-oscillations in the solution, h being the maximal cell size. Over the next twenty years, numerous strategies were tried in an attempt to either control or suppress them, with varying degrees of success. According to [1] and [94], some of the strategies utilized included staggered grids, which were used first in [82] and then in [113] and [147], mixed interpolation [173], viscous coefficients [189], nonphysically large bottom friction [145], and finally a reformulation of the SWE as a single wave equation known as the generalized wave continuity equation (GWCE). This latter result was due to Lynch and Gray (1978), who also provided a suite of test cases with exact solutions useful for verifying linearized shallow water models [127].

Beginning in the 1970s, finite element methods (FEMs) gradually displaced FDMs as the numerical scheme of choice for solving the 2-D SWE, partly because of their flexibility in the choice of approximation space and element shape, and also their capability of handling the unstructured grids needed to simulate very complex domains. This trend appears to have accelerated in the 1980s, with numerous sophisticated finite element shallow water codes emerging, such as FEUDX [134], which utilized the nonconservative form

of the primitive SWE, and FE2DY [168], among many others. Kinnmark and Gray (1984) developed a GWCE-based model using an implicit solution procedure [95]. Luettich and Westerink (1992) developed the GWCE-based solver ADCIRC [126]. Many of these codes were parallelized in the 1990s as problem sizes grew.

Very recently, DG methods have become popular, due in part to their compact stencil and the ease with which they handle complex, unstructured meshes. They have been shown, under certain conditions, to possess some advantages over the standard (continuous) Galerkin method in parallel computation as well [103]. Since the use of DG methods in shallow water models has been the subject of very intense investigation over the past decade, an entire section is devoted to these developments; see Section 1.2.3. The DG method has also been used in several two- and three-dimensional SWE codes, such as the ADCIRC-DG [101] hydrodynamic model, and UTBEST [1]; the former is the framework used to implement the coupled morphological model formulated in Chapter 2.

1.2.2 Sediment Transport Models

The history of research on the sediment transport problem is even longer than that for shallow water models. This is because there is evidence that this problem has been of interest to civilizations (in connection with channel construction) for more than 7200 years, dating to the Mesopotamian era [80]. An excursion through this many years of advances is far beyond the scope of this dissertation; in this section, an attempt will be made to review briefly only the "modern" developments in this vast, largely empirical field of research. The interested reader may refer to Graf (1971) for an excellent and

much more complete history [80].

Some context is needed. Exner (1925) suggested a one-dimensional model (neglecting diffusion) of sediment transport as the PDE

$$\frac{\partial \eta}{\partial t} + \frac{1}{1-m}\frac{\partial Q}{\partial x} = 0, \tag{1.2.4}$$

where η is the elevation of the bed above some datum, $m \in [0, 1)$ is the bed porosity, and Q is the sediment discharge rate, which he assumed directly proportional to the fluid velocity and in the direction of the flow [70]. Paola and Voller (2005) generalized equation (1.2.4) to account for conservation of total mass in a three-layer column consisting of seawater, sediment, and bedrock [142]. Their relation was complete, and included effects such as tectonic motion of the bedrock, bed compaction, and mass production/destruction through geochemical processes.

Equation (1.2.4) is simply a statement of conservation of sediment mass within the sediment column, which Exner used in part to explain dune and antidune formation [85]. However, a general-purpose, deterministic expression for Q is as yet unknown; it is the quest for an accurate expression for Q that has been the subject of extensive research and experimentation by engineers for around 150 years. The major developments are summarized below.

1.2.2.1 Bed Load Transport

Among the earliest approaches taken by many investigators involved finding direct expressions for the force exerted by the fluid on the bed [80, 194]. Du Buat (1786) introduced the shear-resistance concept, and proposed the first relationship between the force (and sediment discharge) and the channel depth and bed slope based on his experiments [64]. Stokes (1851) derived

a relation for the corresponding resistance force and drag coefficient C_D for spherical sediment particles by simplifying and solving directly the Navier–Stokes equations [80, 170, 194]. This work contains the earliest known use of the quantity now known as the Reynolds number; Stokes' solution for the drag coefficient was valid only for Reynolds numbers less than one.

Oseen considered the steady-state Navier–Stokes equations for a viscous fluid with the inertia terms and specialized BCs [140], and used the resulting BVP and solution to expand upon Stokes' expression for C_D [141]. Goldstein (1929) published a more complete version of this result [78, 79, 80]. Proudman and Pearson (1957) were able to combine the previous results using boundary layer theory, but had limited success extending them to somewhat higher Reynolds numbers [80, 148]. Thus, experimental data must still be used to estimate C_D in that circumstance.

A new model of bed load movement was introduced by du Boys (1879), who in his landmark paper hypothesized the sediment as moving in layers of a given thickness, with the top layer moving most rapidly [63]. He determined (p. 160) that

$$Q = \chi F(F - F_0), \tag{1.2.5}$$

where χ is what he termed a "characteristic coefficient" [63], F is the force exerted on the bed by the fluid, and F_0 is the entrainment force, i.e. the critical force necessary to initiate bed movement. Schoklitsch (1914) verified equation (1.2.5) experimentally, which popularized it, but objected to the layered model of transport since it did not agree with experimental data [161]. Nevertheless, equation (1.2.5) apparently formed the basis of bed load transport equations for many years [60, 139].

Numerous experiments were carried out in order to determine empirical formulæ for F_0 for various bed materials. However, Shields (1936) conjectured that it was extremely difficult to express F and F_0 analytically [194]. Instead, he opted for an excess bed shear stress approach, and published his now-famous diagram showing the (nondimensionalized) bed shear stress in terms of the particle Reynolds number [162]. Interestingly, Shields' "curve" was actually a narrow, shaded area, indicating some uncertainty in the value of τ_0, the critical shear stress; Rouse (1939) suggested a refined diagram, and proposed an easier method for calculating τ_0 empirically [159]. White (1940) discussed an analytical approach to finding τ_0 [85, 191, 194].

These developments prompted further investigation: beginning in the 1940s, and continuing into the present, a zoo of mostly excess bed shear stress-based empirical formulæ for Q have been proposed. Some of the more widely-used ones include that of Meyer-Peter and Müller (1948), Einstein (1950), Bagnold (1966), Ribberink (1998), and Camenen and Larson (2005); consult [11, 26, 67, 130, 154] for details. No attempt shall be made here to discuss the relative merits and deficiencies of each; an entire book could be written on this subject. Instead, the reader should refer to Sleath (1984) and Yang (1996) for a much more complete listing, analysis, and comparison with experimental and observational data [165, 194].

Alternatives to finding F_0 were also tried, such as finding critical shear velocity $u_0 = \sqrt{\tau_0/\rho}$, where ρ is the fluid density. Fortier and Scobey (1926) listed a table of maximum fluid speeds for which the bed will remain steady for many types of sediment material in canals [73]. Other velocity-based studies were performed by Hjulström (1935) and later by the American Society of Civil Engineers (ASCE); see [86] and [186], respectively, for details. Yang (1972)

adopted an analytical approach, utilizing some basic theories from fluid mechanics, and his results were confirmed experimentally during the 1980s [194]. Of course, this approach was not without its pitfalls, as it is well known that the fluid velocity at the channel bottom is difficult to measure directly, and averaged flow speeds are often used instead. The shear velocity can be estimated using any of several classical formulæ; see, for example, [55] or [129]. Also see Manning (1891) for a comparative study of the best-known expressions in use at that time.

However, it was understood by investigators at a relatively early stage that turbulence in the fluid flow plays an important role in determining the corresponding sediment transport rate [158, 162]. This point was emphasized further in [92]. Of course, this realization meant that no single, definite threshold value for τ_0 exists where the entire bed begins to move. Consequently, probabilistic models for transport were advanced. According to [194], it was Einstein (1950) who first broke with the trend of formulating Q in terms of critical criteria [67], and developed a probabilistic model based on his experimental data. Brown (1950) adopted Einstein's ideas in [22], and Gessler (1965) tabulated probabilities that sediment grains of a specific size would remain stationary when subjected to varying amounts of shear stress [77]. More recently, Kobayashi *et al.* (2010) developed a probabilistic model for bed load and suspended load transport due to currents and waves [98].

Presently, the trend in developing new bed load transport formulæ appears to remain with curve-fitting of experimental data, often by means of regression analysis; see, for example, [26, 157, 167]. Because of their agreement with experimental data for the flow conditions considered in this dissertation, the formulæ suggested in [26] and [167] are used in the model implementation

for all except the final test case described in Chapter 4.

1.2.2.2 Suspended Load Transport

The sediment transport rate Q includes not only the transport of bed load, but also of suspended load. This aspect of sediment transport is not as well understood as bed load transport [80]. Yet it cannot be overlooked, as this is known to be the main mode of transport in most rivers [194].

In any case, scientific analysis of the phenomenon has taken place for about 150 years, with Dupuit (1865) making one of the earliest attempts to model sediment in suspension [66]. He explained it as being caused by differences in velocities of the adjacent particles [80, 115]. In short, Dupuit's theory and basic assumptions appear to have been widely accepted until the 1930s, by which time it was realized that turbulence plays a significant role in the process [80]. Numerous attempts made during this time to definitively quantify the transport rate were largely unsuccessful; proposed formulæ showed poor agreement with experimental data.

A breakthrough in this area was achieved by Rouse (1937), who developed concentration diagrams for suspended sediment in a turbulent flow [80, 158]. His results rendered important aspects of earlier models of suspension (including that of Dupuit) obsolete, as suspended load transport is now thought to be governed mainly by the level of fluid turbulence [75]. His work also seems to have catalyzed research in this area, as a host of suspended load transport formulæ were proposed over the next several decades, such as those by Lane and Kalinske (1941), Einstein (1950), Brooks (1963), and Chang *et al.* (1965), among a host of others; see [21, 33, 67, 107] for details, and [80] and [165] for a more complete listing. Research in this area continues into the

present.

1.2.2.3 Transport due to Waves

Sediment transport due to waves comprises part of the sediment discharge rate Q. In the coastal zone, wave action is known to play an important, if not dominating (relative to the current), role in the transport process. For example, List *et al.* (2006) asserts that in many regions with seawater less than 60 m deep, a tenfold increase in Q may occur because of the effect of the waves, leading to isolated "hotspots" of erosion [121]. In essence, short waves are known to complicate the transport process by stirring the bed load, causing oscillatory transport rates that are not necessarily in phase with the wave [26]. Research in this area appears confined only to the past fifty years [26]. Even so, several oft-used empirical formulæ have been proposed. Among the more well-known ones are those of Madsen and Grant (1976), Bailard and Inman (1981), Dibajnia and Watanabe (1992), Soulsby (1997), Ribberink (1998), and Camenen and Larson (2005); consult [12, 59, 128, 154, 167] for details, and [26] for a concise listing of these. Others may be found by consulting Sleath (1984), who offers an excellent treatment of the subject [165].

The situation becomes further complicated when transport under the combined effects of waves plus steady and/or oscillatory (tidal) currents is considered. In many cases, the contributions of the waves and currents are not additive; see [26] or [165] for details. Also, many of the formulæ require several wave parameters, such as the wave speed, period, and significant wave height, to be known *a priori*; in practice, these would need to be calculated using analytical or numerical wave models, such as STWAVE [184] or SWAN [179], either separately (beforehand) or in parallel with the combined hydrodynamic-

sediment transport model.

1.2.2.4 Total Load Transport

Some brief remarks are in order regarding direct expression of the total discharge rate Q. A few investigators have attempted to quantify the total load discharge without separating it into total and suspended load components, and/or current and wave components. One such proposed relation is due to Engelund and Hansen (1967), and appears to be commonly used because of its relatively wide range of applicability and ease of implementation [194]. Additional ones may be found in [80] and [194], but their validity is often limited to grain sizes and flow profiles not under consideration in this dissertation.

1.2.2.5 Numerical Modeling

Until the rise of digital computing technology, almost all simulations of sediment transport (by waves and/or currents) were done either by direct field observations and measurements or by using flumes in laboratories. However, by the end of the 1970s, new numerical algorithms became available, and computers became powerful enough to make it feasible to predict numerically the transport rates in flowing channels, rivers, and coastal systems. As such, a few numerical models began to appear. Smith (1977) and Grant (1979) formulated one-dimensional models in [166] and [81], respectively, while Lepetit and Hauguel (1979) discuss a two-dimensional model in [116]. Numerous programs were developed beginning in the 1980s, such as SEDTRANS [135], RIVER [171], and CROSMOR [185], to name just a few. Finite difference-based solvers proved popular, though stochastic approaches were also tried [171, 185]. The work of Kriebel and Dean (1985) is of keen interest, since it is an early account

on numerically simulating beach erosion during hurricanes [100].

Owing to the fact that the two processes are inherently linked, interest in coupling numerical sediment transport models to hydrodynamic models has existed since at least the early 1980s, as evidenced in [99] and [116]. Initially applied to rivers, the models were quickly extended to estuarine and coastal environments [17, 71]. Recently, several coupled models have since been incorporated into larger, three-dimensional modeling frameworks such as FVCOM [36] and the Regional Ocean Modeling System (ROMS) [176]. The two-dimensional models generally fell into two types: the quasi-steady type, in which the hydrodynamic and transport processes are analyzed separately, and the fully-coupled type. A discussion and comparison of each in the context of finite volume methods (FVMs) may be found in [122].

Recently, several new two-dimensional DGFEM-based solvers incorporating bed morphology have appeared [101, 152, 153, 172], which form the basis of the present study. However, much work remains to be done in this area. As far as the author knows, there are currently no working solvers for the complete two-dimensional tightly-coupled SWE-Exner system which combine the extended LDG method to treat the nonconservative product (more on this in the next section) with wetting and drying and higher-order slope limiting algorithms.

1.2.3 Discontinuous Galerkin Methods

In this section, the literature review is concluded with a discussion on the development of DG methods, with an interest on the evolution of the extended methods used to treat nonconservative products. An attempt will be made to be brief here, but the interested reader may wish to consult Arnold

et al. (2002) for an excellent historical discourse on DG methods [5].

Compared with the development of shallow water and sediment transport models, discontinuous Galerkin methods are a modern idea, with their roots traceable to work by Lions (1968), who introduced them in a primitive form while solving second-order elliptic Dirichlet BVPs with very rough boundary data [120]. The idea was to enforce the BC weakly through a (sufficiently large) penalty. Aubin (1970) applied this method to finite difference approximations of nonlinear problems [6], while Babuška (1973) applied it within the finite element framework [7].

However, Babuška found that the convergence rates were suboptimal because the weak formulation was inconsistent; the exact solution did not satisfy the weak form of the regularized problem [5]. A workaround was found by Nitsche (1971), who proposed an alternative FEM-based penalty method with a consistent weak form, and showed that if the penalty is $\mathcal{O}(h^{-1})$ as $h \downarrow 0$, then the optimal $\mathcal{L}_2$- and $\mathcal{H}^1$-convergence rates are restored [138].

Around this time, it was observed that if Dirichlet BCs could be imposed weakly on the boundary instead of being incorporated into the finite element space, then it should be possible to enforce inter-element continuity in the same manner [5]. That is, terms that penalize the jump in the solution should be introduced on interior edges. Indeed, Babuška and Zlámal (1973) used this "interior penalty" (IP) method to weakly enforce $\mathcal{C}^1$-continuity on interior edges for fourth-order problems [8]. But their bilinear form was inconsistent: a consistent IP method was stated by Wheeler (1978), which was a generalization of Nitsche's method to second-order elliptic BVPs [190]. By the end of the 1970s, IP methods were well established.

Despite continuing advances made by investigators such as Douglas *et*

al. (1979) and Arnold (1982), who generalized Wheeler's technique to nonlinear hyperbolic and parabolic equations, respectively [4, 62], IP methods apparently fell out of favor beginning in the early 1980s. The decline in interest has been attributed to the method being no more efficient than the classical FEM, as well as to the difficulty in finding optimal values for the penalty parameter [5].

Meanwhile, an FEM very closely related to the IP method was proposed by Reed and Hill (1973), who were analyzing the neutron transport problem [149]. Lasaint and Raviart (1974) analyzed this method extensively, giving rise to the name "discontinuous Galerkin" (DG) method [108]. Further theoretical development followed during the next twenty years; convergence properties, in particular, appear to have been a subject of intense investigation, with an optimal rate of $h^{p+1/2}$ being established for general triangulations [91, 119, 146, 155]. Finally, it was realized that the similarity of the DG method to the IP method warranted an attempt at a unified analysis, which was undertaken by Arnold *et al.* (2002).

Development of RKDG methods appears to have been ongoing for thirty years. Chavent and Salzano (1982) applied the DG method in space to nonlinear hyperbolic equations, then applied the forward Euler method in time to the resulting ODE [35]. A natural generalization to explicit Runge–Kutta timestepping schemes was investigated by Cockburn and Shu (1989), beginning a comprehensive study. A series of five papers on these RKDG schemes resulted, which analyzed the stability and convergence of the method, discussed total variation diminishing (TVD) and total variation bounded (TVB) schemes, and explored (but did not introduce) the use of slope limiting [39, 40, 41, 42, 44]. Bassi and Rebay (1997) applied the RKDG method to compressible Navier–Stokes problems, adopting a mixed variant in which the solution gradi-

ents were not computed explicitly, but rather were approximated weakly [15]. The term "local discontinuous Galerkin" (LDG) method seems to have originated in [43]. Shortly thereafter, Cockburn and Dawson (1999) extended the LDG method to more general second-order problems [38], while Castillo *et al.* (2002) analyzed the *hp* version [29].

However, it was apparently realized by the end of the 1980s that hyperbolic conservation laws in nonconservative form posed unique challenges to DG methods; they could not be applied in a straightforward manner to systems unable to be written in divergence form. This proved especially problematic when the true solution became discontinuous—a phenomenon proved by Lax (1973) to occur in finite time for hyperbolic equations [109]—since then the solution (interpreted in the distributional sense) fails to exist, and Rankine–Hugoniot shock conditions cannot be formulated [153]. Thus, it became necessary to construct mathematically well-balanced schemes in order to properly handle the nonconservative product.

Several approaches were tried. Among the most widely accepted thus far is due to LeFloch (1989), who adopted a definition of the nonconservative product in terms of a bounded Borel measure [110]. This is a generalization of the Volpert (1967) product [48], and was originally applied to studies of deformation of elastoplastic materials and two-phase flows. His definition formed the cornerstone of the so-called DLM theory, introduced by Dal Maso *et al.* (1995) in [49]. Using this definition, LeFloch (1990), LeFloch and Liu (1993), and later Crasta and LeFloch (2002) were able to prove several important existence and uniqueness results [46, 111, 112]. Around the same time, Toumi (1992) developed a generalized Roe solver [177], which was applied to shock tube problems in [178]. An alternative approach was proposed by Saurel and

Abgrall (1999) in [160].

Lately, much of the work in this area has been devoted to finding well-balanced schemes in an FVM context; see, for example, [30, 143, 144]. Xing and Shu (2006) developed higher-order well-balanced WENO schemes for the RKDG framework in [192]. Very recently, Castro *et al.* (2010) designed well-balanced FDMs for nonconservative systems [31]. However, it is the recent work of Rhebergen *et al.* (2008) that will be of prime importance here, since they developed well-balanced schemes within the FEM context, and, along with Tassi *et al.* (2008), tested this scheme on a simplified version of the morphological system of interest here.

1.3 Summary of Contributions

In this dissertation, a tightly-coupled, robust, and efficient morphological model that utilizes the LDG finite element method has been presented, analyzed and implemented. It has been designed for use with two-dimensional structured and unstructured meshes within the Advanced Circulation (ADCIRC) modeling framework, and has been tested against exact and/or published solutions whenever possible. Specifically, the following have been achieved:

- The LDG method for the tightly-coupled morphological system, including all diffusion terms, has been formulated, and an *a priori* error estimate for a slightly simplified form of this system has been derived (see Chapter 3). The estimate does not contain an exponential bounding factor. The LDG formulation presented is $\mathcal{L}_2$-stable.

- The tightly-coupled morphological system, including the diffusion terms, with added stabilization terms designed to handle the nonconservative product arising in the momentum equations (see Section 2.4), has been implemented within the ADCIRC modeling framework (see Section 2.5).

- Code and model verification work has been done by testing the h- and p-convergence rates against the theoretical rates. This was achieved by comparing the DG model solution against an exact solution (see Section 4.1).

- The model's convergence behavior has been tested, at least qualitatively, on several simplified, idealistic two-dimensional coastal modeling applications. The model results are compared with those in the literature, where available (see Sections 4.2–4.4).

- A higher-order WENO-type slope limiting algorithm has been added to the implementation, which is designed to mitigate spurious oscillations in DG solutions of order two (see Section 2.5 for discussion). It is shown to work satisfactorily in Sections 4.2–4.4.

- The model is shown to capture several complex two-dimensional flow features near obstacles when the grid and solution undergo h- and p-refinement, respectively. The resulting flow properties are shown to coincide with those described in the literature (Sections 4.3 and 4.4).

- The relative computational costs of increasing p, the polynomial order of approximation, have been demonstrated when the model is run using a constant number of CPUs (see Section 4.6).

- The implementation is shown to possess the ability to handle dry regions whenever the use of a wetting and drying algorithm is enabled. This includes those regions that are initially protected by potentially over-topping barriers (see Section 4.5). The bed is shown to evolve qualitatively as expected in the vicinity of the barriers provided that p is of sufficient order.

1.4 Outline of Dissertation

The remainder of this dissertation is as follows. The interdependent system of governing equations for hydrodynamics and bed morphology are presented in detail in the next chapter. The LDG formulation and finite element discretization for this system of PDEs is given in Section 2.2. However, as mentioned above, the presence of dynamic bathymetry gives rise to a non-conservative product in the formulation. The analysis of such models is due primarily to Dal Maso *et al.* [49], and their theoretical results are summarized and discussed in Section 2.3. The resulting alternative semi-discrete formulation is the basis of the RKDG method as originally presented by Rhebergen *et al.* [152, 153], and is described in Section 2.4. Some details of the model implementation are described in Section 2.5.

In Chapter 3, an *a priori* error estimate for the conventional LDG method presented in Section 2.2 is derived. The error equation that arises from the semi-discrete formulation is shown in Section 3.1. A detailed and extensive analysis of this equation comprises the remainder of the chapter.

Several numerical studies are presented in Chapter 4. These studies highlight the convergence of the method in both h and p for problems with analytical solutions or those with previously published results. The focus is

on coastal engineering applications, in which flow and transport through a converging channel, around a bridge pile, within an inlet, and across a weir are investigated. In all applications except the last, the effects of h- and/or p-refinement within the RKDG formulation are studied. A brief runtime performance comparison is conducted in Section 4.6.

Finally, some concluding remarks about the work and results presented in Chapters 3 and 4 appear in Chapter 5. Also included (Section 5.2) is a series of possible future research directions and goals.

Chapter 2

Solution Methodology

This chapter begins with a presentation of the governing equations for hydrodynamics and sediment transport. A detailed derivation of the two-dimensional SWE, including a scaling analysis may be found in [101] and [187]. This is followed by a derivation of the weak formulation of the problem and its LDG finite element discretization. A discussion of the treatment of discontinuous true solutions follows, and an alternative semi-discrete formulation is derived, following [153]. Finally, an overview of the implementation is given, including a brief examination of the relevant boundary conditions (BCs), elements and element mappings, basis functions, time stepping algorithm, and post-processing operators.

The discussion concerning the problem description and finite element discretization may be found in the author's earlier work [131], as may much of the material appearing in the remainder of the chapter [132].

2.1 Model Problem Statement

The two-dimensional shallow water, or Saint-Venant, equations [1, 101, 187] coupled to the sediment transport, or Exner, equation [70] represent the system of incompletely parabolic partial differential equations under consideration in this dissertation. The SWE are the governing equations for hydrody-

namics, and are derived from the three-dimensional Navier–Stokes equations by applying Boussinesq's approximation [19], assuming a hydrostatic pressure distribution and uniform velocity profile in the vertical direction, using an eddy viscosity formulation, and integrating over depth [187]. Exner's equation governs the transport of sediment, and may be derived directly from so-called "first principles" by considering mass balance within the sediment column (lying directly beneath the seawater column) [101, 104].

Let $\Omega \subset \mathbb{R}^2$ be a bounded, polygonal spatial domain for all values of time $t \in (t_0, t_0 + T]$, given some fixed initial time $t_0 \in \mathbb{R}$ and some fixed $T > 0$, and let $\partial\Omega$ denote the boundary of Ω. On the set $\Omega \times (t_0, t_0 + T]$, the coupled system of conservation laws may be written concisely in Cartesian coordinates as

$$\partial_t(\mathbf{K}\mathbf{w}) + \nabla \cdot (\mathbf{F} - \mathsf{D} : \nabla\mathbf{w}) + \boldsymbol{G} : \nabla\mathbf{w} = \mathbf{s}, \tag{2.1.1}$$

where the quantity of interest is $\mathbf{w} = (H, \mathbf{q}^\top, b)^\top$. The first component of $\mathbf{w}$, which is $H = \zeta + b$, is the total depth of the seawater column, where ζ is the observed free surface elevation measured positively upward from a given vertical datum, and b is the bathymetric depth measured positively downward from the datum, as shown in Figure 2.1. The vector $\mathbf{q}$ is the discharge per unit width. Expressed in terms of velocity, $\mathbf{q} = (Hu, Hv)^\top$, where u and v represent the depth-averaged, Reynolds-averaged current velocity in the x- and y-direction, respectively.

In equation (2.1.1), the matrix $\mathbf{K} = \mathrm{diag}(1, 1, 1, -\kappa)$, where $\kappa \in (0, 1]$ is one minus the bed porosity. The value of κ is assumed to be spatially and temporally constant to facilitate the analysis in Chapter 3. The negative sign in front of κ accounts for b being measured positively downward, not upward.

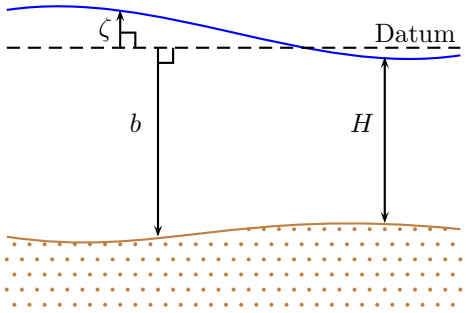

Figure 2.1: The seawater column in Cartesian coordinates

Continuing with equation (2.1.1), the quantity $\mathbf{F} \in \mathbb{R}^{4\times 2}$ denotes the inviscid flux. It may be written concisely as

$$\mathbf{F}(\mathbf{w}) = \left(\mathbf{q}, \frac{\mathbf{q}\otimes\mathbf{q}}{H} + \frac{gH^2}{2}\mathbf{I}, \tilde{\mathbf{q}}\right)^\top, \tag{2.1.2}$$

where g is the gravitational constant (taken as $9.80665\,\mathrm{m/s^2}$ in the implementation), $\mathbf{I} \in \mathbb{R}^{2\times 2}$ is the identity matrix, and $\tilde{\mathbf{q}}$ is the total sediment load discharge per unit width due to the combined effects of currents and waves. To simplify the analysis in Chapter 3, transport of bed load due to waves and transport of suspended load are neglected. This restriction on $\tilde{\mathbf{q}}$ remains in place in Chapter 4. For the moment, it is assumed that each component of $\mathbf{F}$ is sufficiently regular; it is shown in Chapter 3 that, under some mild assumptions, $\mathbf{F}$ is Lipschitz-continuous in all of its arguments.

The anisotropic diffusion coefficient is represented by the fourth-order tensor $\mathsf{D} \in \mathbb{R}^{4\times 2\times 4\times 2}$. For simplicity, it is assumed to be constant in space and time in Chapters 3 and 4. A difficulty arises here, however, because D is not invertible—a consequence of equation (2.1.1) being incompletely parabolic. To circumvent this limitation, D may be partitioned into sub-tensors that multiply the hydrodynamic and sedimentary components of $\nabla\mathbf{w}$. Let D_{ijkl} denote a

component of D for $i \in \{1,2,3,4\}$, $j \in \{1,2\}$, $k \in \{1,2,3,4\}$, and $l \in \{1,2\}$. Define the sub-tensors

$$\mathsf{H} = \mathsf{D}|_{i,k\in\{2,3\}} = \begin{pmatrix} \begin{pmatrix} \nu_x & 0 \\ 0 & 0 \end{pmatrix} & \begin{pmatrix} 0 & \nu_y \\ 0 & 0 \end{pmatrix} \\ \begin{pmatrix} 0 & 0 \\ \nu_x & 0 \end{pmatrix} & \begin{pmatrix} 0 & 0 \\ 0 & \nu_y \end{pmatrix} \end{pmatrix},$$
$$\mathbf{S} = \mathsf{D}|_{i=k=4} = \operatorname{diag}(\tilde{\nu}_x, \tilde{\nu}_y),$$

where ν_x, ν_y, $\tilde{\nu}_x$, and $\tilde{\nu}_y$ are all strictly positive, and represent hydrodynamic and sedimentary eddy viscosity in the x- and y-direction, respectively. The remaining components of D are zero. Under these restrictions, both H and $\mathbf{S}$ are easily inverted; each nonzero scalar component may simply be inverted in place. Note that in the case of isotropic seawater flow, $\mathsf{H} = \nu\mathsf{I}$, where $\mathsf{I} \in \mathbb{R}^{2\times2\times2\times2}$ is the fourth-order identity tensor; for isotropic transport, $\mathbf{S} = \tilde{\nu}\mathbf{I}$. This is the scenario handled in the implementation.

The remaining term appearing on the left-hand side of equation (2.1.1) is the nonconservative product, where $\boldsymbol{G} \in \mathbb{R}^{4\times2\times4}$ is a third-order tensor which cannot be expressed as the Jacobian of some matrix [49, 152, 153]. This term may be rewritten, since $\boldsymbol{G}$ has only two nonzero components: $G_{214} = G_{324} = -gH$. Therefore $\boldsymbol{G} : \nabla\mathbf{w} = (0, -gH\nabla b^\top, 0)^\top$.

Finally, the vector $\mathbf{s}$ denotes the source terms, which are nonzero only in the momentum equations. That is,

$$\mathbf{s}(\mathbf{w}) = \left(0, \left(-\tau_{\mathrm{bf}}\mathbf{q} - \varrho^{-1}(H\nabla p_{\mathrm{atm}} - \boldsymbol{\tau}_{\mathrm{wind}} - \boldsymbol{\tau}_{\mathrm{rad}})\right)^\top, 0\right)^\top, \tag{2.1.3}$$

where the nonnegative quantity τ_{bf} represents a constant bottom friction coefficient; ϱ, the seawater reference density[1]; p_{atm}, the atmospheric pressure at the

[1]Taken as $1024.763\,\mathrm{kg/m^3}$ in the implementation, which corresponds approximately to seawater at $20\,^\circ\mathrm{C}$ with salinity $35\,\mathrm{psu}$ in the IES-80 equation of state [180].

sea surface; $\boldsymbol{\tau}_{\text{wind}}$, the wind stress at the sea surface, and $\boldsymbol{\tau}_{\text{rad}}$, the radiation stress at the sea surface caused by short wind-driven waves.

It has not escaped the author's notice that the Coriolis and tidal potential terms have been omitted from equation (2.1.3). These forcing terms, while important when simulating geophysical phenomena over a portion of the surface of the Earth, do not significantly affect the error analysis performed in Chapter 3, nor do they affect the overall stability of the LDG method. If investigators should insist on including these terms when Cartesian coordinates are used, several approaches may be used. One, which is valid for small portions of the Earth's surface, is to apply the so-called "β-plane" approximation; see [187] for details. Another approach is to convert longitude-latitude pairs (λ, φ) to linear distances (x, y) using the carte parallelogrammatique projection (CPP):

$$\begin{aligned} x &= R(\lambda - \lambda_0)\cos\varphi_0, \\ y &= R(\phi - \phi_0), \end{aligned}$$

where R is the mean radius of the Earth (m) and (λ_0, φ_0) is the center of the projection. Care, however, must be taken to properly account for this transformation in all derivatives appearing in equation (2.1.1); a so-called "spherical correction factor" is required [51]. The CPP approach is taken in the implementation when spherical coordinates are used. However, the Coriolis and tide-generating potential terms are zero in the test cases presented in Chapter 4, since Cartesian coordinates are used.

The first step in formulating this problem by the LDG method is to rewrite equation (2.1.1) as a first-order system in mixed form by introducing an auxiliary variable $\mathbf{Z} \in \mathbb{R}^{4\times 2}$ with components Z_{ij}. Then the initial-boundary

value problem is

$$\begin{cases} \partial_t(\mathbf{K}\mathbf{w}) = -\nabla\cdot(\mathbf{F}+\mathbf{Z}) + \mathbf{g} + \mathbf{s}, & \text{on } \Omega\times(t_0, t_0+T], \\ \mathbf{Z} = -\mathsf{D}:\nabla\mathbf{w}, & \text{on } \Omega\times(t_0, t_0+T], \\ \mathbf{w} = \mathbf{w}_0, & \text{on } \Omega\times\{t=t_0\}, \\ \mathbf{w} = \mathbf{w}_D, & \text{on } \partial\Omega\times[t_0, t_0+T], \end{cases} \tag{2.1.4}$$

where $\mathbf{g}(\mathbf{Z}) = -gH(0, \tilde{\nu}_x^{-1}Z_{41}, \tilde{\nu}_y^{-1}Z_{42}, 0)^\top$, $\mathbf{w}_0$ is the initial data, and $\mathbf{w}_D$ is the Dirichlet data, which was chosen for convenience and simplicity; the implementation requires more complicated boundary conditions, which are discussed in Section 2.5.1. It is also assumed that a unique solution to (2.1.4) exists, although mathematical results in this realm are largely unavailable at present [69].

2.2 Finite Element Discretization

2.2.1 Weak Formulation

Let Ω be approximated by a family of regular finite element partitions $\{\Omega_h\}_{h>0}$ such that

$$\overline{\Omega} = \{\cup_E \Omega_E\} \cup \big\{\{\cup_I \Gamma_I\} \cup \{\cup_B \Gamma_B\}\big\} \cup \big\{\cup_N \{\mathbf{x}_N\}\big\},$$

where $\overline{\Omega}$ denotes the closure of Ω; Ω_E, an element; Γ_I, an interior edge; Γ_B, a boundary edge, and $\{\mathbf{x}_N\}$, a node. Recall that since Ω is polygonal, $\Omega_h = \Omega$; domain approximation errors were not considered in this dissertation. The elements are convex, nonoverlapping subdomains with Lipschitz boundaries which do not cross $\partial\Omega$, with the element size parametrized by $h_E = \operatorname{diam}(\Omega_E)$, so that $h = \max_E h_E$. Additionally, each physical element is affinely equivalent to one of several master elements [20]; see Section 2.5 for a brief description.

Each Ω_h may be nonconforming; element boundaries do not have to align.[2] However, it is assumed that the number of elements sharing an edge is bounded independently of h. Lastly, each Ω_h is assumed to be locally quasi-uniform [20].

Define the function spaces

$$\begin{aligned}
\mathcal{X}_h &= \left\{ f \in \mathcal{L}_2(\Omega_h) \cap BV(\Omega_h) : f|_{\Omega_E} \in \mathcal{H}^1(\Omega_E) \text{ for all } \Omega_E \subseteq \Omega_h \right\}, \\
\mathcal{W}_h &= [\mathcal{L}_\infty(t_0, t_0 + T; \mathcal{X}_h)]^4, \\
\mathcal{Z}_h &= [\mathcal{L}_\infty(t_0, t_0 + T; \mathcal{X}_h)]^{4\times 2},
\end{aligned}$$

where $BV(\Omega_h) \subset \mathcal{L}_1(\Omega_h)$ denotes the space of functions of bounded variation on Ω_h; these functions have well-defined traces on element boundaries. For any function $\mathbf{f} \in \mathcal{W}_h$, its "interior" and "exterior" traces are denoted for any fixed time t as

$$\begin{aligned}
\mathbf{f}^{(\text{in})}(t, \mathbf{x}) &= \lim_{\varepsilon \uparrow 0} \mathbf{f}(t, \mathbf{x} + \varepsilon \mathbf{n}), \\
\mathbf{f}^{(\text{ex})}(t, \mathbf{x}) &= \lim_{\varepsilon \downarrow 0} \mathbf{f}(t, \mathbf{x} + \varepsilon \mathbf{n}),
\end{aligned}$$

where $\mathbf{x} \in \left\{ \{\cup_I \Gamma_I\} \cup \{\cup_B \Gamma_B\} \right\}$ and $\mathbf{n}$ is the unit normal vector that points toward the element with the lower index, with $\mathbb{R}^2 \backslash \overline{\Omega}$ corresponding to $E = 0$. By this convention, $\mathbf{f}^{(\text{in})}(t, \cdot)$ is the interior trace with respect to the element with the *higher* index sharing the edge. Observe that since $\mathbf{f}(t, \cdot)|_{\Omega_E} \in [\mathcal{H}^1(\Omega_E)]^4$, both $\mathbf{f}^{(\text{in})}(t, \cdot)$ and $\mathbf{f}^{(\text{ex})}(t, \cdot)$ reside in $[\mathcal{H}^{1/2}(\partial\Omega_E)]^4$ because they merely represent the action of the trace operator upon $\mathbf{f}$ at some fixed time. The "average" and "jump" operators may then be defined for any fixed time t as

$$\{\{\mathbf{f}\}\} = \frac{1}{2}\left(\mathbf{f}^{(\text{in})} + \mathbf{f}^{(\text{ex})}\right), \tag{2.2.1}$$

$$[\![\mathbf{f}]\!] = \mathbf{f}^{(\text{in})} - \mathbf{f}^{(\text{ex})}, \tag{2.2.2}$$

[2] Valid for the analysis in Chapter 3 only. In the implementation, and in all test cases presented herein, all elements were conforming.

where the dependencies of the functions on t and $\mathbf{x}$ have been suppressed. Similar definitions for the interior and exterior trace, average, and jump hold for functions residing in $\mathcal{Z}_h$. It should be noted that these definitions were chosen for convenience and simplicity; they differ slightly from those commonly used in the literature [152, 153, 172], in that the jump of a vector-valued (matrix-valued) function is a vector (matrix), not a scalar, since the normal is not included in equation (2.2.2).

Throughout this dissertation, the $\mathcal{L}_2(\Omega_E)$-inner product notation $(\cdot,\cdot)_E$ is used on elements and the $\mathcal{L}_2(\partial\Omega_E)$-inner product notation $\langle\cdot,\cdot\rangle$ on edges, with either an I or a B appended as necessary to distinguish inner products over interior and boundary edges. The arguments may be scalar-, vector-, or matrix-valued functions, with the understanding that if each $f_i(t,\cdot) \in \mathcal{L}_2(\Omega_E)$ and each $g_i(t,\cdot) \in \mathcal{L}_2(\Omega_E)$, then

$$(\mathbf{f},\mathbf{g})_E = \sum_{i=1}^{4} (f_i, g_i)_E \,,$$

and that if each $F_{ij}(t,\cdot) \in \mathcal{L}_2(\Omega_E)$ and each $G_{ij}(t,\cdot) \in \mathcal{L}_2(\Omega_E)$, then

$$(\mathbf{F},\mathbf{G})_E = \sum_{i=1}^{4}\sum_{j=1}^{2} (F_{ij}, G_{ij})_E \,.$$

Similar definitions apply for inner products on the edges.

In addition, the notation $\|\cdot\|_{r,E}$ is used to denote the $\mathcal{H}^r(\Omega_E)$-norm for integral values of $0 \le r < \infty$; $\|\cdot\|_{r,I}$, the $\mathcal{H}^r(\Gamma_I)$-norm; $\|\cdot\|_{r,B}$, the $\mathcal{H}^r(\Gamma_B)$-norm, and $\|\cdot\|_{r,h}$, the $\mathcal{H}^r(\Omega_h)$-norm. As before, the arguments may be scalar-, vector-, or matrix-valued, and hold for any fixed time t. The $\mathcal{L}_2(\Omega_h)$- and $\mathcal{L}_2(\Omega_E)$-norms are related by

$$\|f\|_{0,h}^2 = \sum_E \|f\|_{0,E}^2 \,,$$

provided that $f(t,\cdot) \in \mathcal{L}_2(\Omega_E)$ for all $\Omega_E \subseteq \Omega_h$.

With these definitions and conventions, the initial-boundary value problem (2.1.4) may be rewritten and stated in the following weak form:

Find $\mathbf{w}$ *and* $\mathbf{Z}$ *such that*

$$\begin{cases} \displaystyle\sum_E \big(\partial_t(\mathbf{K}\mathbf{w}), \mathbf{v}\big)_E = -\sum_I \big\langle (\mathbf{F}+\mathbf{Z})\mathbf{n}, [\![\mathbf{v}]\!] \big\rangle_I - \sum_B \big\langle (\mathbf{F}+\mathbf{Z})\mathbf{n}, \mathbf{v}^{(\mathrm{in})} \big\rangle_B \\ \qquad\qquad + \displaystyle\sum_E \big\{ (\mathbf{F}+\mathbf{Z}, \nabla\mathbf{v})_E + (\mathbf{g}+\mathbf{s}, \mathbf{v})_E \big\}, \\ \displaystyle\sum_E (\mathbf{Z}, \mathbf{V})_E = -\sum_I \big\langle \mathbf{w}, (\mathsf{D} : [\![\mathbf{V}]\!])\mathbf{n} \big\rangle_I - \sum_B \big\langle \mathbf{w}_D, \big(\mathsf{D} : \mathbf{V}^{(\mathrm{in})}\big)\mathbf{n} \big\rangle_B \\ \qquad\qquad + \displaystyle\sum_E \big(\mathbf{w}, \nabla\cdot(\mathsf{D} : \mathbf{V})\big)_E, \\ \displaystyle\sum_E \big(\mathbf{w}(t_0,\cdot), \mathbf{v}\big)_E = \sum_E (\mathbf{w}_0, \mathbf{v})_E \,, \end{cases} \tag{2.2.3}$$

for all $\mathbf{v} \in \mathcal{W}_h$ *and all* $\mathbf{V} \in \mathcal{Z}_h$.

2.2.2 Semi-discrete Formulation

Now define the function spaces

$$\begin{aligned} \mathcal{X}_{hp} &= \{ f \in \mathcal{X}_h : f|_{\Omega_E} \in \mathcal{P}^p(\Omega_E) \text{ for all } \Omega_E \subseteq \Omega_h \}, \\ \mathcal{W}_{hp} &= [\mathcal{L}_\infty(t_0, t_0+T; \mathcal{X}_{hp})]^4, \\ \mathcal{Z}_{hp} &= [\mathcal{L}_\infty(t_0, t_0+T; \mathcal{X}_{hp})]^{4\times 2}, \end{aligned}$$

where $\mathcal{P}^p(\Omega_E)$ denotes the space of complete polynomials of degree $p \geq 0$ defined on Ω_E. It is assumed for simplicity that p remains the same from element to element; consideration of adaptivity in p is beyond the scope of this dissertation. Note that $\mathcal{X}_{hp}$ represents a finite-dimensional subspace of $\mathcal{X}_h$.

It is desired to approximate the solution $\mathbf{w}$ and $\mathbf{Z}$ to (2.2.3) by a finite

element solution $\mathbf{w}_{hp} \in \mathcal{W}_{hp}$ and $\mathbf{Z}_{hp} \in \mathcal{Z}_{hp}$. However, $\mathbf{w}_{hp}$ and $\mathbf{Z}_{hp}$, and hence $\mathbf{F}_{hp} = \mathbf{F}(\mathbf{w}_{hp})$, are not single-valued on $\cup_I \Gamma_I$. Therefore, it is necessary to replace these terms with carefully chosen numerical fluxes; it is imperative that these numerical fluxes preserve the stability and consistency of the method. In addition, nonlinear fluxes must also preserve entropy conditions.

Let $\Pi\mathbf{F}_{hp}(t,\cdot) \in \mathcal{Z}_{hp}$ be the $\mathcal{L}_2(\Omega_E)$-projection of $\mathbf{F}_{hp}(t,\cdot)$ into the space $\mathcal{Z}_{hp}$ for any fixed time t:

$$\left(\mathbf{F}_{hp} - \Pi\mathbf{F}_{hp}, \mathbf{V}\right)_E = 0 \qquad \text{for all } \mathbf{V} \in \mathcal{Z}_{hp}.$$

That is, $\Pi\mathbf{F}_{hp}$ is the best approximation of $\mathbf{F}_{hp}$ in $\mathcal{Z}_{hp}$. The nonlinear flux on all interior and boundary edges is then approximated by

$$(\Pi\mathbf{F}_{hp})\mathbf{n} \approx \{\!\{\Pi\mathbf{F}_{hp}\}\!\}\mathbf{n} + \boldsymbol{\sigma}[\![\mathbf{w}_{hp}]\!], \tag{2.2.4}$$

where $\boldsymbol{\sigma} \in \mathbb{R}^{4\times 4}$ acts as a stabilization term, in the form of numerical diffusion. Notice that the approximation to $\Pi\mathbf{F}_{hp}$ defined by equation (2.2.4) is similar in form to many commonly used numerical fluxes, such as the Roe [156] or local Lax-Friedrichs flux. The stabilization term is defined as

$$\begin{aligned}\boldsymbol{\sigma} &= \operatorname{diag}(\sigma_{11}, \sigma_{22}, \sigma_{33}, \sigma_{44}) \\ &= \operatorname{diag}\left(\frac{\alpha}{2}, \max\left\{\frac{\alpha}{2}, \mu\right\}, \max\left\{\frac{\alpha}{2}, \mu\right\}, \max\left\{\frac{\alpha}{2}, \tilde{\mu}\right\}\right).\end{aligned} \tag{2.2.5}$$

In equation (2.2.5), $\alpha = \max\{\alpha^{(\text{in})}, \alpha^{(\text{ex})}\}$ is assumed to be bounded from above independently of h, where $\alpha^{(\text{in})}$ and $\alpha^{(\text{ex})}$ are the maximum eigenvalues in absolute value of $\nabla\mathbf{F}_{hp}^{(\text{in})} \cdot \mathbf{n}$ and $\nabla\mathbf{F}_{hp}^{(\text{ex})} \cdot \mathbf{n}$, respectively, and are dependent on the expression for $\tilde{\mathbf{q}}$. The parameters μ and $\tilde{\mu}$ are penalties, and both are of the order h^{-1} as $h \downarrow 0$. This property, together with the boundedness

assumption about α above, ensures that σ_{22}, σ_{33}, and σ_{44} (but not σ_{11}!) are all of the order h^{-1} as $h \downarrow 0$.

The linear boundary fluxes pose less of a problem; it is unnecessary to either project onto the finite element space or introduce penalty terms. They are defined as the averages of the interior and exterior traces of the functions:

$$\mathbf{w}_{hp}(t,\mathbf{x}) \approx \{\{\mathbf{w}_{hp}(t,\mathbf{x})\}\},$$
$$\mathbf{Z}_{hp}(t,\mathbf{x}) \approx \{\{\mathbf{Z}_{hp}(t,\mathbf{x})\}\},$$

for all $\mathbf{x} \in \big\{\{\cup_I \Gamma_I\} \cup \{\cup_B \Gamma_B\}\big\}$ and each fixed time t.

In addition, since $\mathbf{g}_{hp} = \mathbf{g}(\mathbf{Z}_{hp})$, $\mathbf{s}_{hp} = \mathbf{s}(\mathbf{w}_{hp})$, and $\mathbf{w}_0$ do not generally reside in $\mathcal{W}_{hp}$, let $\Pi\mathbf{g}_{hp}(t,\cdot)$, $\Pi\mathbf{s}_{hp}(t,\cdot)$, and $\Pi\mathbf{w}_0$ be the $\mathcal{L}_2(\Omega_E)$-projections of $\mathbf{g}_{hp}(t,\cdot)$, $\mathbf{s}_{hp}(t,\cdot)$, and $\mathbf{w}_0$ into $\mathcal{W}_{hp}$, respectively, for any fixed time t. Then the semi-discrete statement of (2.1.4) is:

Find $\mathbf{w}_{hp} \in \mathcal{W}_{hp}$ *and* $\mathbf{Z}_{hp} \in \mathcal{Z}_{hp}$ *such that*

$$\begin{cases} \displaystyle\sum_E \big(\partial_t(\mathbf{K}\mathbf{w}_{hp}), \mathbf{v}\big)_E = -\sum_I \big\langle \{\{\Pi\mathbf{F}_{hp}\}\}\mathbf{n} + \boldsymbol{\sigma}[\![\mathbf{w}_{hp}]\!] + \{\{\mathbf{Z}_{hp}\}\}\mathbf{n}, [\![\mathbf{v}]\!]\big\rangle_I \\ \qquad\qquad\qquad\qquad - \displaystyle\sum_B \big\langle \Pi\mathbf{F}^{(\mathrm{in})}_{hp}\mathbf{n} + \boldsymbol{\sigma}\big(\mathbf{w}^{(\mathrm{in})}_{hp} - \mathbf{w}_D\big) + \mathbf{Z}^{(\mathrm{in})}_{hp}\mathbf{n}, \mathbf{v}^{(\mathrm{in})}\big\rangle_B \\ \qquad\qquad\qquad\qquad + \displaystyle\sum_E \Big\{ (\Pi\mathbf{F}_{hp} + \mathbf{Z}_{hp}, \nabla\mathbf{v})_E + \big(\Pi(\mathbf{g}_{hp} + \mathbf{s}_{hp}), \mathbf{v}\big)_E \Big\}, \\ \displaystyle\sum_E (\mathbf{Z}_{hp}, \mathbf{V})_E = -\sum_I \big\langle \{\{\mathbf{w}_{hp}\}\}, (\mathsf{D} : [\![\mathbf{V}]\!])\mathbf{n}\big\rangle_I \\ \qquad\qquad\qquad\qquad - \displaystyle\sum_B \big\langle \mathbf{w}_D, \big(\mathsf{D} : \mathbf{V}^{(\mathrm{in})}\big)\mathbf{n}\big\rangle_B \\ \qquad\qquad\qquad\qquad + \displaystyle\sum_E \big(\mathbf{w}_{hp}, \nabla\cdot(\mathsf{D} : \mathbf{V})\big)_E, \\ \displaystyle\sum_E \big(\mathbf{w}_{hp}(t_0,\cdot), \mathbf{v}\big)_E = \sum_E (\Pi\mathbf{w}_0, \mathbf{v})_E\,, \end{cases} \tag{2.2.6}$$

for all $\mathbf{v} \in \mathcal{W}_{hp}$ *and all* $\mathbf{V} \in \mathcal{Z}_{hp}$.

2.3 Treatment of Discontinuous Solutions

Consider the situation when the diffusion tensor D is identically zero in equation (2.1.1):

$$\partial_t(\mathbf{K}\mathbf{w}) + \nabla \cdot \mathbf{F} + \boldsymbol{G} : \nabla \mathbf{w} = \mathbf{s}. \tag{2.3.1}$$

The semi-discrete formulation that would result by following the procedure in the previous section is:

Find $\mathbf{w}_{hp} \in \mathcal{W}_{hp}$ *such that*

$$\begin{cases} \displaystyle\sum_E \big(\partial_t(\mathbf{K}\mathbf{w}_{hp}), \mathbf{v}\big)_E = -\sum_I \big\langle \{\!\{\Pi\mathbf{F}_{hp}\}\!\}\mathbf{n} + \boldsymbol{\sigma}[\![\mathbf{w}_{hp}]\!], [\![\mathbf{v}]\!] \big\rangle_I \\ \qquad\qquad\qquad\qquad - \displaystyle\sum_B \big\langle \Pi\mathbf{F}^{(\mathrm{in})}_{hp}\mathbf{n} + \boldsymbol{\sigma}\big(\mathbf{w}^{(\mathrm{in})}_{hp} - \mathbf{w}_D\big), \mathbf{v}^{(\mathrm{in})} \big\rangle_B \\ \qquad\qquad\qquad\qquad + \displaystyle\sum_E \Big\{ \big(\Pi\mathbf{F}_{hp}, \nabla\mathbf{v}\big)_E + \big(\Pi(\mathbf{g}_{hp} + \mathbf{s}_{hp}), \mathbf{v}\big)_E \Big\}, \\ \displaystyle\sum_E \big(\mathbf{w}_{hp}(t_0, \cdot), \mathbf{v}\big)_E = \sum_E \big(\Pi\mathbf{w}_0, \mathbf{v}\big)_E, \end{cases} \tag{2.3.2}$$

for all $\mathbf{v} \in \mathcal{W}_{hp}$,

where $\mathbf{g}_{hp} = (0, gH_{hp}\nabla b^{\top}_{hp}, 0)^{\top}$.

The problem given by (2.3.2) is ill posed whenever the true solution becomes discontinuous. This phenomenon is generally expected to occur here, since equation (2.3.1) is a nonlinear hyperbolic PDE in nonconservative form; shocks are known to develop over time [109]. Thus, weak solutions to (2.3.1) will not exist because the distributional derivatives are not defined at the discontinuities, and consequently no Rankine–Hugoniot shock conditions may be defined [152, 153].

The underlying issue in the ill-posedness of (2.3.2) is the presence of the nonconservative product $\boldsymbol{G} : \nabla\mathbf{w}$, with nonzero components appearing

in the momentum equations, which are represented by the second and third components of equation (2.3.1). Since $\boldsymbol{G}$ cannot be expressed as the Jacobian of some tensor $\mathbf{Q} \in \mathbb{R}^{4\times 2}$, equation (2.3.1) cannot be written in so-called divergence form:

$$\partial_t(\mathbf{Kw}) + \nabla \cdot \mathbf{Q} = \mathbf{s}. \tag{2.3.3}$$

As a result, traditional DG methods cannot be applied to this system in a straightforward manner.

There are three options available to treat this shortcoming. The first is to use the fully nonconservative form of (2.3.1). Indeed, by considering the fully nonconservative form of the coupled system in one space dimension, adjusted characteristic speeds may be extracted and incorporated into the definition of the numerical flux, and the system may then be expressed in divergence form. However, in two space dimensions, this approach fails. Moreover, this option is unattractive from a numerical point of view, since the numerical method may then possibly converge to nonphysical (*i.e.*, non-entropy-preserving) solutions [101].

The second approach involves uncoupling the sediment transport equation, represented by the fourth component of (2.3.1), from the SWE, represented by the first three components of (2.3.1), at least to some extent. Based on physical arguments involving typical time scales for sediment and seawater transport rates, this approach was previously taken in the model implementation [101]. The principal drawback to this approach is its lack of accuracy during instances when the time scales for transport of sediment and seawater become similar, such as during the extreme events ultimately desired to simulate. Some additional commentary regarding quasi-steady and fully coupled formulations may be found in [123].

The remaining option is to employ a special treatment for the nonconservative product. This was done in previous work for one-dimensional problems in [47] and for two phase flow problems in [16]. An alternative treatment was proposed by Dal Maso *et al.* [49] and applied by Rhebergen *et al.* to one- and two-dimensional problems using the DG method with piecewise linear finite element basis functions in [153]. It is this treatment that will be discussed throughout the remainder of this section and used in the implementation.

The ideas proposed in [49] for overcoming the absence of a weak solution are twofold:

1. Introduce a smooth path function which connects the interior and exterior states across a discontinuity, and

2. Define the nonconservative product in terms of a bounded Borel measure.

Once done, and a new numerical flux defined, a notion of "weak solution" may be given to equation (2.3.1), and an alternative semi-discrete formulation may be derived.

The first idea proposed by Dal Maso *et al.* is to regularize the true solution $\mathbf{w}$ near discontinuities by connecting the interior and exterior traces $\mathbf{w}^{(\text{in})}$ and $\mathbf{w}^{(\text{ex})}$ (assuming these are well defined) with a smooth path function $\boldsymbol{\chi} : [0,1] \to \mathbb{R}^4$ parametrized by $\tau \in [0,1]$. This path $\boldsymbol{\chi}$ must satisfy the following properties:

1. [End conditions.] By definition, $\boldsymbol{\chi}(0) = \mathbf{w}^{(\text{in})}$ and $\boldsymbol{\chi}(1) = \mathbf{w}^{(\text{ex})}$,

2. [Consistency.] If $[\![\mathbf{w}]\!] = 0$, then $\boldsymbol{\chi}(\tau) = \mathbf{w}^{(\text{in})}$,

3. [Lipschitz-continuity.] For each component χ_i of $\boldsymbol{\chi}$, there exists a constant $M > 0$ such that

$$|\partial_\tau \chi_i(\tau)| \leq M |[\![w_i]\!]|$$

for a.e. $\tau \in [0, 1]$, and

4. [Symmetry.] In two or more space dimensions, the path must be symmetric with respect to an interchange of the traces.

Condition 4 need not be satisfied for one-dimensional problems [49, 153].

Define the third-order tensor $\boldsymbol{T} \in \mathbb{R}^{4\times 2\times 4}$ by the relation

$$\boldsymbol{T} = \partial_{\mathbf{w}} \mathbf{F} + \boldsymbol{G}, \tag{2.3.4}$$

where $\partial_{\mathbf{w}} \mathbf{F}$ denotes the Jacobian of $\mathbf{F}$ with respect to $\mathbf{w}$. Then equation (2.3.1) may be rewritten as

$$\partial_t (\mathbf{K}\mathbf{w}) + \boldsymbol{T} : \nabla \mathbf{w} = \mathbf{s}. \tag{2.3.5}$$

With the coupled system expressed by (2.3.5), the following theorem, due to Dal Maso *et al.* [49], on the integration of nonconservative products, which are treated as a bounded Borel measure, may be stated:

Theorem 2.3.1 (Dal Maso *et al.*, 1995)**.** *Assume that*

1. *The function* $\mathbf{w}$ *is bounded on its domain* Ω*,*

2. *The function* $\mathbf{w}$ *is of bounded variation on* Ω*,*

3. *Each entry of* $\mathbf{T}$ *is a locally bounded, measurable function that maps Borel sets to Borel sets, and*

4. *The domain* $\Omega = \Omega^C \cup \Omega^J \cup \Omega^I$ *with each subset disjoint, where* Ω^C *is the set where* $\mathbf{w}$ *is almost everywhere continuous,* Ω^J *is the set of jumps in* $\mathbf{w}$*, and* Ω^I *is the set of "irregular" (nodal) points.*

Then there exists a unique, bounded vector of Borel measures $\boldsymbol{\mu} : \Omega \to \mathbb{R}^4$ *such that for a given Borel subset* $A \subset \Omega$*,*

1. *If* $A \subset \Omega^C$*, then*
$$\boldsymbol{\mu}(A) = \int_A \mathbf{T} : \nabla \mathbf{w} \, dA,$$
2. *If* $A \subset \Omega^J$*, then*
$$\boldsymbol{\mu}(A) = \int_A \left(\int_0^1 \mathbf{T}(\boldsymbol{\chi}) \partial_\tau \boldsymbol{\chi} \, d\tau \right) \mathbf{n} \, dA,$$
where $\mathbf{n}$ *is directed toward the region where* $\tau = 1$*, and*
3. *If* $A \subset \Omega^I$*, then*
$$\boldsymbol{\mu}(A) = \mathbf{0}.$$

Proof. Consult [49]. □

Remark 2.3.2. Assumption 2 is crucial since it guarantees that $\mathbf{w}^{(\text{in})}$ and $\mathbf{w}^{(\text{ex})}$ are well defined, and also ensures that $\mathbf{w}$ admits only jump-type discontinuities on Ω. For this reason, the space $BV(\Omega_h)$ was incorporated into the definition of the function spaces $\mathcal{W}_{hp}$ and $\mathcal{Z}_{hp}$ in Section 2.2.1.

Remark 2.3.3. In practice, and throughout the remainder of this dissertation,
$$\begin{aligned} \Omega^C &= \cup_E \Omega_E, \\ \Omega^J &= \{\cup_I \Gamma_I\} \cup \{\cup_B \Gamma_B\}, \\ \Omega^I &= \cup_N \{\mathbf{x}_N\}. \end{aligned}$$

2.4 Alternative semi-discrete formulation

Having introduced smooth paths which connect discontinuities in the true solution of equation (2.3.5), and defined the nonconservative product, it is now possible to seek a weak solution to (2.3.5) by way of an alternative semi-discrete formulation. This is derived following the approach discussed in [153] and [172].

Multiplying equation (2.3.5) by a test function $\mathbf{v} \in \mathcal{W}_h$, integrating over Ω_h, and rearranging gives

$$\sum_E \big(\partial_t(\mathbf{Kw}), \mathbf{v}\big)_E = -\int_{\Omega_h} \mathbf{v} \cdot \, d\boldsymbol{\mu} + \sum_E (\mathbf{s}, \mathbf{v})_E \,. \tag{2.4.1}$$

By Theorem 2.3.1,

$$d\boldsymbol{\mu} = \begin{cases} \boldsymbol{T} : \nabla \mathbf{w} \, d\mathbf{x}, & \text{on } \cup_E \Omega_E, \\ \left(\displaystyle\int_0^1 \boldsymbol{T}(\boldsymbol{\chi}) \partial_\tau \boldsymbol{\chi} \, d\tau \right) \mathbf{n} \, ds, & \text{on } \{\cup_I \Gamma_I\} \cup \{\cup_B \Gamma_B\}, \\ \mathbf{0}, & \text{on } \cup_N \{\mathbf{x}_N\}. \end{cases} \tag{2.4.2}$$

With $d\boldsymbol{\mu}$ defined by equation (2.4.2), equation (2.4.1) becomes

$$\begin{aligned} \sum_E \big(\partial_t(\mathbf{Kw}), \mathbf{v}\big)_E = &- \sum_I \left\langle \left(\int_0^1 \boldsymbol{T}(\boldsymbol{\chi}) \partial_\tau \boldsymbol{\chi} \, d\tau \right) \mathbf{n}, \mathbf{v} \right\rangle_I \\ &- \sum_B \left\langle \left(\int_0^1 \boldsymbol{T}(\boldsymbol{\chi}) \partial_\tau \boldsymbol{\chi} \, d\tau \right) \mathbf{n}, \mathbf{v} \right\rangle_B \\ &- \sum_E (\boldsymbol{T} : \nabla \mathbf{w}, \mathbf{v})_E + \sum_E (\mathbf{s}, \mathbf{v})_E \,. \end{aligned} \tag{2.4.3}$$

Splitting $\boldsymbol{T}$ using equation (2.3.4) gives

$$\begin{cases} \displaystyle\sum_E \big(\partial_t(\mathbf{K}\mathbf{w}), \mathbf{v}\big)_E = \sum_I \left\langle [\![\mathbf{F}]\!]\mathbf{n} - \left(\int_0^1 \boldsymbol{G}(\boldsymbol{\chi})\partial_\tau \boldsymbol{\chi}\, d\tau\right)\mathbf{n}, \mathbf{v} \right\rangle_I \\ \qquad\qquad + \displaystyle\sum_B \left\langle [\![\mathbf{F}]\!]\mathbf{n} - \left(\int_0^1 \boldsymbol{G}(\boldsymbol{\chi})\partial_\tau \boldsymbol{\chi}\, d\tau\right)\mathbf{n}, \mathbf{v} \right\rangle_B \\ \qquad\qquad - \displaystyle\sum_E \left(\nabla\cdot\mathbf{F} + \boldsymbol{G} : \nabla\mathbf{w} - \mathbf{s}, \mathbf{v}\right)_E, \\ \displaystyle\sum_E \big(\mathbf{w}(t_0,\cdot), \mathbf{v}\big)_E = \sum_E (\mathbf{w}_0, \mathbf{v})_E \,. \end{cases} \tag{2.4.4}$$

This is the alternative weak formulation.

Now consider seeking an approximate weak solution $\mathbf{w}_{hp} \in \mathcal{W}_{hp}$. Since the test function $\mathbf{v}$ is double-valued on the set $\{\cup_I \Gamma_I\} \cup \{\cup_B \Gamma_B\}$, an appropriate numerical flux $\hat{\mathbf{v}}$ must be supplied. This numerical flux is chosen in [153] such that the DG formulation with nonconservative products reduces to the conservative DG formulation whenever $\boldsymbol{G}_{hp} = \boldsymbol{G}(\mathbf{w}_{hp})$ is the Jacobian of some tensor $\mathbf{Q}_{hp}$. To this end, Rhebergen *et al.* [153] prove that $\hat{\mathbf{v}} = \{\!\{\mathbf{v}\}\!\}$ satisfies this requirement. Thus, $\mathbf{v}$ may be replaced with $\{\!\{\mathbf{v}\}\!\}$ in the boundary integrals of (2.4.4), and the divergence term in the element integral may be

integrated by parts to obtain, after some simplification,

$$\begin{cases} \displaystyle\sum_E \big(\partial_t(\mathbf{K}\mathbf{w}_{hp}), \mathbf{v}\big)_E = -\sum_I \big\langle \hat{\mathbf{f}}, [\![\mathbf{v}]\!] \big\rangle_I \\ \qquad\qquad\qquad\qquad - \displaystyle\sum_I \left\langle \left(\int_0^1 \boldsymbol{G}_{hp}(\boldsymbol{\chi}) \partial_\tau \boldsymbol{\chi} \, d\tau \right) \mathbf{n}, \{\!\{\mathbf{v}\}\!\} \right\rangle_I \\ \qquad\qquad\qquad\qquad - \displaystyle\sum_B \left\langle \hat{\mathbf{f}} + \left(\int_0^1 \boldsymbol{G}_{hp}(\boldsymbol{\chi}) \partial_\tau \boldsymbol{\chi} \, d\tau \right) \mathbf{n}, \mathbf{v}^{(\mathrm{in})} \right\rangle_B \\ \qquad\qquad\qquad\qquad + \displaystyle\sum_E \Big\{ (\Pi \mathbf{F}_{hp}, \nabla \mathbf{v})_E + \big(\Pi(\mathbf{g}_{hp} + \mathbf{s}_{hp}), \mathbf{v}\big)_E \Big\}, \\ \displaystyle\sum_E \big(\mathbf{w}(t_0, \cdot), \mathbf{v}\big)_E = \sum_E (\Pi \mathbf{w}_0, \mathbf{v})_E \,, \end{cases} \tag{2.4.5}$$

where $\mathbf{g}_{hp} = (0, gH_{hp}\nabla b_{hp}^\top, 0)^\top$ and $\hat{\mathbf{f}}$ is a numerical flux to be defined in Sections 2.4.2 and 2.4.3.

2.4.1 Choice of Path Function

The derivation thus far has been independent of the exact form of the path function $\boldsymbol{\chi}$. However, with $\mathbf{w}_{hp}$ regularized near the element boundaries in this manner, the value of the regularized nonconservative product, and hence the value of the path integral, is ultimately dependent in the limit on the choice of path; see, for example, [49] or [153]. As a consequence, equation (2.4.5) cannot be further simplified until a suitable form of $\boldsymbol{\chi}$ is chosen.

Several investigators have studied the effect of the path choice on the numerical solution. Rhebergen *et al.* [153] experimented with polynomial paths of various orders. Additional trials were done by Toumi [177]. The effect on the numerical solution was found to be small, and that having a good numerical integration scheme to integrate the path integral appeared to be of greater importance [153]. With this result in mind, a linear path will be used in the

implementation:

$$\boldsymbol{\chi}(\tau) = \mathbf{w}_{hp}^{(\mathrm{in})} + \tau(\mathbf{w}_{hp}^{(\mathrm{ex})} - \mathbf{w}_{hp}^{(\mathrm{in})}).$$

This choice of path allows for easy evaluation of the path integrals appearing in equation (2.4.5). Define

$$\mathbf{v}_{\mathrm{nc}} = \left(\int_0^1 \boldsymbol{G}_{hp}(\boldsymbol{\chi}) \partial_\tau \boldsymbol{\chi} \, d\tau \right) \mathbf{n} = (0, g\{\{H_{hp}\}\}[\![b_{hp}]\!]\mathbf{n}^\top, 0)^\top$$

on both internal and boundary edges. Then equation (2.4.5) can be rewritten, and the initial-boundary value problem (2.1.4) becomes:

Find $\mathbf{w}_{hp} \in \mathcal{W}_{hp}$ *such that*

$$\begin{cases} \displaystyle\sum_E \big(\partial_t(\mathbf{K}\mathbf{w}_{hp}), \mathbf{v}\big)_E = -\sum_I \Big\{ \big\langle \hat{\mathbf{f}}, [\![\mathbf{v}]\!] \big\rangle_I + \langle \mathbf{v}_{\mathrm{nc}}, \{\{\mathbf{v}\}\} \rangle_I \Big\} \\ \qquad\qquad\qquad\qquad - \displaystyle\sum_B \big\langle \hat{\mathbf{f}} + \mathbf{v}_{\mathrm{nc}}, \mathbf{v}^{(\mathrm{in})} \big\rangle_B \\ \qquad\qquad\qquad\qquad + \displaystyle\sum_E \Big\{ (\Pi \mathbf{F}_{hp}, \nabla \mathbf{v})_E + \big(\Pi(\mathbf{g}_{hp} + \mathbf{s}_{hp}), \mathbf{v}\big)_E \Big\}, \\ \displaystyle\sum_E \big(\mathbf{w}(t_0, \cdot), \mathbf{v}\big)_E = \sum_E (\Pi \mathbf{w}_0, \mathbf{v})_E \,, \end{cases} \tag{2.4.6}$$

for all $\mathbf{v} \in \mathcal{W}_{hp}$.

This is the semi-discrete formulation of interest in the model implementation.

2.4.2 The Numerical Flux (Split Formulation)

To close (2.4.6), it remains to define an appropriate (stable) numerical flux $\hat{\mathbf{f}}$. In this section, the formulations for the numerical flux function $\hat{\mathbf{f}}$ differ between the hydrodynamic and sedimentary components of equation (2.4.6). That is,

$$\hat{\mathbf{f}} = \big(\hat{\mathbf{f}}_{\mathrm{hy}}^\top, \hat{f}_{\mathrm{sed}}\big)^\top,$$

where $\hat{\mathbf{f}}_{\text{hy}}$ and $\hat{f}_{\text{sed}}$ are the numerical fluxes for the hydrodynamic and sedimentary components of (2.4.6), respectively. As discussed in [153], the form of the hydrodynamic flux may be thought of as a sum of an average term involving the hydrodynamic components of $\mathbf{F}_{hp}$, a stabilizing (viscous) term involving $[\![\mathbf{w}_{hp}]\!]$, and an additional stabilizing term involving $\mathbf{v}_{\text{nc}}$, the value of the path integral, which accounts for the nonconservative product. The function $\hat{\mathbf{f}}_{\text{hy}}$ is defined, following [153], as

$$\hat{\mathbf{f}}_{\text{hy}} = \begin{cases} \mathbf{F}_{hp}^{(\text{in})}\mathbf{n} - \frac{1}{2}\mathbf{v}_{\text{nc}} & S^{(\text{in})} > 0 \\ \hat{\mathbf{f}}_{\text{HLL}} - \dfrac{S^{(\text{in})} + S^{(\text{ex})}}{2\big(S^{(\text{ex})} - S^{(\text{in})}\big)}\mathbf{v}_{\text{nc}} & S^{(\text{in})} < 0 < S^{(\text{ex})} \\ \mathbf{F}_{hp}^{(\text{ex})}\mathbf{n} + \frac{1}{2}\mathbf{v}_{\text{nc}} & S^{(\text{ex})} < 0 \end{cases}, \tag{2.4.7}$$

where the quantities

$$S^{(\text{in})} = \min\{\min_i \lambda_i^{(\text{in})}, \min_i \lambda_i^{(\text{ex})}\}$$
$$S^{(\text{ex})} = \max\{\max_i \lambda_i^{(\text{in})}, \max_i \lambda_i^{(\text{ex})}\}$$

represent the "truncated" speeds of the slowest- and fastest-moving characteristics in the normal direction, respectively, $\lambda_i^{(\text{in})}$ and $\lambda_i^{(\text{ex})}$ are the eigenvalues of the hydrodynamic components of $\boldsymbol{T}^{(\text{in})} \cdot \mathbf{n}$ and $\boldsymbol{T}^{(\text{ex})} \cdot \mathbf{n}$, respectively, and

$$\hat{\mathbf{f}}_{\text{HLL}} = \frac{S^{(\text{ex})}\mathbf{F}_{hp}^{(\text{in})}\mathbf{n} - S^{(\text{in})}\mathbf{F}_{hp}^{(\text{ex})}\mathbf{n}}{S^{(\text{ex})} - S^{(\text{in})}} - \frac{S^{(\text{in})}S^{(\text{ex})}}{S^{(\text{ex})} - S^{(\text{in})}}[\![\mathbf{w}_{hp}]\!] \tag{2.4.8}$$

is the Harten-Lax-van Leer (HLL) numerical flux defined in [83]. It should be noted that for most problems in shallow water hydrodynamics, the Froude number rarely[3] exceeds 0.2, and therefore only the second case listed in equation (2.4.7) is frequently encountered [187]. It is emphasized once again that

[3] An exception would be flow across external and internal barriers (described in Section 2.5.1), and possibly in estuarine regions where H is very small, but not small enough for the region to be fully dry.

only the hydrodynamic components of $\mathbf{w}_{hp}$, $\mathbf{F}_{hp}$, and $\mathbf{v}_{\text{nc}}$ are considered in equations (2.4.7) and (2.4.8); the sedimentary component is ignored.

It can be shown (see [117, 118]) that the eigenvalues of the hydrodynamic part of $\boldsymbol{T} \cdot \mathbf{n}$ are given by

$$\begin{aligned}
\lambda_1 &= \frac{\mathbf{q}}{H} \cdot \mathbf{n}, \\
\lambda_2 &= \lambda_1 - \sqrt{gH}, \\
\lambda_3 &= \lambda_1 + \sqrt{gH},
\end{aligned}$$

and therefore

$$\begin{aligned}
S^{(\text{in})} &= \min\{\lambda_2^{(\text{in})}, \lambda_2^{(\text{ex})}\}, \\
S^{(\text{ex})} &= \max\{\lambda_3^{(\text{in})}, \lambda_3^{(\text{ex})}\}.
\end{aligned}$$

For the sedimentary component of equation (2.4.6), an upwind flux is used, based on the assumption that transport is always in the direction of the flow. This choice of numerical flux is known to work well in practice [101], and as such was introduced into the model implementation at an early date. It is defined as

$$\hat{f}_{\text{sed}} = \begin{cases} \tilde{\mathbf{q}}^{(\text{in})} \cdot \mathbf{n}, & \mathbf{q}_{\text{Roe}} \cdot \mathbf{n} \geq 0, \\ \tilde{\mathbf{q}}^{(\text{ex})} \cdot \mathbf{n}, & \mathbf{q}_{\text{Roe}} \cdot \mathbf{n} < 0, \end{cases}$$

where

$$\mathbf{q}_{\text{Roe}} = \frac{\mathbf{q}^{(\text{in})}\sqrt{H^{(\text{in})}} + \mathbf{q}^{(\text{ex})}\sqrt{H^{(\text{ex})}}}{\sqrt{H^{(\text{in})}} + \sqrt{H^{(\text{ex})}}}$$

is the so-called "Roe-averaged" value of $\mathbf{q}$; consult [101, 117, 118, 156] for additional details and remarks.

This formulation of the numerical flux is used in the numerical test cases described in Sections 4.1 through 4.4, and is shown to be effective. However, for the final test case described in Section 4.5, a modified numerical flux is used. This is the subject of the next section.

2.4.3 The NCP Numerical Flux

Although the split formulation for the numerical flux defined in the previous section appears to work satisfactorily in practice, it is desirable, and basically more correct, to employ a unified formulation for $\hat{\mathbf{f}}$ that properly accounts for the additional characteristic that appears as a result of the presence of advecting sediment within the seawater column. More precisely, the numerical flux is defined in [172] as

$$\hat{\mathbf{f}} = \begin{cases} \mathbf{F}_{hp}^{(\mathrm{in})}\mathbf{n} - \frac{1}{2}\mathbf{v}_{\mathrm{nc}}, & S^{(\mathrm{in})} > 0, \\ \hat{\mathbf{f}}_{\mathrm{HLL}} - \dfrac{S^{(\mathrm{in})} + S^{(\mathrm{ex})}}{2\big(S^{(\mathrm{ex})} - S^{(\mathrm{in})}\big)}\mathbf{v}_{\mathrm{nc}}, & S^{(\mathrm{in})} < 0 < S^{(\mathrm{ex})}, \\ \mathbf{F}_{hp}^{(\mathrm{ex})}\mathbf{n} + \frac{1}{2}\mathbf{v}_{\mathrm{nc}}, & S^{(\mathrm{ex})} < 0, \end{cases} \tag{2.4.9}$$

where the quantities

$$S^{(\mathrm{in})} = \min\{\min_i \lambda_i^{(\mathrm{in})}, \min_i \lambda_i^{(\mathrm{ex})}\}$$
$$S^{(\mathrm{ex})} = \max\{\max_i \lambda_i^{(\mathrm{in})}, \max_i \lambda_i^{(\mathrm{ex})}\}$$

represent the speeds of the slowest- and fastest-moving characteristics in the normal direction, respectively, $\lambda_i^{(\mathrm{in})}$ and $\lambda_i^{(\mathrm{ex})}$ are the (approximate) eigenvalues of $\boldsymbol{T}^{(\mathrm{in})} \cdot \mathbf{n}$ and $\boldsymbol{T}^{(\mathrm{ex})} \cdot \mathbf{n}$, respectively, and

$$\hat{\mathbf{f}}_{\mathrm{HLL}} = \frac{S^{(\mathrm{ex})}\mathbf{F}_{hp}^{(\mathrm{in})}\mathbf{n} - S^{(\mathrm{in})}\mathbf{F}_{hp}^{(\mathrm{ex})}\mathbf{n}}{S^{(\mathrm{ex})} - S^{(\mathrm{in})}} - \frac{S^{(\mathrm{in})}S^{(\mathrm{ex})}}{S^{(\mathrm{ex})} - S^{(\mathrm{in})}}\big([\![H_{hp}]\!], [\![\mathbf{q}_{hp}]\!]^\top, -[\![b_{hp}]\!]\big)^\top \tag{2.4.10}$$

is the Harten-Lax-van Leer (HLL) numerical flux defined in [83]. Note that all components of $\mathbf{w}_{hp}$, $\mathbf{F}_{hp}$, and $\mathbf{v}_{\mathrm{nc}}$ are considered in equation (2.4.9), unlike in the previous section.

The four eigenvalues of $\boldsymbol{T} \cdot \mathbf{n}$ are found from its characteristic polynomial, which takes the form

$$\left(\lambda - \frac{\mathbf{q}}{H} \cdot \mathbf{n}\right)(\mathfrak{a}\lambda^3 + \mathfrak{b}\lambda^2 + \mathfrak{c}\lambda + \mathfrak{d}) = 0, \tag{2.4.11}$$

where

$$
\begin{aligned}
\mathfrak{a} &= 1, \\
\mathfrak{b} &= -\left(\frac{2\mathbf{q}}{H} + \frac{\partial \tilde{\mathbf{q}}}{\partial b}\right) \cdot \mathbf{n}, \\
\mathfrak{c} &= \left(\frac{\mathbf{q}}{H} \cdot \mathbf{n}\right)^2 - gH\left[\frac{1}{\kappa}\left(\frac{\partial \tilde{\mathbf{q}}}{\partial \mathbf{q}} \cdot \mathbf{n}\right) \cdot \mathbf{n} + 1\right] + 2\left(\frac{\mathbf{q}}{H} \cdot \mathbf{n}\right)\left(\frac{\partial \tilde{\mathbf{q}}}{\partial b} \cdot \mathbf{n}\right), \\
\mathfrak{d} &= -\frac{gH}{\kappa}\left[\left(\frac{\partial \tilde{\mathbf{q}}}{\partial H} \cdot \mathbf{n}\right) + \left(\frac{\mathbf{q}}{H} \cdot \mathbf{t}\right)\left(\frac{\partial \tilde{\mathbf{q}}}{\partial \mathbf{q}} \cdot \mathbf{t}\right) \cdot \mathbf{n}\right] \\
&\quad + \left[gH - \left(\frac{\mathbf{q}}{H} \cdot \mathbf{n}\right)^2\right]\left(\frac{\partial \tilde{\mathbf{q}}}{\partial b} \cdot \mathbf{n}\right),
\end{aligned}
$$

for any sufficiently smooth sediment discharge function $\tilde{\mathbf{q}}$. Note that in the expression for $\mathfrak{d}$, $\mathbf{t}$ is a unit tangent vector. Using these coefficients, the quantities

$$
\begin{aligned}
\mathfrak{Q} &= \frac{1}{9}(3\mathfrak{c} - \mathfrak{b}^2), \\
\mathfrak{R} &= \frac{1}{54}(9\mathfrak{b}\mathfrak{c} - 27\mathfrak{d} - 2\mathfrak{b}^3),
\end{aligned}
$$

may be formed, and, provided that the discriminant $\mathfrak{D} = \mathfrak{Q}^3 + \mathfrak{R}^2 < 0$, the four (real and distinct) eigenvalues are given by

$$\lambda_1 = \frac{\mathbf{q}}{H} \cdot \mathbf{n}, \tag{2.4.12}$$

$$\lambda_2 = 2\sqrt{-\mathfrak{Q}}\cos\left(\frac{\theta}{3}\right) + \frac{2}{3}\lambda_1, \tag{2.4.13}$$

$$\lambda_3 = 2\sqrt{-\mathfrak{Q}}\cos\left(\frac{1}{3}(\theta + 2\pi)\right) + \frac{2}{3}\lambda_1, \tag{2.4.14}$$

$$\lambda_4 = 2\sqrt{-\mathfrak{Q}}\cos\left(\frac{1}{3}(\theta + 4\pi)\right) + \frac{2}{3}\lambda_1, \tag{2.4.15}$$

where $\theta = \cos^{-1}(\mathfrak{R}/\sqrt{-\mathfrak{Q}^3})$.

It is readily observed that the coefficients $\mathfrak{b}$, $\mathfrak{c}$, and $\mathfrak{d}$, and hence the eigenvalues, depend strongly on $\tilde{\mathbf{q}}$. Consequently, some care must be given to

the choice of sediment discharge function, since it must be ensured that $\mathfrak{D} < 0$ for physically relevant values of $\mathbf{w}_{hp}$.

For example, suppose that $\tilde{\mathbf{q}} = H^{-3}|\mathbf{q}|^2\mathbf{q}$, where $|\cdot|$ is the standard Euclidean 2-norm, as is done in [123] and [172]. Due in part to the simplicity of this relation, it may be shown analytically that $\mathfrak{D} < 0$ for all $H > 0$ and all values of $\mathbf{q}$: Since

$$\begin{aligned}
\mathfrak{b} &= -2\lambda_1, \\
\mathfrak{c} &= \left(1 - \frac{2g}{\kappa}\right)\lambda_1^2 - g\left(\frac{|\mathbf{u}|^2}{\kappa} + H\right), \\
\mathfrak{d} &= \frac{g\lambda_1}{\kappa}(3|\mathbf{u}|^2 - 2\lambda_1^2),
\end{aligned}$$

where λ_1 is given by equation (2.4.12) and $\mathbf{u} = \mathbf{q}/H$, it follows that

$$\begin{aligned}
\mathfrak{D} &= \frac{\mathfrak{d}^2}{4} - \frac{\mathfrak{b}\mathfrak{c}\mathfrak{d}}{6} + \frac{\mathfrak{b}^3\mathfrak{d}}{27} + \frac{\mathfrak{c}^3}{27} - \frac{\mathfrak{b}^2\mathfrak{c}^2}{108} \\
&< \frac{\mathfrak{d}^2}{4} - \frac{\mathfrak{b}\mathfrak{c}\mathfrak{d}}{6} + \frac{\mathfrak{b}^3\mathfrak{d}}{27} \\
&= \frac{g\lambda_1^2}{108\kappa^2}(2\lambda_1^2 - 3|\mathbf{u}|^2)(126g\lambda_1^2 - 4\kappa\lambda_1^2 + 36gH\kappa - 45g|\mathbf{u}|^2) \\
&\leq -\frac{g|\mathbf{u}|^4}{108\kappa^2}\big((81g - 4\kappa)|\mathbf{u}|^2 + 36gH\kappa\big) \leq 0
\end{aligned}$$

since $\mathfrak{c} < 0$ and $\lambda_1^2 \leq |\mathbf{u}|^2$.

However, if a more physically realistic formulation for $\tilde{\mathbf{q}}$ is used, such as that described by Camenen and Larson (2005) in [26], then it turns out that $\mathfrak{D}$ is *not* always negative. This phenomenon is shown in Figure 2.2, where $\mathfrak{D}$ is positive in the indicated region. Note, however, that this region corresponds to unrealistic flow profiles; a groundwater flow model is more appropriate as $H/d_{50} \downarrow 0$, where d_{50} is the median sediment grain size. Since $\hat{\mathbf{f}}$ becomes very sensitive to $|\mathbf{q}|$ as $H \downarrow 0$, it is necessary to choose a sufficiently

large minimum seawater column depth $H_{\min}$ for determining dry regions (see Section 2.5.5).

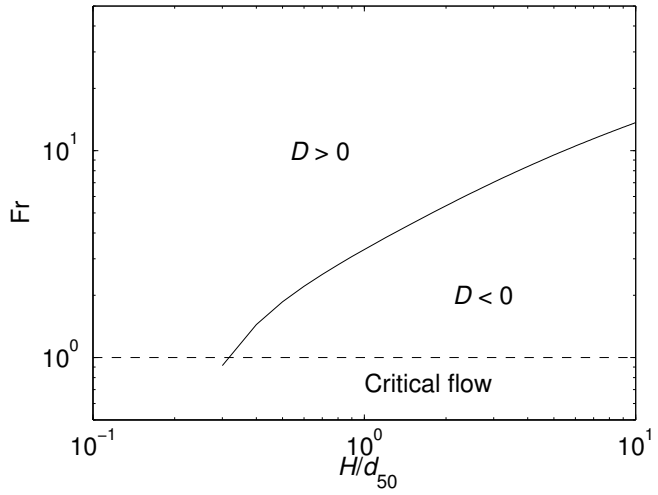

Figure 2.2: Froude numbers for which $\mathfrak{D} = 0$ using Camenen and Larson's formulation of $\tilde{\mathbf{q}}$

2.5 Implementation Overview

In this section, a brief summary of the model implementation is given. This includes details regarding the choices of boundary conditions (BCs), element types, basis functions, and time stepping schemes. For a more complete description of the current implementation of these items, consult [101] or [105].

2.5.1 Boundary Conditions

It was mentioned in Section 2.1 that the Dirichlet BC that appears in the IBVP (2.1.4) was chosen to simplify the analysis given in Chapter 3. However, in many kinds of geophysical flow problems, several other types of BCs appear. These are enforced weakly through the linear and nonlinear

numerical fluxes by specifying the values of the exterior traces (defined in Section 2.2.1) along the boundary edges. It is these BCs that are implemented in the numerical model.

There are seven types of BCs which appear in the test cases described in Chapter 4. They are as follows:

Open BCs: In regions where the open ocean intersects the domain boundary, the free surface elevation is specified, and continuity of the hydrodynamic discharge and bathymetric depth is enforced:

$$\begin{aligned} \zeta^{(\mathrm{ex})} &= \zeta_D, \\ [\![\mathbf{q}]\!] &= \mathbf{0}, \\ [\![b]\!] &= 0, \end{aligned}$$

where ζ_D is specified (typically it is a periodic function in time and is composed of several tidal harmonic constituents). For the diffusive terms, no information on $\mathbf{Z}^{(\mathrm{ex})}$ is stated, and therefore $\{\!\{\mathbf{Z}\}\!\} = \mathbf{Z}^{(\mathrm{in})}$.

Land BCs: At interfaces between seawater and either the mainland or an island, continuity of the seawater column depth and bathymetry is enforced, the *average* normal flow is set to zero, and free slip is specified:

$$\begin{aligned} [\![H]\!] &= 0, \\ \{\!\{\mathbf{q}\}\!\} \cdot \mathbf{n} &= 0, \\ [\![\mathbf{q}]\!] \cdot \mathbf{t} &= 0, \\ [\![b]\!] &= 0. \end{aligned}$$

Note that although the sedimentary flux integrals are zero, the BC for b is necessary to ensure that $\mathbf{v}_{\mathrm{nc}} = \mathbf{0}$. As with open boundaries, no action is taken with $\mathbf{Z}^{(\mathrm{ex})}$; it then follows that $\{\!\{\mathbf{Z}\}\!\} = \mathbf{Z}^{(\mathrm{in})}$.

Flow BCs: In regions where a river intersects the domain boundary, continuity of the seawater column depth and bathymetry is assumed, the normal hydrodynamic discharge is prescribed, and no slip is specified:

$$\begin{aligned} [\![H]\!] &= 0, \\ (\mathbf{q}^{(\mathrm{ex})} - \mathbf{q}_D) \cdot \mathbf{n} &= 0, \\ [\![\mathbf{q}]\!] \cdot \mathbf{t} &= \mathbf{q}^{(\mathrm{in})} \cdot \mathbf{t}, \\ [\![b]\!] &= 0, \end{aligned}$$

where $\mathbf{q}_D$ is prescribed (typically it is a periodic function also composed of tidal harmonic constituents). Again, nothing is said about $\mathbf{Z}^{(\mathrm{ex})}$; therefore $\{\!\{\mathbf{Z}\}\!\} = \mathbf{Z}^{(\mathrm{in})}$.

External barrier BCs: An external barrier is a levee, dike, weir, or other man-made object which impedes the flow across the domain boundary. When the seawater level is below the barrier height H_{ebar}, which is measured positively above the datum, negatively below, a land BC is imposed. However, when the seawater level exceeds H_{ebar}, the barrier is over-topped, the normal discharge becomes nonzero, and the flow across the barrier is supercritical. In all cases, continuity of the seawater column height and bathymetry is imposed, as well as conditional slip:

$$\begin{aligned} [\![H]\!] &= 0, \\ (\mathbf{q}^{(\mathrm{ex})} - \mathbf{q}_D) \cdot \mathbf{n} &= 0, \\ [\![\mathbf{q}]\!] \cdot \mathbf{t} &= \begin{cases} 0, & \zeta \leq H_{\mathrm{ebar}}, \\ \mathbf{q}^{(\mathrm{in})} \cdot \mathbf{t}, & \zeta > H_{\mathrm{ebar}}, \end{cases} \\ [\![b]\!] &= 0, \end{aligned}$$

where the normal discharge across the barrier is given by

$$\mathbf{q}_D \cdot \mathbf{n} = \begin{cases} -\mathbf{q}^{(\mathrm{in})} \cdot \mathbf{n}, & \zeta \leq H_{\mathrm{ebar}}, \\ R_{\mathrm{ebar}} C^S_{\mathrm{ebar}} \sqrt{\dfrac{8g}{27}} (\zeta - H_{\mathrm{ebar}})^{3/2}, & \zeta > H_{\mathrm{ebar}}, \end{cases}$$

where $R_{\mathrm{ebar}} \in [0, 1]$ is a ramping function of a specified duration, and C^S_{ebar} is the (dimensionless) coefficient of free surface supercritical flow (typically unity). The barrier is assumed to behave as a broad-crested weir [85, 114]. It is also assumed that $H_{\mathrm{ebar}} \gg -b$, so that it never becomes buried beneath the bed. In addition, the condition $\{\{\mathbf{Z}\}\} = \mathbf{0}$ is imposed.

Internal barrier BCs: An internal barrier behaves like an external barrier, except that it impedes the flow between two elements, as shown in Figure 2.3. A well-constructed jetty may act as an internal barrier, for example. For the purposes of the implementation, the internal barrier is assumed to behave as a broad-crested weir[4], allowing for the use of formulæ from [114]. In all cases, continuity of the seawater column height and bathymetry is imposed, as well as conditional slip, on both sides of the barrier:

[4]This implicitly assumes that flow across the barrier is always normal to both the "front" and "back" edges of the weir. A front edge is *always* paired with a corresponding back edge, as shown in Figure 2.3. For lone edges located at T-junctions or at the ends of internal barriers, a land BC is imposed.

Front side:

$$\begin{aligned}
[\![H]\!] &= 0, \\
(\mathbf{q}^{(\mathrm{ex})} - \mathbf{q}_D) \cdot \mathbf{n}_{\mathrm{front}} &= 0, \\
[\![\mathbf{q}]\!] \cdot \mathbf{t}_{\mathrm{front}} &= \begin{cases} 0, & \zeta \leq H_{\mathrm{ibar}} \\ \mathbf{q}^{(\mathrm{in})} \cdot \mathbf{t}_{\mathrm{front}}, & \text{otherwise} \end{cases}, \\
[\![b]\!] &= 0.
\end{aligned}$$

Back side:

$$\begin{aligned}
[\![H]\!] &= 0, \\
(\mathbf{q}^{(\mathrm{ex})} - \mathbf{q}_D) \cdot \mathbf{n}_{\mathrm{back}} &= 0, \\
[\![\mathbf{q}]\!] \cdot \mathbf{t}_{\mathrm{back}} &= \begin{cases} 0, & \zeta \leq H_{\mathrm{ibar}} \\ \mathbf{q}^{(\mathrm{in})} \cdot \mathbf{t}_{\mathrm{back}}, & \text{otherwise} \end{cases}, \\
[\![b]\!] &= 0.
\end{aligned}$$

The normal discharge across the front side of the barrier is determined by the following algorithm:

1. [Not over-topped?] If $\zeta_{\mathrm{front}} \leq H_{\mathrm{ibar}}$ and $\zeta_{\mathrm{back}} \leq H_{\mathrm{ibar}}$, then

$$\mathbf{q}_D \cdot \mathbf{n}_{\mathrm{front}} = -\mathbf{q}^{(\mathrm{in})} \cdot \mathbf{n}_{\mathrm{front}}.$$

2. [Water levels equal?] If $\zeta_{\mathrm{front}} = \zeta_{\mathrm{back}}$, then

$$\mathbf{q}_D \cdot \mathbf{n}_{\mathrm{front}} = -\mathbf{q}^{(\mathrm{in})} \cdot \mathbf{n}_{\mathrm{front}}.$$

3. [Over-topped at front?] If $\zeta_{\mathrm{front}} > \zeta_{\mathrm{back}}$ and $\zeta_{\mathrm{front}} > H_{\mathrm{ibar}}$, then determine whether the flow is sub- or supercritical:

   (a) [Subcritical flow?] If $\zeta_{\mathrm{back}} - H_{\mathrm{ibar}} > \frac{2}{3}(\zeta_{\mathrm{front}} - H_{\mathrm{ibar}})$, then

$$\mathbf{q}_D \cdot \mathbf{n}_{\mathrm{front}} = R_{\mathrm{ibar}} C^s_{\mathrm{ibar}} (\zeta_{\mathrm{back}} - H_{\mathrm{ibar}}) \sqrt{2g(\zeta_{\mathrm{front}} - \zeta_{\mathrm{back}})}.$$

(b) Otherwise, the flow is supercritical, and

$$\mathbf{q}_D \cdot \mathbf{n}_{\text{front}} = R_{\text{ibar}} C^S_{\text{ibar}} \sqrt{\frac{8g}{27}} (\zeta_{\text{front}} - H_{\text{ibar}})^{3/2}.$$

4. [Over-topped at back?] If $\zeta_{\text{back}} > \zeta_{\text{front}}$ and $\zeta_{\text{back}} > H_{\text{ibar}}$, then determine whether the flow is sub- or supercritical:

   (a) [Subcritical flow?] If $\zeta_{\text{front}} - H_{\text{ibar}} > \frac{2}{3}(\zeta_{\text{back}} - H_{\text{ibar}})$, then

   $$\mathbf{q}_D \cdot \mathbf{n}_{\text{front}} = -R_{\text{ibar}} C^s_{\text{ibar}} (\zeta_{\text{front}} - H_{\text{ibar}}) \sqrt{2g(\zeta_{\text{back}} - \zeta_{\text{front}})}.$$

   (b) Otherwise, the flow is supercritical, and

   $$\mathbf{q}_D \cdot \mathbf{n}_{\text{front}} = -R_{\text{ibar}} C^S_{\text{ibar}} \sqrt{\frac{8g}{27}} (\zeta_{\text{back}} - H_{\text{ibar}})^{3/2}.$$

An analogous algorithm holds for the back side of the barrier. Here, $R_{\text{ibar}} \in [0, 1]$ is a ramping function of specified duration; C^s_{ibar}, the coefficient of free surface subcritical flow (typically unity); C^S_{ibar}, the coefficient of free surface supercritical flow (also typically unity), and ζ_{front} and ζ_{back}, the interior traces of the free surface elevations at the front and back sides, respectively. Similar to external barriers, it is assumed that $H_{\text{ibar}} \gg -b$ on both sides, so that the internal barrier never becomes buried beneath the bed. In addition, the condition $\{\{\mathbf{Z}\}\} = \mathbf{0}$ is imposed.

Radiation (Sommerfield) BCs: On these boundaries, information about the bed, seawater column height, and flow is allowed to freely propagate out of the domain without reflection. Thus, the jump in the solution is zero:

$$[\![\mathbf{w}]\!] = \mathbf{0}.$$

In addition, the condition $\{\{\mathbf{Z}\}\} = \mathbf{0}$ is imposed here.

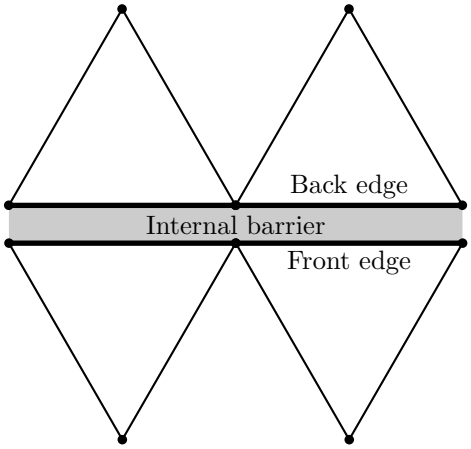

Figure 2.3: An internal barrier boundary between triangular elements

Periodic BCs: For the test case described in Section 4.1, the domain is rectangular, and the seawater column height, bathymetry, and flow are assumed to be periodic:

$$\mathbf{w}^{(\mathrm{ex})}(x) = \mathbf{w}^{(\mathrm{in})}(x + \lambda),$$
$$\mathbf{w}^{(\mathrm{ex})}(x + \lambda) = \mathbf{w}^{(\mathrm{in})}(x),$$

where $\lambda > 0$ is the period (domain length in the x-direction). Note that for that test case, the diffusion terms are identically zero, so no conditions for $\mathbf{Z}$ are needed.

For all test cases, the boundary conditions must be carefully chosen. For example, for the test case described in Section 4.2, it was found that imposing a radiation BC on the downstream boundary instead of an open BC resulted in a net gain of global seawater mass. Although not the focus of this dissertation, the proper specification of boundary conditions is the subject of ongoing research by many investigators [101, 187].

2.5.2 Elements and Affine Mappings

Recall from Section 2.2 that each element Ω_E is assumed to be triangular. This choice of element allows for greater flexibility when handling unstructured meshes, such as those used in the numerical examples described in Chapter 4. On each element Ω_E, the LDG solution pair $\mathbf{w}_{hp}$ and $\mathbf{Z}_{hp}$ may be expanded as

$$\mathbf{w}_{hp}(t,\mathbf{x})|_{\Omega_E} = \mathbf{W}_{hp,E}(t)\cdot\boldsymbol{\phi}(\mathbf{x}), \tag{2.5.1}$$

$$\mathbf{Z}_{hp}(t,\mathbf{x})|_{\Omega_E} = \boldsymbol{Z}_{hp,E}(t)\cdot\boldsymbol{\phi}(\mathbf{x}), \tag{2.5.2}$$

where $\mathbf{W}_{hp,E}\in\mathbb{R}^{4\times N}$ and $\boldsymbol{Z}_{hp,E}\in\mathbb{R}^{4\times 2\times N}$ are tensors which contain the local degrees of freedom of $\mathbf{w}_{hp}$ and $\mathbf{Z}_{hp}$, respectively,

$$N = \frac{1}{2}(p+1)(p+2)$$

is the number of degrees of freedom on each element, and $\boldsymbol{\phi}(\mathbf{x})\in\mathbb{R}^N$ is a vector of basis functions on the physical element, defined in terms of the basis functions on the master triangular element $\hat{\boldsymbol{\phi}}(\boldsymbol{\xi})$ through an affine mapping $G_E:\hat{\Omega}\to\Omega_E$ as

$$\boldsymbol{\phi}(\mathbf{x}) = \hat{\boldsymbol{\phi}}\big(G_E^{-1}(\mathbf{x})\big),$$

where $\hat{\Omega}$ is the master triangular element defined by

$$\hat{\Omega} = \{(\xi_1,\xi_2)\in\mathbb{R}^2 : \xi_1 > -1, \xi_2 > -1, \xi_1+\xi_2 < 0\}.$$

The map G_E is defined as follows. Let (x_1,y_1), (x_2,y_2), and (x_3,y_3) be the vertices of Ω_E, in counterclockwise order. Then

$$G_E(\boldsymbol{\xi}) = -\frac{1}{2}\begin{pmatrix} x_1-x_2 & x_1-x_3 \\ y_1-y_2 & y_1-y_3\end{pmatrix}\boldsymbol{\xi} + \frac{1}{2}\begin{pmatrix} x_2+x_3 \\ y_2+y_3\end{pmatrix}.$$

Thus, the inverse of this map is given by

$$G_E^{-1}(\mathbf{x}) = \frac{1}{|\Omega_E|}\begin{pmatrix} y_3 - y_1 & x_1 - x_3 \\ y_1 - y_2 & x_2 - x_1 \end{pmatrix}\left[\mathbf{x} - \frac{1}{2}\begin{pmatrix} x_2 + x_3 \\ y_2 + y_3 \end{pmatrix}\right],$$

where $|\Omega_E|$ is the area of Ω_E.

2.5.3 Basis Functions and the Mass Matrix

Substituting the expansions (2.5.1) and (2.5.2) into the discrete weak systems (2.2.6) and (2.4.6), and taking the test functions to be $\boldsymbol{\phi}$ yields an algebraic linear system of ODEs

$$\sum_E \frac{d}{dt}(\mathbf{K}\mathbf{W}_{hp,E})\mathbf{M}_E = \sum_E \mathbf{R}(\mathbf{W}_{hp,E}, \boldsymbol{Z}_{hp,E}) \tag{2.5.3}$$

as well as an auxiliary system

$$\sum_E \boldsymbol{Z}_{hp,E}\mathbf{M}_E = \sum_E \boldsymbol{R}_a(\mathbf{W}_{hp,E}), \tag{2.5.4}$$

where $\mathbf{M}_E \in \mathbb{R}^{N\times N}$ is the elemental mass matrix, and the tensors $\mathbf{R} \in \mathbb{R}^{4\times N}$ and $\boldsymbol{R}_a \in \mathbb{R}^{4\times 2\times N}$ denote the remaining terms on the right-hand sides of the primary and auxiliary equations in (2.2.6), respectively.

In order to solve the systems (2.5.3) and (2.5.4) for $\mathbf{W}_{hp,E}$ and $\boldsymbol{Z}_{hp,E}$, respectively, the mass matrix $\mathbf{M}_E$ must be inverted. Using an $\mathcal{L}_2(\hat{\Omega})$-orthogonal basis reduces the mass matrix $\mathbf{M}_E$ to a diagonal one, which may be trivially inverted. For this reason, a hierarchical basis with the $\mathcal{L}_2(\hat{\Omega})$-orthogonality property proposed by Dubiner [65] has been implemented. For future reference, the first six basis functions and the corresponding values of the mass matrix on the master element (denoted by M_d) are given in Table 2.1; a concise general formulation may be found in [101].

d	$\hat{\phi}_d(\xi_1, \xi_2)$	M_d
1	1	2
2	$\frac{1}{2} + \frac{3}{2}\xi_2$	1
3	$\frac{1}{2} + \xi_1 + \frac{1}{2}\xi_2$	$\frac{1}{3}$
4	$-\frac{1}{2} + \xi_2 + \frac{5}{2}\xi_2^2$	$\frac{2}{3}$
5	$\frac{3}{4} + \frac{3}{2}\xi_1 + 2\xi_2 + \frac{5}{2}\xi_1\xi_2 + \frac{5}{4}\xi_2^2$	$\frac{2}{9}$
6	$\frac{1}{4} + \frac{3}{2}\xi_1 + \xi_2 + \frac{3}{2}\xi_1^2 + \frac{3}{2}\xi_1\xi_2 + \frac{1}{4}\xi_2^2$	$\frac{2}{15}$

Table 2.1: The first six Dubiner basis functions

2.5.4 Timestepping Scheme

Solving equation (2.5.3) requires the use of an appropriate time stepping scheme once $\mathbf{M}_E^{-1}$ is determined. The time stepping scheme utilized herein is an explicit strong-stability preserving (SSP) s-stage, kth-order Runge–Kutta (RK) scheme, where the pair (s, k) is one of $(1, 1)$, $(s, 2)$ with $s \geq 2$, $(s, 3)$ with $3 \leq s \leq 8$, or $(s, 4)$ with $5 \leq s \leq 8$. The SSP RK scheme is designed so that if the forward Euler method is stable under a given semi-norm and Courant–Friedrichs–Lewy (CFL) condition, then the higher-order scheme remains stable under the same semi-norm, but perhaps under a different CFL condition [101]. These methods also possess the desirable TVD property. This time stepping method takes the following general form[5]:

Algorithm 2.5.1 (SSP RK scheme)**.** *Given initial data* $\mathbf{W}_{hp,E}(t_0)$ *(which contains the local degrees of freedom of* $\Pi\mathbf{w}_0$*), an element* Ω_E*, the number of stages* s *and order* k*, this algorithm computes the DG solution* $\mathbf{W}_{hp,E}$ *at a given final time* $t_0 + T$*.*

[5]The algorithm presentation, style, and notation was inspired by Knuth [97].

1. *[Initialize.] Set* $n \leftarrow 0$*, so that* $t = t_0$*.*

2. *[Modify IC.] Set* $\mathbf{W}_{hp,E}^{(0)} \leftarrow (\Lambda\Pi)(M\Pi)\mathbf{W}_{hp,E}(t_0)$*. (That is, apply the wetting and drying operator, and then apply the slope limiting operator.)*

3. *[Reset.] Set* $i \leftarrow 1$*.*

4. *[Auxiliary solve.] Set* $\mathbf{Z}_{hp,E}^{(i-1)} \leftarrow \mathbf{R}_a(\mathbf{W}_{hp,E}^{(i-1)})\mathbf{M}_E^{-1}$*.*

5. *[Primary solve.] Set*

$$\mathbf{W}_{hp,E}^{(i)} \leftarrow \sum_{j=1}^{i} \Big\{ \alpha_{ij}\mathbf{W}_{hp,E}^{(j-1)} + \beta_{ij}\Delta t\mathbf{K}^{-1}\mathbf{R}\big(\mathbf{W}_{hp,E}^{(j-1)}, \mathbf{Z}_{hp,E}^{(j-1)}, t_n + \delta_j\Delta t\big)\mathbf{M}_E^{-1} \Big\}.$$

6. *[Wet/dry and slope limit.] Set* $\mathbf{W}_{hp,E}^{(i)} \leftarrow (\Lambda\Pi)(M\Pi)\mathbf{W}_{hp,E}^{(i)}$*. (At this point* $\mathbf{W}_{hp,E}^{(i)}$ *is the DG solution at RK stage* i*.)*

7. *[More stages?] If* $i = s$*, set* $\mathbf{W}_{hp,E}(t_{n+1}) \leftarrow \mathbf{W}_{hp,E}^{(s)}$*; otherwise increase* i *by 1 and go back to step 4.*

8. *[Repeat?] If* $n = \lfloor T/\Delta t + 0.5 \rfloor - 1$*, the algorithm terminates with* $\mathbf{W}_{hp,E}(t_{n+1})$ *as the DG solution at time* $t_0 + T$*; otherwise increment* n *by 1 and go back to step 3.*

In the algorithm above, $(\Lambda\Pi)$ and $(M\Pi)$ are the slope limiting and wetting and drying operators (described in the next section), respectively, $\delta_j = \sum_{k=1}^{j-1} \gamma_{j-1,k}$ is a vector of length s of time-lagging parameters, and the $s \times s$ matrices $\boldsymbol{\alpha}$, $\boldsymbol{\beta}$, and $\boldsymbol{\gamma}$ are optimized parameters with respect to maximization

of the CFL number. They satisfy the TVD constraints

$$\begin{aligned} \alpha_{ij} &\geq 0, \\ \sum_{j=1}^{i} \alpha_{ij} &= 1, \\ \gamma_{ij} &= \beta_{ij} + \sum_{k=j}^{i-1} \gamma_{kj} \alpha_{i,k+1}. \end{aligned}$$

To be clear, it should be noted that Algorithm 2.5.1 must be performed for each degree of freedom on every element Ω_E. Refer to [101, 105, 163] for further details on SSP RK methods, and to [102] for values of $\boldsymbol{\alpha}$ and $\boldsymbol{\beta}$.

2.5.5 Post-processing Operations

The remainder of this chapter is devoted to remarks on the use of two post-processing operators, namely the slope limiting operator ($\Lambda\Pi$), and the wetting and drying operator ($M\Pi$). These operations are applied in steps 2 and 6 of Algorithm 2.5.1.

To eliminate local overshoots and undershoots, five different choices of slope limiters are implemented. They are as follows:

1. Minmod (described in [101]),
2. Characteristic-based TVB [44],
3. Modified characteristic-based TVB [24, 44],
4. Higher-order WENO [193],
5. Vertex-based.

However, only limiters 1 and 4 will be used in the numerical results presented in Chapter 4; some of the others are notorious for degrading the solution to first-order accuracy at local extrema (effectively $p = 0$ in these regions), and it is desirable to test the implementation with $p \geq 0$ in the examples listed in Chapter 4. Thus, when $p = 1$, limiter 1 is used if needed. This is the case for the entire morphodynamic system in Section 4.3, and for the sediment transport equation in Section 4.4. But when $p > 1$, it becomes necessary to make use of a higher-order slope limiting procedure. For this dissertation, the algorithm outlined in the work by Xu *et al.* [193] is implemented, which is a local limiting procedure based on the application of a WENO-type limiter to the coefficients of the higher-order Taylor series expansion about the barycenter of Ω_E. It has been shown to work well in practice [193]. For the sake of brevity, the implementation details shall not be expounded upon here, and the interested reader may refer to Sections 2.1, 2.2, 2.3, and 2.5 of [193]. It was found to be necessary to apply limiter 4 only to the sediment transport equation for the test cases described in Sections 4.2 and 4.4. For the remaining test cases, it was found that limiting was unnecessary in order to preserve numerical stability. That is, $(\Lambda\Pi) = I$ in those cases.

Consider equation (2.1.2). Several components of $\mathbf{F}(\mathbf{w})$ contain a singularity when $H \downarrow 0$. For this reason, as well as those described at the conclusion of Section 2.4.3, and for reasons elaborated in the next chapter, it is necessary to select an appropriate value of $H_{\min}$, the minimum seawater column depth, below which H cannot drop. When $H \downarrow H_{\min}$, an element or node may become dry, in which case both hydrodynamic and sedimentary discharge is either zeroed out or limited [24]. This action is described by the operator $(M\Pi)$. As a general rule, the wetting and drying algorithm under consideration does *not*

conserve linear momentum, although it does conserve seawater and sediment mass. For implementation details, consult [24]. It should be noted that the first four test cases described in Chapter 4 are designed so that $(M\Pi) = I$; a nontrivial application of the wetting and drying algorithm may be found in Section 4.5.

Chapter 3

An *A Priori* Error Estimate

This chapter contains the analysis of the LDG approximation to the full system of the SWE, coupled with equations which also model bed morphology due to sediment transport. The LDG method was originally developed for the Navier–Stokes equations by Bassi and Rebay [15], and analyzed for linear advection-diffusion equations by Cockburn and Shu [43]. Aizinger and Dawson [2] first applied the method to the depth-averaged SWE and later to three-dimensional hydrostatic shallow water models [3]. Some basic analysis of the LDG method applied to a linearized model was done in [1]. Application of the LDG method to the morphodynamics problem described herein was recently studied numerically in [132]. Several collaborators have formulated and analyzed DG and coupled continuous/discontinuous methods for the SWE in a series of papers [1, 3, 52, 53, 54].

In this chapter, the analysis in [1] is extended to the full nonlinear SWE coupled with bed morphology. This represents to the author's knowledge the first complete *a priori* error analysis for the LDG method applied to the SWE, and the first error analysis of the method applied to morphodynamics. In addition, the analysis uses a different technique than the somewhat standard one used for time-dependent problems; the use of Grönwall's lemma is avoided in formulating the estimate and hence the exponentially large constant which results from this approach is avoided.

The outline of this chapter is as follows. Section 3.1 examines the error equation, which is analyzed and bounded in Section 3.2. Finally, a discussion of the result and potential applications appears in Section 3.3.

3.1 The Error Equation

The error equation is one of the key relations needed to perform the *a priori* error analysis in the next section [1, 54]. To derive this relation, subtract (2.2.3) from (2.2.6), which gives

$$\begin{aligned}
\sum_E \big(\mathbf{K}\partial_t(\mathbf{w}_{hp}-\mathbf{w}),\mathbf{v}\big)_E = &-\sum_I \big\langle(\{\{\Pi\mathbf{F}_{hp}\}\}-\mathbf{F})\mathbf{n}+\boldsymbol{\sigma}[\![\mathbf{w}_{hp}-\mathbf{w}]\!],[\![\mathbf{v}]\!]\big\rangle_I \\
&-\sum_I \big\langle(\{\{\mathbf{Z}_{hp}\}\}-\mathbf{Z})\mathbf{n},[\![\mathbf{v}]\!]\big\rangle_I \\
&-\sum_B \big\langle\big(\Pi\mathbf{F}_{hp}^{(\mathrm{in})}-\mathbf{F}\big)\mathbf{n}+\boldsymbol{\sigma}\big(\mathbf{w}_{hp}^{(\mathrm{in})}-\mathbf{w}\big),\mathbf{v}^{(\mathrm{in})}\big\rangle_B \\
&-\sum_B \big\langle\big(\mathbf{Z}_{hp}^{(\mathrm{in})}-\mathbf{Z}\big)\mathbf{n},\mathbf{v}^{(\mathrm{in})}\big\rangle_B \\
&+\sum_E (\Pi\mathbf{F}_{hp}-\mathbf{F}+\mathbf{Z}_{hp}-\mathbf{Z},\nabla\mathbf{v})_E \\
&+\sum_E (\Pi\mathbf{g}_{hp}-\mathbf{g}+\Pi\mathbf{s}_{hp}-\mathbf{s},\mathbf{v})_E\,, \qquad (3.1.1)\\
\sum_E (\mathbf{Z}_{hp}-\mathbf{Z},\mathbf{V})_E = &-\sum_I \big\langle\{\{\mathbf{w}_{hp}\}\}-\mathbf{w},(\mathsf{D}:[\![\mathbf{V}]\!])\mathbf{n}\big\rangle_I \\
&+\sum_E \big(\mathbf{w}_{hp}-\mathbf{w},\nabla\cdot(\mathsf{D}:\mathbf{V})\big)_E, \qquad (3.1.2)\\
\sum_E \big((\mathbf{w}_{hp}-\mathbf{w})(t_0,\cdot),\mathbf{v}\big)_E &= \sum_E (\Pi\mathbf{w}_0-\mathbf{w}_0,\mathbf{v})_E = 0. \qquad (3.1.3)
\end{aligned}$$

Notice that in equation (3.1.1), $\mathbf{w}$ has been added to the stabilization terms appearing inside the interior and boundary edge integrals. This is a harmless operation, since it is assumed that $[\![\mathbf{w}]\!] = \mathbf{0}$ on all edges. Observe also that

because of the choice of boundary conditions, no boundary edge integrals appear in equation (3.1.2). This result has consequences for the analysis in the next section. Finally, it is seen that equation (3.1.3) simply states that the finite element solution at the initial time is the best approximation to the true solution at the initial time.

Equations (3.1.1)–(3.1.3) are written in terms of the total error in the finite element solution. This can be decomposed into the approximation error

$$\boldsymbol{\psi} = \mathbf{w}_{hp} - \Pi\mathbf{w}, \tag{3.1.4}$$

$$\boldsymbol{\Psi} = \mathbf{Z}_{hp} - \Pi\mathbf{Z}, \tag{3.1.5}$$

and the projection error

$$\boldsymbol{\theta} = \mathbf{w} - \Pi\mathbf{w}, \tag{3.1.6}$$

$$\boldsymbol{\Theta} = \mathbf{Z} - \Pi\mathbf{Z}, \tag{3.1.7}$$

where $\Pi\mathbf{w}(t,\cdot)$ and $\Pi\mathbf{Z}(t,\cdot)$ are the $\mathcal{L}_2(\Omega_E)$-projections of $\mathbf{w}(t,\cdot)$ and $\mathbf{Z}(t,\cdot)$ into the polynomial spaces $\mathcal{W}_{hp}$ and $\mathcal{Z}_{hp}$ for any fixed time t, respectively:

$$\left(\boldsymbol{\theta}, \mathbf{v}\right)_E = 0 \qquad \text{for all } \mathbf{v} \in \mathcal{W}_{hp}, \tag{3.1.8}$$

$$\left(\boldsymbol{\Theta}, \mathbf{V}\right)_E = 0 \qquad \text{for all } \mathbf{V} \in \mathcal{Z}_{hp}. \tag{3.1.9}$$

Using the relations (3.1.4)–(3.1.7) together with (3.1.8) and (3.1.9), equa-

tions (3.1.1)–(3.1.3) may be written as

$$\begin{aligned}\sum_E (\mathbf{K}\partial_t\boldsymbol{\psi},\mathbf{v})_E = &-\sum_I \big\langle (\{\!\{\Pi\mathbf{F}_{hp}\}\!\}-\mathbf{F})\mathbf{n}+\boldsymbol{\sigma}[\![\boldsymbol{\psi}-\boldsymbol{\theta}]\!]+\{\!\{\boldsymbol{\Psi}-\boldsymbol{\Theta}\}\!\}\mathbf{n},[\![\mathbf{v}]\!]\big\rangle_I\\ &-\sum_B \big\langle (\Pi\mathbf{F}_{hp}^{(\mathrm{in})}-\mathbf{F})\mathbf{n}+\boldsymbol{\sigma}(\boldsymbol{\psi}^{(\mathrm{in})}-\boldsymbol{\theta}^{(\mathrm{in})}),\mathbf{v}^{(\mathrm{in})}\big\rangle_B\\ &-\sum_B \big\langle (\boldsymbol{\Psi}^{(\mathrm{in})}-\boldsymbol{\Theta}^{(\mathrm{in})})\mathbf{n},\mathbf{v}^{(\mathrm{in})}\big\rangle_B\\ &+\sum_E (\Pi\mathbf{F}_{hp}-\mathbf{F}+\boldsymbol{\Psi},\nabla\mathbf{v})_E\\ &+\sum_E (\Pi\mathbf{g}_{hp}-\mathbf{g}+\Pi\mathbf{s}_{hp}-\mathbf{s},\mathbf{v})_E\,, \end{aligned}\tag{3.1.10}$$

$$\sum_E (\boldsymbol{\Psi},\mathbf{V})_E = -\sum_I \big\langle \{\!\{\boldsymbol{\psi}-\boldsymbol{\theta}\}\!\},(\mathsf{D}:[\![\mathbf{V}]\!])\mathbf{n}\big\rangle_I + \sum_E \big(\boldsymbol{\psi},\nabla\cdot(\mathsf{D}:\mathbf{V})\big)_E,\tag{3.1.11}$$

$$\sum_E \big(\boldsymbol{\psi}(t_0,\cdot),\mathbf{v}\big)_E = 0.\tag{3.1.12}$$

Setting $\mathbf{v}=\boldsymbol{\psi}$ and $\mathbf{V}=\boldsymbol{\Psi}$, eliminating terms using the integration by parts formula, adding equations (3.1.10) and (3.1.11) together, and rearranging terms yields

$$\begin{aligned}0 = &\frac{1}{2}\frac{d}{dt}\big\|\mathbf{K}^{1/2}\boldsymbol{\psi}\big\|_{0,h}^2+\|\boldsymbol{\Psi}\|_{0,h}^2+\tau_{\mathrm{bf}}\Big(\|\psi_2\|_{0,h}^2+\|\psi_3\|_{0,h}^2\Big)\\ &+\sum_I \big\|\boldsymbol{\sigma}^{1/2}[\![\boldsymbol{\psi}]\!]\big\|_{0,I}^2+\sum_B \big\|\boldsymbol{\sigma}^{1/2}\boldsymbol{\psi}^{(\mathrm{in})}\big\|_{0,B}^2-\sum_E (\Pi\mathbf{F}_{hp}-\mathbf{F},\nabla\boldsymbol{\psi})_E\\ &+\sum_I \big\langle (\{\!\{\Pi\mathbf{F}_{hp}\}\!\}-\mathbf{F})\mathbf{n},[\![\boldsymbol{\psi}]\!]\big\rangle_I+\sum_B \big\langle \big(\Pi\mathbf{F}_{hp}^{(\mathrm{in})}-\mathbf{F}\big)\mathbf{n},\boldsymbol{\psi}^{(\mathrm{in})}\big\rangle_B\\ &-\sum_I \langle \boldsymbol{\sigma}[\![\boldsymbol{\theta}]\!],[\![\boldsymbol{\psi}]\!]\rangle_I-\sum_B \big\langle \boldsymbol{\sigma}\boldsymbol{\theta}^{(\mathrm{in})},\boldsymbol{\psi}^{(\mathrm{in})}\big\rangle_B-\sum_I \langle \{\!\{\boldsymbol{\Theta}\}\!\}\mathbf{n},[\![\boldsymbol{\psi}]\!]\rangle_I\\ &-\sum_B \big\langle \boldsymbol{\Theta}^{(\mathrm{in})}\mathbf{n},\boldsymbol{\psi}^{(\mathrm{in})}\big\rangle_B-\sum_I \big\langle \{\!\{\boldsymbol{\theta}\}\!\},(\mathsf{D}:[\![\boldsymbol{\Psi}]\!])\mathbf{n}\big\rangle_I-\sum_E (\Pi\mathbf{g}_{hp}-\mathbf{g},\boldsymbol{\psi})_E\\ &+\varrho^{-1}\sum_E \Big\{\big((\psi_1-\theta_1)\partial_x P,\psi_2\big)_E+\big((\psi_1-\theta_1)\partial_y P,\psi_3\big)_E\Big\}. \end{aligned}$$

Observe the disappearance of the wind and wave radiation stress terms, since these are empirically-derived relations that do not depend on either $\mathbf{w}$ or $\mathbf{Z}$, as well as equation (3.1.12). The above equation may be written more simply as

$$\frac{1}{2}\frac{d}{dt}\left\|\mathbf{K}^{1/2}\boldsymbol{\psi}\right\|_{0,h}^2 + \|\boldsymbol{\Psi}\|_{0,h}^2 + \tau_{\text{bf}}\left(\|\psi_2\|_{0,h}^2 + \|\psi_3\|_{0,h}^2\right) + \sum_I \left\|\boldsymbol{\sigma}^{1/2}[\![\boldsymbol{\psi}]\!]\right\|_{0,I}^2 + \sum_B \left\|\boldsymbol{\sigma}^{1/2}\boldsymbol{\psi}^{(\text{in})}\right\|_{0,B}^2 = \sum_{n=1}^{10} R_n. \quad (3.1.13)$$

Equation (3.1.13) is the so-called "error equation"; the left-hand side is written solely in terms of the approximation error.

3.2 Error Analysis

At this point, one is now in a position to derive the error estimate. Traditionally, this has been done in a very straightforward manner by first integrating the error equation, such as equation (3.1.13), in time over the interval $[t_0, t_0 + T]$ and then bounding all the terms on the right-hand side (in our case terms R_1 through R_{10}). However, this approach inevitably requires the use of the differential form of Grönwall's lemma, which results in an exponentially large bounding constant in the final estimate. This is impractical from a computational point of view.

In this dissertation, the following strategy is adopted in order to circumvent this problem, and thus tighten the bound:

1. Partition the time interval $[t_0, t_0+T]$ into M sub-intervals of length ΔT_m for $1 \leq m \leq M$, where M is a sufficiently large positive integer, so that

each ΔT_m is sufficiently small, and

$$[t_0, t_0 + T] = [t_0, t_M] = \bigcup_{m=1}^{M} [t_{m-1}, t_m].$$

2. Bound the terms R_1 through R_{10} on each time sub-interval, beginning with the first sub-interval $[t_0, t_1]$.

3. Take the maximum over all time sub-intervals of the approximation error, and drop all penalty terms on the left-hand side, to obtain the result.

Assume that step 1 above has been followed. The next step is to proceed to step 2 and consider the first time interval $[t_0, t_1]$, so that $m = 1$. Define the quantities

$$\|\psi_i(t_{1i}, \cdot)\|_{0,h} = \max_{t \in [t_0, t_1]} \|\psi_i(t, \cdot)\|_{0,h} = \|\psi_i\|_{\mathcal{L}_\infty(t_0, t_1; \mathcal{L}_2(\Omega_h))}$$

for $i \in \{1, 2, 3, 4\}$, and let $t_1^* = t_0 + \max_i t_{1i}$. Integrating equation (3.1.13) in time from t_0 to $t_0 + t_{1i}$ for each value of i yields a set of four error equations, each with a right-hand side bounded by the quantity $\int_{t_0}^{t_1^*} \left| \sum_{n=1}^{10} R_n \right| dt$. Then it follows that

$$\frac{1}{2} K_{ii} \|\psi_i(t_{1i}, \cdot)\|_{0,h}^2 \leq \int_{t_0}^{t_1^*} \left| \sum_{n=1}^{10} R_n \right| dt + \frac{1}{2} K_{ii} \|\psi_i(t_0, \cdot)\|_{0,h}^2 \qquad \text{for } 1 \leq i \leq 4$$

and

$$\int_{t_0}^{t_1^*} \left\{ \|\boldsymbol{\Psi}\|_{0,h}^2 + \sum_I \left\| \boldsymbol{\sigma}^{1/2} [\![\boldsymbol{\psi}]\!] \right\|_{0,I}^2 + \sum_B \left\| \boldsymbol{\sigma}^{1/2} \boldsymbol{\psi}^{(\text{in})} \right\|_{0,B}^2 \right\} dt \leq \int_{t_0}^{t_1^*} \left| \sum_{n=1}^{10} R_n \right| dt,$$

where the term involving $\psi_i(t_0, \cdot)$ has been retained for later discussion, even

though it is zero. Therefore

$$\frac{1}{2}\sum_i K_{ii}\left\|\psi_i(t_{1i},\cdot)\right\|_{0,h}^2 + \int_{t_0}^{t_1^*}\left\{\left\|\boldsymbol{\Psi}\right\|_{0,h}^2 + \sum_I \left\|\boldsymbol{\sigma}^{1/2}[\![\boldsymbol{\psi}]\!]\right\|_{0,I}^2 + \sum_B \left\|\boldsymbol{\sigma}^{1/2}\boldsymbol{\psi}^{(\mathrm{in})}\right\|_{0,B}^2\right\} dt \leq 4\int_{t_0}^{t_1^*}\left|\sum_{n=1}^{10} R_n\right| dt + \frac{1}{2}\sum_i K_{ii}\left\|\psi_i(t_0,\cdot)\right\|_{0,h}^2 . \quad (3.2.1)$$

Before bounding the terms R_1 through R_{10} over $[t_0, t_1]$, it should be noted that the following four inequalities involving scalar "cross-terms", which all hold on each element Ω_E for any value of $\Delta T_1 > 0$ and $\epsilon > 0$, will prove useful in the analysis that follows:

$$\int_{t_0}^{t_1^*}\left\|\psi_i\right\|_{0,E}\left\|\psi_k\right\|_{0,E}\, dt \leq \frac{\Delta T_1}{2}\left\|\psi_i(t_{1i},\cdot)\right\|_{0,E}^2 + \frac{\Delta T_1}{2}\left\|\psi_k(t_{1k},\cdot)\right\|_{0,E}^2 , \quad (3.2.2)$$

$$\int_{t_0}^{t_1^*}\left\|\theta_i\right\|_{0,E}\left\|\psi_k\right\|_{0,E}\, dt \leq \epsilon\int_{t_0}^{t_1^*}\left\|\theta_i\right\|_{0,E}^2\, dt + \frac{\Delta T_1}{4\epsilon}\left\|\psi_k(t_{1k},\cdot)\right\|_{0,E}^2 , \quad (3.2.3)$$

$$\int_{t_0}^{t_1^*}\left\|\Psi_{ij}\right\|_{0,E}\left\|\psi_k\right\|_{0,E}\, dt \leq \epsilon\int_{t_0}^{t_1^*}\left\|\Psi_{ij}\right\|_{0,E}^2\, dt + \frac{\Delta T_1}{4\epsilon}\left\|\psi_k(t_{1k},\cdot)\right\|_{0,E}^2 , \quad (3.2.4)$$

$$\int_{t_0}^{t_1^*}\left\|\Theta_{ij}\right\|_{0,E}\left\|\psi_k\right\|_{0,E}\, dt \leq \epsilon\int_{t_0}^{t_1^*}\left\|\Theta_{ij}\right\|_{0,E}^2\, dt + \frac{\Delta T_1}{4\epsilon}\left\|\psi_k(t_{1k},\cdot)\right\|_{0,E}^2 . \quad (3.2.5)$$

These relations follow directly from Young's inequality, and it is envisaged that these hold when both the parameter ϵ and the time interval length ΔT_1 are chosen to be sufficiently small.

To bound the right-hand side of equation (3.2.1), one must make use of the following results which may be found in many standard texts on the mathematical theory of the finite element method [20, 37]:

Theorem 3.2.1 (Trace inequality)**.** *Suppose that an element Ω_E has a Lipschitz boundary. Then there exists a constant $C_{\mathrm{tr},E}$ such that*

$$\|f\|_{0,\partial\Omega_E} \leq C_{\mathrm{tr},E} \|f\|_{0,E}^{1/2} \|f\|_{1,E}^{1/2}$$

for every $f \in \mathcal{H}^1(\Omega_E)$.

Note that if one defines the trace constant $C_{\mathrm{tr}} = \sup_h \max_E C_{\mathrm{tr},E}$, this can be shown to be finite for regular meshes, including triangular, quadrilateral, or hybrid meshes. Two immediate consequences of Theorem 3.2.1 are

$$\sum_I \|f\|_{0,I}^2 \leq C_{\mathrm{tr}}^2 \sum_E \|f\|_{0,E} \|f\|_{1,E},$$
$$\sum_B \|f\|_{0,B}^2 \leq C_{\mathrm{tr}}^2 \sum_E \|f\|_{0,E} \|f\|_{1,E};$$

extensive use is made of these facts in the analysis below.

Theorem 3.2.2 (Inverse inequality)**.** *For a regular, quasi-uniform mesh, there exists a constant C_{inv} independent of h such that*

$$\|f\|_{1,E} \leq C_{\mathrm{inv}} h^{-1} \|f\|_{0,E}$$

for every $f \in \mathcal{X}_{hp}$.

Theorem 3.2.3 (Approximation error bound)**.** *Let Πf denote the $\mathcal{L}_2(\Omega_E)$-projection of $f \in \mathcal{H}^r(\Omega_E)$ into the space $\mathcal{P}^p(\Omega_E)$. Then there exists a constant K independent of h such that*

$$\|f - \Pi f\|_{\ell,E} \leq K h^{\min\{r,p+1\}-\ell} \|f\|_{r,E},$$

where $0 \leq \ell \leq \min\{r, p+1\}$.

The right-hand side of equation (3.2.1) by now be bounded. Terms R_1 through R_3 involve the nonlinear fluxes, which require much more scrutiny, and so are treated separately from the remaining terms:

$$\int_{t_0}^{t_1^*} \left| \sum_{n=1}^{10} R_n \right| dt \leq \int_{t_0}^{t_1^*} \left\{ |R_1 + R_2 + R_3| + \sum_{n=4}^{10} |R_n| \right\} dt.$$

Term R_1 may be integrated by parts to obtain

$$\begin{aligned} R_1 &= \sum_E (\Pi \mathbf{F}_{hp} - \mathbf{F}, \nabla \boldsymbol{\psi})_E = \sum_E \big(\Pi(\mathbf{F}_{hp} - \mathbf{F}), \nabla \boldsymbol{\psi}\big)_E \\ &= \sum_I \big\langle \{\!\{\Pi(\mathbf{F}_{hp} - \mathbf{F})\}\!\}\mathbf{n}, [\![\boldsymbol{\psi}]\!] \big\rangle_I + \sum_B \big\langle \Pi\big(\mathbf{F}_{hp}^{(\mathrm{in})} - \mathbf{F}\big)\mathbf{n}, \boldsymbol{\psi}^{(\mathrm{in})} \big\rangle_B \\ &\quad - \sum_E \big(\nabla \cdot \Pi(\mathbf{F}_{hp} - \mathbf{F}), \boldsymbol{\psi}\big)_E + \sum_I \big\langle [\![\Pi(\mathbf{F}_{hp} - \mathbf{F})]\!]\mathbf{n}, \{\!\{\boldsymbol{\psi}\}\!\} \big\rangle_I \\ &= R_{1,1} + R_{1,2} + R_{1,3} + R_{1,4}. \end{aligned}$$

Let $\boldsymbol{\Theta}_{\mathbf{F}} = \mathbf{F} - \Pi\mathbf{F}$ denote the flux projection error. Then

$$\begin{aligned} R_2 &= -\sum_I \big\langle (\{\!\{\Pi \mathbf{F}_{hp}\}\!\} - \mathbf{F})\mathbf{n}, [\![\boldsymbol{\psi}]\!] \big\rangle_I \\ &= -\sum_I \big\langle \{\!\{\Pi(\mathbf{F}_{hp} - \mathbf{F})\}\!\}\mathbf{n} - \{\!\{\boldsymbol{\Theta}_{\mathbf{F}}\}\!\}\mathbf{n}, [\![\boldsymbol{\psi}]\!] \big\rangle_I \\ &= R_{2,1} + R_{2,2}, \end{aligned}$$

and similarly,

$$\begin{aligned} R_3 &= -\sum_B \big\langle \big(\Pi \mathbf{F}_{hp}^{(\mathrm{in})} - \mathbf{F}\big)\mathbf{n}, \boldsymbol{\psi}^{(\mathrm{in})} \big\rangle_B \\ &= -\sum_B \big\langle \Pi\big(\mathbf{F}_{hp}^{(\mathrm{in})} - \mathbf{F}\big)\mathbf{n} - \boldsymbol{\Theta}_{\mathbf{F}}^{(\mathrm{in})}\mathbf{n}, \boldsymbol{\psi}^{(\mathrm{in})} \big\rangle_B \\ &= R_{3,1} + R_{3,2}. \end{aligned}$$

Notice that $R_{1,1} + R_{2,1} = 0$ and $R_{1,2} + R_{3,1} = 0$, and so

$$R_1 + R_2 + R_3 = R_{1,3} + R_{1,4} + R_{2,2} + R_{3,2}.$$

Next comes one of the more difficult parts of the analysis, which lies in the treatment of the sub-terms $R_{1,3} + R_{1,4}$. The aim is to invoke equation (3.1.11), at least in some form. However, since the morphodynamic system is incompletely parabolic, the first component of equation (3.1.11) is zero. Therefore, the first component of $R_{1,3}+R_{1,4}$ is split off and bounded separately:

$$\begin{aligned} R_{1,3} + R_{1,4} = &- \sum_E \big(\nabla \cdot (\psi_2, \psi_3)^\top, \psi_1\big)_E + \sum_I \big\langle [\![(\psi_2, \psi_3)^\top]\!] \cdot \mathbf{n}, \{\!\{ \psi_1 \}\!\} \big\rangle_I \\ &- \sum_E \sum_{i>1} \big(\partial_x \Pi(F_{i1,hp} - F_{i1}) + \partial_y \Pi(F_{i2,hp} - F_{i2}), \psi_i\big)_E \\ &+ \sum_I \sum_{i>1} \big\langle [\![\Pi(F_{i1,hp} - F_{i1})]\!] n_x + [\![\Pi(F_{i2,hp} - F_{i2})]\!] n_y, \{\!\{ \psi_i \}\!\} \big\rangle_I \\ = &\, R_{1,3,1} + R_{1,4,1} + R_{1,3,2} + R_{1,4,2}, \end{aligned}$$

since $\Pi(\mathbf{q}_{hp} - \mathbf{q}) = (\psi_2, \psi_3)^\top$. Now consider terms $R_{1,3,1}$ and $R_{1,3,2}$, which involve the linear part of the flux. After integrating term $R_{1,3,1}$ by parts, the result is

$$\begin{aligned} R_{1,3,1} + R_{1,4,1} = &- \sum_I \big\langle \{\!\{ (\psi_2, \psi_3)^\top \}\!\} \cdot \mathbf{n}, [\![\psi_1]\!] \big\rangle_I \\ &- \sum_B \big\langle \big(\psi_2^{(\mathrm{in})}, \psi_3^{(\mathrm{in})}\big)^\top \cdot \mathbf{n}, \psi_1^{(\mathrm{in})} \big\rangle_B + \sum_E \big((\psi_2, \psi_3)^\top, \nabla \cdot \widehat{\mathbf{V}}\big)_E, \end{aligned}$$

where $\widehat{\mathbf{V}} = \psi_1 \mathbf{I}$, so that $\nabla \cdot \widehat{\mathbf{V}} = \nabla \psi_1$. The second and third components of equation (3.1.11) may now be invoked, since the relation $\widehat{\mathbf{V}} = \mathsf{H} : \mathbf{V}|_{i \in \{2,3\}}$ may now be substituted. After doing so, some tedious manipulation, which

involves the cancellation of the first component of term $R_{2,2}$, yields the relation

$$\begin{aligned} R_{1,3,1} + R_{1,4,1} + R_{2,2} = &- \sum_{B} \left\langle \left(\psi_2^{(\text{in})}, \psi_3^{(\text{in})}\right)^\top, \psi_1^{(\text{in})}\mathbf{n} \right\rangle_B \\ &+ \sum_{E} \left\{ \left(\Psi_{21}, \nu_x^{-1}\psi_1\right)_E + \left(\Psi_{32}, \nu_y^{-1}\psi_1\right)_E \right\} \\ &+ \sum_{I} \sum_{i>1} \left\langle \{\!\{\Theta_{\mathbf{F},i1}\}\!\} n_x + \{\!\{\Theta_{\mathbf{F},i2}\}\!\} n_y, [\![\psi_i]\!] \right\rangle_I \\ = &\, \widehat{R}_1 + \widehat{R}_2 + \widehat{R}_4. \end{aligned}$$

The dissection of terms $R_1 + R_2 + R_3$ is now complete; they may now be bounded. Let $\widehat{R}_3 = R_{1,3,2} + R_{1,4,2}$ and $\widehat{R}_5 = R_{3,2}$. Noting that

$$\int_{t_0}^{t_1^*} |R_1 + R_2 + R_3| \, dt \leq \int_{t_0}^{t_1^*} \left\{ \left|\widehat{R}_1\right| + \left|\widehat{R}_2\right| + \left|\widehat{R}_3\right| + \left|\widehat{R}_4\right| + \left|\widehat{R}_5\right| \right\} dt,$$

the first observation is

$$\begin{aligned}
\int_{t_0}^{t_1^*} \left|\widehat{R}_1\right| dt &= \int_{t_0}^{t_1^*} \left| \sum_B \left\langle \left(\psi_2^{(\mathrm{in})}, \psi_3^{(\mathrm{in})}\right)^\top, \psi_1^{(\mathrm{in})} \mathbf{n} \right\rangle_B \right| dt \\
&\leq \int_{t_0}^{t_1^*} \sum_B \left| \left\langle \sigma_{22}^{1/2} \psi_2^{(\mathrm{in})}, \sigma_{22}^{-1/2} \psi_1^{(\mathrm{in})} n_x \right\rangle_B \right| dt \\
&\quad + \int_{t_0}^{t_1^*} \sum_B \left| \left\langle \sigma_{33}^{1/2} \psi_3^{(\mathrm{in})}, \sigma_{33}^{-1/2} \psi_1^{(\mathrm{in})} n_y \right\rangle_B \right| dt \\
&\leq \int_{t_0}^{t_1^*} \sum_B \left\| \sigma_{22}^{1/2} \psi_2^{(\mathrm{in})} \right\|_{0,B} \left\| \sigma_{22}^{-1/2} \psi_1^{(\mathrm{in})} n_x \right\|_{0,B} dt \\
&\quad + \int_{t_0}^{t_1^*} \sum_B \left\| \sigma_{33}^{1/2} \psi_3^{(\mathrm{in})} \right\|_{0,B} \left\| \sigma_{33}^{-1/2} \psi_1^{(\mathrm{in})} n_y \right\|_{0,B} dt \\
&\leq \epsilon \int_{t_0}^{t_1^*} \sum_B \left\{ \left\| \sigma_{22}^{1/2} \psi_2^{(\mathrm{in})} \right\|_{0,B}^2 + \left\| \sigma_{33}^{1/2} \psi_3^{(\mathrm{in})} \right\|_{0,B}^2 \right\} dt \\
&\quad + \frac{1}{4\epsilon} \int_{t_0}^{t_1^*} \sum_B \left\{ \left\| \sigma_{22}^{-1/2} \psi_1^{(\mathrm{in})} n_x \right\|_{0,B}^2 + \left\| \sigma_{33}^{-1/2} \psi_1^{(\mathrm{in})} n_y \right\|_{0,B}^2 \right\} dt \\
&\leq C_{\mathrm{tr}}^2 C_{\mathrm{inv}} \frac{\Delta T_1}{2\epsilon} \left\| \psi_1(t_{11}, \cdot) \right\|_{0,h}^2 + \epsilon \int_{t_0}^{t_1^*} \sum_B \left\| \boldsymbol{\sigma}^{1/2} \boldsymbol{\psi}^{(\mathrm{in})} \right\|_{0,B}^2 dt, \quad (3.2.6)
\end{aligned}$$

which is obtained after applying Schwarz's inequality twice (once for each component), Young's inequality twice, Theorems 3.2.1 and 3.2.2 in succession (to each of the latter two terms), and equation (3.2.2) once. Since both σ_{22}^{-1} and σ_{33}^{-1} are of the order h as $h \downarrow 0$, they cancel the h^{-1} that appears as a result of invoking Theorem 3.2.2.

Two applications of equation (3.2.4) yield

$$\begin{aligned}
\int_{t_0}^{t_1^*} \left|\widehat{R}_2\right| dt &= \int_{t_0}^{t_1^*} \left| \sum_E \left\{ \left(\Psi_{21}, \nu_x^{-1}\psi_1\right)_E + \left(\Psi_{32}, \nu_y^{-1}\psi_1\right)_E \right\} \right| dt \\
&\leq \sum_E \int_{t_0}^{t_1^*} \left\{ \nu_x^{-1} \left\|\Psi_{21}\right\|_{0,E} + \nu_y^{-1} \left\|\Psi_{32}\right\|_{0,E} \right\} \left\|\psi_1\right\|_{0,E} \, dt \\
&\leq \epsilon \int_{t_0}^{t_1^*} \sum_E \left\{ \left\|\Psi_{21}\right\|_{0,E}^2 + \left\|\Psi_{32}\right\|_{0,E}^2 \right\} dt \\
&\quad + \frac{\Delta T_1}{4\epsilon} \left(\nu_x^{-2} + \nu_y^{-2}\right) \sum_E \left\|\psi_1(t_{11}, \cdot)\right\|_{0,E}^2 \\
&\leq \frac{\Delta T_1}{4\epsilon} \left(\nu_x^{-2} + \nu_y^{-2}\right) \left\|\psi_1(t_{11}, \cdot)\right\|_{0,h}^2 + \epsilon \int_{t_0}^{t_1^*} \left\|\mathbf{\Psi}\right\|_{0,h}^2 \, dt. \qquad (3.2.7)
\end{aligned}$$

The second, third, and fourth components of equation (3.1.11) may be applied directly to term $R_{1,3,2}$ in order to treat $\widehat{R}_3$:

$$\begin{aligned}
\int_{t_0}^{t_1^*} \left|\widehat{R}_3\right| dt \leq & \int_{t_0}^{t_1^*} \sum_E \left| \left(\Psi_{21}, \nu_x^{-1}\Pi(F_{hp,21} - F_{21})\right)_E \right| dt \\
& + \int_{t_0}^{t_1^*} \sum_E \left| \left(\Psi_{22}, \nu_y^{-1}\Pi(F_{hp,22} - F_{22})\right)_E \right| dt \\
& + \int_{t_0}^{t_1^*} \sum_E \left| \left(\Psi_{31}, \nu_x^{-1}\Pi(F_{hp,31} - F_{31})\right)_E \right| dt \\
& + \int_{t_0}^{t_1^*} \sum_E \left| \left(\Psi_{32}, \nu_y^{-1}\Pi(F_{hp,32} - F_{32})\right)_E \right| dt \\
& + \int_{t_0}^{t_1^*} \sum_E \left| \left(\Psi_{41}, \tilde{\nu}_x^{-1}\Pi(F_{hp,41} - F_{41})\right)_E \right| dt \\
& + \int_{t_0}^{t_1^*} \sum_E \left| \left(\Psi_{42}, \tilde{\nu}_y^{-1}\Pi(F_{hp,42} - F_{42})\right)_E \right| dt \\
& + \int_{t_0}^{t_1^*} \sum_I \sum_{i>1} \left| \left\langle \sigma_{ii}^{1/2} \{\!\{\theta_i\}\!\}, \sigma_{ii}^{-1/2} [\![\Pi(\mathbf{F}_{hp} - \mathbf{F})|_i]\!] \cdot \mathbf{n} \right\rangle_I \right| dt.
\end{aligned}$$

Consider the first six terms on the right-hand side. Since

$$\|\Pi f\|_{0,E} \leq \|f\|_{0,E} \qquad \text{for all } f \in \mathcal{L}_2(\Omega_E),$$

it is clear that

$$\begin{aligned}\sum_E \left|\left(\Psi_{21}, \nu_x^{-1}\Pi(F_{hp,21} - F_{21})\right)_E\right| &\leq \sum_E \|\Psi_{21}\|_{0,E}\, \nu_x^{-1}\, \|F_{hp,21} - F_{21}\|_{0,E} \\ &\leq \epsilon \sum_E \|\Psi_{21}\|_{0,E}^2 + \frac{\nu_x^{-2}}{4\epsilon} \sum_E \|F_{hp,21} - F_{21}\|_{0,E}^2 .\end{aligned}$$

To proceed further, it must now be shown that each component of $\mathbf{F}$ is Lipschitz-continuous in all its arguments. This will enable the expression of $\|F_{hp,ij} - F_{ij}\|_{0,E}$ in terms of $\boldsymbol{\psi}$ and $\boldsymbol{\theta}$. For the linear parts of $\mathbf{F}$, it is clear that

$$\|F_{hp,1j} - F_{1j}\|_{0,E} \leq \|\boldsymbol{\psi} - \boldsymbol{\theta}\|_{0,E} \qquad \text{for } j = 1, 2,$$

with Lipschitz constants $L_{11} = L_{12} = 1$. It can be shown that

$$\begin{aligned}\|F_{hp,21} - F_{21}\|_{0,E} &\leq L_{21}\, \|\boldsymbol{\psi} - \boldsymbol{\theta}\|_{0,E} , \\ \|F_{hp,22} - F_{22}\|_{0,E} &\leq L_{22}\, \|\boldsymbol{\psi} - \boldsymbol{\theta}\|_{0,E} ,\end{aligned}$$

where

$$\begin{aligned}L_{21} &= \max\left\{ \frac{\|w_2^2\|_\infty}{\|w_1\|_\infty \|w_{hp,1}\|_\infty}, \frac{\|w_2\|_\infty + \|w_{hp,2}\|_\infty}{\|w_{hp,1}\|_\infty} \right\}, \\ L_{22} &= \max\left\{ \frac{\|w_{hp,2}\|_\infty \|w_{hp,3}\|_\infty}{\|w_1\|_\infty \|w_{hp,1}\|_\infty}, \frac{\|w_{hp,3}\|_\infty}{\|w_1\|_\infty}, \frac{\|w_2\|_\infty}{\|w_1\|_\infty} \right\},\end{aligned}$$

and similarly for F_{31} and F_{32}, provided that w_2, w_2^2, w_3, w_3^2, $w_{hp,2}$, and $w_{hp,3}$ are all uniformly bounded above, and that w_1 and $w_{hp,1}$ are both uniformly bounded below, for all partitions Ω_h. Finally, since it is assumed that $\tilde{\mathbf{q}}$ is Lipschitz-continuous in all its arguments, it follows that

$$\begin{aligned}\|F_{hp,41} - F_{41}\|_{0,E} &\leq L_{41}\, \|\boldsymbol{\psi} - \boldsymbol{\theta}\|_{0,E} , \\ \|F_{hp,42} - F_{42}\|_{0,E} &\leq L_{42}\, \|\boldsymbol{\psi} - \boldsymbol{\theta}\|_{0,E} .\end{aligned}$$

Now, defining $C_L = \max_{i,j} L_{ij}$, it follows that

$$\sum_E \left| \left(\Psi_{21}, \nu_x^{-1} \Pi (F_{hp,21} - F_{21}) \right)_E \right| \\ \leq \epsilon \left\| \Psi_{21} \right\|_{0,h}^2 + \frac{\nu_x^{-2} C_L^2}{4\epsilon} \left(\sum_i \left\| \psi_i \right\|_{0,h}^2 + \sum_E \left\| \boldsymbol{\theta} \right\|_{0,E}^2 \right),$$

and similarly for the other five terms. Applying equation (3.2.2) to integrate $\left\| \psi_i \right\|_{0,h}^2$ in time gives

$$\int_{t_0}^{t_1^*} \sum_E \left| \left(\Psi_{21}, \nu_x^{-1} \Pi (F_{hp,21} - F_{21}) \right)_E \right| dt \leq \epsilon \int_{t_0}^{t_1^*} \left\| \Psi_{21} \right\|_{0,h}^2 \, dt \\ + \frac{\nu_x^{-2} C_L^2}{4\epsilon} \left(\Delta T_1 \sum_i \left\| \psi_i(t_{1i}, \cdot) \right\|_{0,h}^2 + \int_{t_0}^{t_1^*} \sum_E \left\| \boldsymbol{\theta} \right\|_{0,E}^2 \, dt \right),$$

and likewise for the other five terms. For the last term, since

$$\begin{aligned} &\int_{t_0}^{t_1^*} \sum_I \sum_{i>1} \left| \left\langle \sigma_{ii}^{1/2} \{\!\{ \theta_i \}\!\}, \sigma_{ii}^{-1/2} [\![\Pi (\mathbf{F}_{hp} - \mathbf{F})|_i]\!] \cdot \mathbf{n} \right\rangle_I \right| dt \\ &\quad \leq \int_{t_0}^{t_1^*} \sum_I \sum_{i>1} \left\| \sigma_{ii}^{1/2} \{\!\{ \theta_i \}\!\} \right\|_{0,I} \left\| \sigma_{ii}^{-1/2} [\![\Pi (\mathbf{F}_{hp} - \mathbf{F})|_i]\!] \cdot \mathbf{n} \right\|_{0,I} dt \\ &\quad \leq \int_{t_0}^{t_1^*} \sum_I \sum_{i>1} \left\{ \frac{1}{4\epsilon} \left\| \sigma_{ii}^{1/2} \{\!\{ \theta_i \}\!\} \right\|_{0,I}^2 + \epsilon \left\| \sigma_{ii}^{-1/2} [\![\Pi (\mathbf{F}_{hp} - \mathbf{F})|_i]\!] \cdot \mathbf{n} \right\|_{0,I}^2 \right\} dt \\ &\quad \leq C_{\mathrm{tr}}^2 \int_{t_0}^{t_1^*} \sum_E \left\{ \frac{h^{-1}}{4\epsilon} \sum_{i>1} \left\| \theta_i \right\|_{0,E}^2 + 6\epsilon C_L^2 C_{\mathrm{inv}} \left\| \boldsymbol{\psi} - \boldsymbol{\theta} \right\|_{0,E}^2 \right\} dt \\ &\quad \leq C_{\mathrm{tr}}^2 \left\{ \int_{t_0}^{t_1^*} \left(\frac{h^{-1}}{4\epsilon} + 6\epsilon C_L^2 C_{\mathrm{inv}} \right) \sum_E \left\| \boldsymbol{\theta} \right\|_{0,E}^2 \, dt \right. \\ &\qquad \left. + 6\epsilon C_L^2 C_{\mathrm{inv}} \Delta T_1 \sum_i \left\| \psi_i(t_{1i}, \cdot) \right\|_{0,h}^2 \right\}, \end{aligned}$$

it follows that

$$\int_{t_0}^{t_1^*} \left| \widehat{R}_3 \right| dt \leq \epsilon \int_{t_0}^{t_1^*} \left\| \boldsymbol{\Psi} \right\|_{0,h}^2 \, dt + \widehat{C} \sum_i \left\| \psi_i(t_{1i}, \cdot) \right\|_{0,h}^2 + \widehat{\widehat{C}} \int_{t_0}^{t_1^*} \sum_E \left\| \boldsymbol{\theta} \right\|_{0,E}^2 \, dt, \tag{3.2.8}$$

where

$$\widehat{C} = \left(\frac{1}{4\epsilon} \Big(2 \left(\nu_x^{-2} + \nu_y^{-2} \right) + \tilde{\nu}_x^{-2} + \tilde{\nu}_y^{-2} \Big) + 6\epsilon C_{\text{tr}}^2 C_{\text{inv}} \right) C_L^2 \Delta T_1,$$

$$\widehat{\widehat{C}} = \frac{C_L^2}{4\epsilon} \Big(2 \big(\nu_x^{-2} + \nu_y^{-2} \big) + \tilde{\nu}_x^{-2} + \tilde{\nu}_y^{-2} \Big) + C_{\text{tr}}^2 \left(\frac{h^{-1}}{4\epsilon} + 6\epsilon C_L^2 C_{\text{inv}} \right).$$

Now consider term $\widehat{R}_4$. With the aid of the penalty terms, Schwarz's inequality, Young's inequality, and Theorem 3.2.1, it is observed that

$$\begin{aligned}
\int_{t_0}^{t_1^*} \left| \widehat{R}_4 \right| dt &\leq \int_{t_0}^{t_1^*} \sum_I \sum_{i>1} \left| \left\langle \sigma_{ii}^{-1/2} \{\!\{ \boldsymbol{\Theta}_{\mathbf{F}} |_i \}\!\} \cdot \mathbf{n}, \sigma_{ii}^{1/2} [\![\psi_i]\!] \right\rangle_I \right| dt \\
&\leq \int_{t_0}^{t_1^*} \sum_I \sum_{i>1} \left\| \sigma_{ii}^{-1/2} \{\!\{ \boldsymbol{\Theta}_{\mathbf{F}} |_i \}\!\} \cdot \mathbf{n} \right\|_{0,I} \left\| \sigma_{ii}^{1/2} [\![\psi_i]\!] \right\|_{0,I} dt \\
&\leq \int_{t_0}^{t_1^*} \sum_I \sum_{i>1} \left\{ \frac{1}{4\epsilon} \left\| \sigma_{ii}^{-1/2} \{\!\{ \boldsymbol{\Theta}_{\mathbf{F}} |_i \}\!\} \cdot \mathbf{n} \right\|_{0,I}^2 + \epsilon \left\| \sigma_{ii}^{1/2} [\![\psi_i]\!] \right\|_{0,I}^2 \right\} dt \\
&\leq \epsilon \int_{t_0}^{t_1^*} \sum_I \sum_{i>1} \left\| \sigma_{ii}^{1/2} [\![\psi_i]\!] \right\|_{0,I}^2 dt \\
&\quad + \frac{C_{\text{tr}}^2}{4\epsilon} \int_{t_0}^{t_1^*} \sum_E \sum_{i>1} \left\| \sigma_{ii}^{-1/2} \boldsymbol{\Theta}_{\mathbf{F}} |_i \right\|_{0,E} \left\| \sigma_{ii}^{-1/2} \boldsymbol{\Theta}_{\mathbf{F}} |_i \right\|_{1,E} dt. \quad (3.2.9)
\end{aligned}$$

Term $\widehat{R}_5$ must be split into components, since no part of it was canceled earlier (owing to the choice of boundary conditions). For the first component, notice that $\boldsymbol{\Theta}_{\mathbf{F}}^{(\text{in})}|_{i=1} = \big(\theta_2^{(\text{in})}, \theta_3^{(\text{in})} \big)^\top$. Thus,

$$\widehat{R}_5 = \sum_B \left\{ \left\langle \big(\theta_2^{(\text{in})}, \theta_3^{(\text{in})} \big)^\top, \psi_1^{(\text{in})} \mathbf{n} \right\rangle_B + \sum_{i>1} \left\langle \boldsymbol{\Theta}_{\mathbf{F}}^{(\text{in})} |_i \cdot \mathbf{n}, \psi_i^{(\text{in})} \right\rangle_B \right\}.$$

The first subterm has the same form as term $\widehat{R}_1$; an argument similar to the one used to bound that term may be used here. For the second, third, and fourth subterms of $\widehat{R}_5$, the same procedure used to bound term $\widehat{R}_4$ may again

be used here. After some straightforward manipulations, the result is

$$\int_{t_0}^{t_1^*} \left|\widehat{R}_5\right| dt \leq C_{\rm tr}^2 C_{\rm inv} \frac{\Delta T_1}{2\epsilon} \left\|\psi_1(t_{11},\cdot)\right\|_{0,h}^2 + \epsilon \int_{t_0}^{t_1^*} \sum_B \sum_{i>1} \left\|\sigma_{ii}^{1/2}\psi_i^{(\rm in)}\right\|_{0,B}^2 dt$$
$$+ \epsilon C_{\rm tr}^2 \int_{t_0}^{t_1^*} \sum_E \sum_{i=2}^{3} \left\|\sigma_{ii}^{1/2}\theta_i\right\|_{0,E} \left\|\sigma_{ii}^{1/2}\theta_i\right\|_{1,E} dt$$
$$+ \frac{C_{\rm tr}^2}{4\epsilon} \int_{t_0}^{t_1^*} \sum_E \sum_{i>1} \left\|\sigma_{ii}^{-1/2}\boldsymbol{\Theta}_{\mathbf{F}}|_i\right\|_{0,E} \left\|\sigma_{ii}^{-1/2}\boldsymbol{\Theta}_{\mathbf{F}}|_i\right\|_{1,E} dt. \quad (3.2.10)$$

At this point, $\int_{t_0}^{t_1^*} |R_1 + R_2 + R_3|\ dt$ has been bounded, and it remains to bound $\int_{t_0}^{t_1^*} \sum_{n=4}^{10} |R_n|\ dt$. Proceeding, consider the penalty terms R_4 and R_5. These satisfy

$$\int_{t_0}^{t_1^*} |R_4|\ dt \leq \int_{t_0}^{t_1^*} \left\{ \epsilon \sum_I \left\|\boldsymbol{\sigma}^{1/2}[\![\boldsymbol{\psi}]\!]\right\|_{0,I}^2 \right.$$
$$\left. + \frac{C_{\rm tr}^2}{4\epsilon} \sum_E \sum_i \left\|\sigma_{ii}^{1/2}\theta_i\right\|_{0,E} \left\|\sigma_{ii}^{1/2}\theta_i\right\|_{1,E} \right\} dt, \quad (3.2.11)$$

and similarly,

$$\int_{t_0}^{t_1^*} |R_5|\ dt \leq \int_{t_0}^{t_1^*} \left\{ \epsilon \sum_B \left\|\boldsymbol{\sigma}^{1/2}\boldsymbol{\psi}^{(\rm in)}\right\|_{0,B}^2 \right.$$
$$\left. + \frac{C_{\rm tr}^2}{4\epsilon} \sum_E \sum_i \left\|\sigma_{ii}^{1/2}\theta_i\right\|_{0,E} \left\|\sigma_{ii}^{1/2}\theta_i\right\|_{1,E} \right\} dt. \quad (3.2.12)$$

To bound the first two diffusion terms R_6 and R_7, the same trick as that used to bound $R_{2,2}$ and $R_{3,2}$ may be applied:

$$\int_{t_0}^{t_1^*} |R_6|\ dt = \int_{t_0}^{t_1^*} \left| \sum_I \left\langle \{\!\{\boldsymbol{\Theta}\}\!\}\mathbf{n}, [\![\boldsymbol{\psi}]\!] \right\rangle_I \right| dt$$
$$\leq \epsilon \int_{t_0}^{t_1^*} \sum_I \left\|\boldsymbol{\sigma}^{1/2}[\![\boldsymbol{\psi}]\!]\right\|_{0,I}^2 dt$$
$$+ \frac{C_{\rm tr}^2}{4\epsilon} \int_{t_0}^{t_1^*} \sum_E \sum_i \left\|\sigma_{ii}^{-1/2}\boldsymbol{\Theta}|_i\right\|_{0,E} \left\|\sigma_{ii}^{-1/2}\boldsymbol{\Theta}|_i\right\|_{1,E} dt, \quad (3.2.13)$$

and, analogously,

$$\int_{t_0}^{t_1^*} |R_7| \, dt \leq \epsilon \int_{t_0}^{t_1^*} \sum_B \left\| \boldsymbol{\sigma}^{1/2} \boldsymbol{\psi}^{(\mathrm{in})} \right\|_{0,B}^2 dt + \frac{C_{\mathrm{tr}}^2}{4\epsilon} \int_{t_0}^{t_1^*} \sum_E \sum_i \left\| \sigma_{ii}^{-1/2} \boldsymbol{\Theta}|_i \right\|_{0,E} \left\| \sigma_{ii}^{-1/2} \boldsymbol{\Theta}|_i \right\|_{1,E} dt. \quad (3.2.14)$$

The last diffusion term R_8 must be handled slightly differently; the penalty terms are not used. Two applications of Theorem 3.2.1 and one of Theorem 3.2.2 yield

$$\begin{aligned}
\int_{t_0}^{t_1^*} |R_8| \, dt &= \int_{t_0}^{t_1^*} \left| \sum_I \langle \{\{\boldsymbol{\theta}\}\}, (\mathsf{D} : [\![\boldsymbol{\Psi}]\!]) \mathbf{n} \rangle_I \right| dt \\
&\leq |\mathsf{D}|_\infty \int_{t_0}^{t_1^*} \sum_I \sum_i \| \{\{\theta_i\}\} \|_{0,I} \, \| [\![\boldsymbol{\Psi}|_i]\!] \cdot \mathbf{n} \|_{0,I} \, dt \\
&\leq |\mathsf{D}|_\infty C_{\mathrm{tr}}^2 \int_{t_0}^{t_1^*} \sum_E \sum_i \left(\|\theta_i\|_{0,E}^{1/2} \, \|\theta_i\|_{1,E}^{1/2} \right) \left(\|\boldsymbol{\Psi}|_i\|_{0,E}^{1/2} \, \|\boldsymbol{\Psi}|_i\|_{1,E}^{1/2} \right) dt \\
&\leq |\mathsf{D}|_\infty C_{\mathrm{tr}}^2 C_{\mathrm{inv}}^{1/2} \int_{t_0}^{t_1^*} \sum_E \sum_i \left(h^{-1/2} \, \|\theta_i\|_{0,E}^{1/2} \, \|\theta_i\|_{1,E}^{1/2} \right) \|\boldsymbol{\Psi}|_i\|_{0,E} \, dt \\
&\leq \int_{t_0}^{t_1^*} \left\{ \epsilon \, \|\boldsymbol{\Psi}\|_{0,h}^2 + \frac{1}{4\epsilon} \, |\mathsf{D}|_\infty^2 \, C_{\mathrm{tr}}^4 C_{\mathrm{inv}} \sum_E \sum_i h^{-1} \, \|\theta_i\|_{0,E} \, \|\theta_i\|_{1,E} \right\} dt,
\end{aligned} \quad (3.2.15)$$

where $|\cdot|_\infty$ denotes the tensor maximum norm. Recall that since D is a constant tensor in space and time, $|\mathsf{D}|_\infty$ is bounded.

Next, consider term R_9, which contains the nonconservative product,

and rewrite it as follows:

$$\begin{aligned}
\int_{t_0}^{t_1^*} |R_9| \, dt &= \int_{t_0}^{t_1^*} \left| \sum_E \left(\Pi \mathbf{g}_{hp} - \mathbf{g}, \boldsymbol{\psi} \right)_E \right| dt \\
&\leq \int_{t_0}^{t_1^*} \sum_E \left| \left(-\tilde{\nu}_x^{-1} g \big(\Pi (H_{hp} Z_{41,hp}) - H Z_{41} \big), \psi_2 \right)_E \right| dt \\
&\quad + \int_{t_0}^{t_1^*} \sum_E \left| \left(-\tilde{\nu}_y^{-1} g \big(\Pi (H_{hp} Z_{42,hp}) - H Z_{42} \big), \psi_3 \right)_E \right| dt \\
&= \tilde{\nu}_x^{-1} g \int_{t_0}^{t_1^*} \sum_E \left| \left(\Pi \big(H_{hp} (\Psi_{41} - \Theta_{41}) + Z_{41} (\psi_1 - \theta_1) \big), \psi_2 \right)_E \right| dt \\
&\quad + \tilde{\nu}_y^{-1} g \int_{t_0}^{t_1^*} \sum_E \left| \left(\Pi \big(H_{hp} (\Psi_{42} - \Theta_{42}) + Z_{42} (\psi_1 - \theta_1) \big), \psi_3 \right)_E \right| dt,
\end{aligned}$$

which is an immediate consequence of the facts that

$$\begin{aligned}
\big(H Z_{41} - \Pi (H Z_{41}), \psi_2 \big)_E &= 0, \\
\big(H Z_{42} - \Pi (H Z_{42}), \psi_3 \big)_E &= 0.
\end{aligned}$$

Assuming that H_{hp}, Z_{41}, and Z_{42} are all bounded on each element in Ω_h for all $h > 0$ and for each $t \in [t_0, t_0 + T]$, then each of equations (3.2.2)–(3.2.5)

may be invoked twice to obtain, after some rearrangement,

$$\begin{aligned}
\int_{t_0}^{t_1^*} |R_9| \, dt \leq \tilde{\nu}_x^{-1} g \sum_E \int_{t_0}^{t_1^*} \|H_{hp}\|_\infty \left(\|\Psi_{41}\|_{0,E} + \|\Theta_{41}\|_{0,E} \right) \|\psi_2\|_{0,E} \, dt \\
+ \tilde{\nu}_x^{-1} g \sum_E \int_{t_0}^{t_1^*} \|Z_{41}\|_\infty \left(\|\psi_1\|_{0,E} + \|\theta_1\|_{0,E} \right) \|\psi_2\|_{0,E} \, dt \\
+ \tilde{\nu}_y^{-1} g \sum_E \int_{t_0}^{t_1^*} \|H_{hp}\|_\infty \left(\|\Psi_{42}\|_{0,E} + \|\Theta_{42}\|_{0,E} \right) \|\psi_3\|_{0,E} \, dt \\
+ \tilde{\nu}_y^{-1} g \sum_E \int_{t_0}^{t_1^*} \|Z_{42}\|_\infty \left(\|\psi_1\|_{0,E} + \|\theta_1\|_{0,E} \right) \|\psi_3\|_{0,E} \, dt \\
\leq \frac{\Delta T_1}{2} g \left(\tilde{\nu}_x^{-1} \|Z_{41}\|_\infty + \tilde{\nu}_y^{-1} \|Z_{42}\|_\infty \right) \|\psi_1(t_{11}, \cdot)\|_{0,h}^2 \\
+ \frac{\Delta T_1}{4\epsilon} g \tilde{\nu}_x^{-1} \left(2\|H_{hp}\|_\infty + (1+2\epsilon)\|Z_{41}\|_\infty \right) \|\psi_2(t_{12}, \cdot)\|_{0,h}^2 \\
+ \frac{\Delta T_1}{4\epsilon} g \tilde{\nu}_y^{-1} \left(2\|H_{hp}\|_\infty + (1+2\epsilon)\|Z_{42}\|_\infty \right) \|\psi_3(t_{13}, \cdot)\|_{0,h}^2 \\
+ \epsilon g \|H_{hp}\|_\infty \int_{t_0}^{t_1^*} \left\{ \tilde{\nu}_x^{-1} \|\Psi_{41}\|_{0,h}^2 + \tilde{\nu}_y^{-1} \|\Psi_{42}\|_{0,h}^2 \right\} dt \\
+ \epsilon g \left(\tilde{\nu}_x^{-1} \|Z_{41}\|_\infty + \tilde{\nu}_y^{-1} \|Z_{42}\|_\infty \right) \int_{t_0}^{t_1^*} \sum_E \|\theta_1\|_{0,E}^2 \, dt \\
+ \epsilon g \|H_{hp}\|_\infty \int_{t_0}^{t_1^*} \sum_E \left\{ \tilde{\nu}_x^{-1} \|\Theta_{41}\|_{0,E}^2 + \tilde{\nu}_y^{-1} \|\Theta_{42}\|_{0,E}^2 \right\} dt,
\end{aligned} \tag{3.2.16}$$

where $\| \cdot \|_\infty$ denotes the $\mathcal{L}_\infty(t_0, t_0+T; \mathcal{L}_\infty(\Omega_h))$-norm.

Lastly, consider term R_{10}. Assuming that $\partial_x P$ and $\partial_y P$, which are given data, are both bounded on Ω_h for all $h > 0$ and for all $t \in [t_0, t_0+T]$, then

this term may be bounded by applying equations (3.2.2) and (3.2.3) twice:

$$\begin{aligned}
\int_{t_0}^{t_1^*} |R_{10}| \, dt &= \varrho^{-1} \int_{t_0}^{t_1^*} \left| \sum_E \left\{ \left((\psi_1 - \theta_1) \partial_x P, \psi_2 \right)_E + \left((\psi_1 - \theta_1) \partial_y P, \psi_3 \right)_E \right\} \right| dt \\
&\leq \varrho^{-1} \int_{t_0}^{t_1^*} \sum_E \|\psi_1 - \theta_1\|_{0,E} \\
&\qquad \times \left(\|\partial_x P\|_\infty \|\psi_2\|_{0,E} + \|\partial_y P\|_\infty \|\psi_3\|_{0,E} \right) dt \\
&\leq \varrho^{-1} \Bigg(\frac{\Delta T_1}{2} \|\psi_1(t_{11}, \cdot)\|_{0,h}^2 + \frac{\Delta T_1}{4\epsilon} (1 + 2\epsilon) \|\partial_x P\|_\infty^2 \|\psi_2(t_{12}, \cdot)\|_{0,h}^2 \\
&\qquad + \frac{\Delta T_1}{4\epsilon} (1 + 2\epsilon) \|\partial_y P\|_\infty^2 \|\psi_3(t_{13}, \cdot)\|_{0,h}^2 \\
&\qquad + \epsilon \int_{t_0}^{t_1^*} \sum_E \|\theta_1\|_{0,E}^2 \, dt \Bigg). \qquad (3.2.17)
\end{aligned}$$

To complete step 2 for the first time interval $[t_0, t_1]$, the results in equations (3.2.6)–(3.2.17) are combined, and all terms involving $\|\psi_i(t_{1i}, \cdot)\|_{0,h}^2$ for each value of i, as well as all terms involving various components of $\|\boldsymbol{\Psi}\|_{0,h}^2$, $\left\|\boldsymbol{\sigma}^{1/2} [\![\boldsymbol{\psi}]\!]\right\|_{0,I}^2$, and $\left\|\boldsymbol{\sigma}^{1/2} \boldsymbol{\psi}^{(\text{in})}\right\|_{0,B}^2$, are hidden inside the appropriate terms appearing on the left-hand side of equation (3.2.1). This is accomplished by taking both the parameter ϵ and the time interval length ΔT_1 to be sufficiently small.

Now consider all subsequent time sub-intervals $[t_{m-1}, t_m]$ for $m = 2, 3, \ldots, M$. Equation (3.2.1) becomes

$$\begin{aligned}
&\frac{1}{2} \sum_i K_{ii} \|\psi_i(t_{mi}, \cdot)\|_{0,h}^2 \\
&\qquad + \int_{t_{m-1}}^{t_m^*} \left\{ \|\boldsymbol{\Psi}\|_{0,h}^2 + \sum_I \left\|\boldsymbol{\sigma}^{1/2} [\![\boldsymbol{\psi}]\!]\right\|_{0,I}^2 + \sum_B \left\|\boldsymbol{\sigma}^{1/2} \boldsymbol{\psi}^{(\text{in})}\right\|_{0,B}^2 \right\} dt \\
&\qquad\qquad \leq 4 \int_{t_{m-1}}^{t_m^*} \left| \sum_{n=1}^{10} R_n \right| dt + \frac{1}{2} \sum_i K_{ii} \|\psi_i(t_{m-1,i}, \cdot)\|_{0,h}^2 \qquad (3.2.18)
\end{aligned}$$

since $\|\psi_i(t_{m-1},\cdot)\|_{0,h} \leq \|\psi_i(t_{m-1,i},\cdot)\|_{0,h}$. This term is bounded from the argument on the previous time interval(s). Equations (3.2.2)–(3.2.5) continue to hold, with t_0, t_1^*, ΔT_1, t_{1i}, and t_{1k} replaced by t_{m-1}, t_m^*, ΔT_m, t_{mi}, and t_{mk}, respectively. Repeating the process of bounding terms R_1 through R_{10} gives, for the sub-interval $[t_{m-1}, t_m]$,

$$\begin{aligned}
\int_{t_{m-1}}^{t_m^*} \left| \sum_{n=1}^{10} R_n \right| dt \leq \widehat{\widehat{C}} & \int_{t_{m-1}}^{t_m^*} \sum_E \|\boldsymbol{\theta}\|_{0,E}^2 \, dt \\
& + \frac{C_{\mathrm{tr}}^2}{2\epsilon} \int_{t_{m-1}}^{t_m^*} \sum_E \sum_{i>1} \left\| \sigma_{ii}^{-1/2} \boldsymbol{\Theta}_{\mathbf{F}}|_i \right\|_{0,E} \left\| \sigma_{ii}^{-1/2} \boldsymbol{\Theta}_{\mathbf{F}}|_i \right\|_{1,E} dt \\
& + \epsilon C_{\mathrm{tr}}^2 \int_{t_{m-1}}^{t_m^*} \sum_E \sum_{i=2}^{3} \left\| \sigma_{ii}^{1/2} \theta_i \right\|_{0,E} \left\| \sigma_{ii}^{1/2} \theta_i \right\|_{1,E} dt \\
& + \frac{C_{\mathrm{tr}}^2}{2\epsilon} \int_{t_{m-1}}^{t_m^*} \sum_E \sum_{i} \left\| \sigma_{ii}^{1/2} \theta_i \right\|_{0,E} \left\| \sigma_{ii}^{1/2} \theta_i \right\|_{1,E} \\
& + \frac{C_{\mathrm{tr}}^2}{2\epsilon} \int_{t_{m-1}}^{t_m^*} \sum_E \sum_{i} \left\| \sigma_{ii}^{-1/2} \boldsymbol{\Theta}|_i \right\|_{0,E} \left\| \sigma_{ii}^{-1/2} \boldsymbol{\Theta}|_i \right\|_{1,E} \\
& + \frac{1}{4\epsilon} |\mathsf{D}|_\infty^2 \, C_{\mathrm{tr}}^4 C_{\mathrm{inv}} \int_{t_{m-1}}^{t_m^*} \sum_E \sum_i h^{-1} \|\theta_i\|_{0,E} \|\theta_i\|_{1,E} \, dt \\
& + \check{C} \int_{t_{m-1}}^{t_m^*} \sum_E \|\theta_1\|_{0,E}^2 \, dt \\
& + \epsilon g \|H_{hp}\|_\infty \int_{t_{m-1}}^{t_m^*} \sum_E \left\{ \tilde{\nu}_x^{-1} \|\Theta_{41}\|_{0,E}^2 + \tilde{\nu}_y^{-1} \|\Theta_{42}\|_{0,E}^2 \right\} dt,
\end{aligned} \tag{3.2.19}$$

where

$$\check{C} = \epsilon \Big(g \left(\tilde{\nu}_x^{-1} \|Z_{41}\|_\infty + \tilde{\nu}_y^{-1} \|Z_{42}\|_\infty \right) + \varrho^{-1} \Big).$$

To bound the right-hand side in terms of the exact solution and flux, Theorem 3.2.3 is applied with $r = p + 1$ to the first, third, fourth, sixth, and seventh terms. For the second, fifth, and eighth terms, Theorem 3.2.3 is ap-

plied with $r = p$, and the facts that

$$\begin{aligned}
\|Z_{41}\|_{p,E} &\leq \tilde{\nu}_x \|b\|_{p+1,E}\,, \\
\|Z_{42}\|_{p,E} &\leq \tilde{\nu}_y \|b\|_{p+1,E}\,, \\
\sum_{i>1} \|\mathbf{Z}|_i\|_{p,E}^2 &\leq \max\{\nu_x^2 + \nu_y^2, \tilde{\nu}_x^2 + \tilde{\nu}_y^2\} \|\mathbf{w}\|_{p+1,E}^2\,,
\end{aligned}$$

are used when bounding the fifth and eighth terms. This completes step 2.

To accomplish step 3, one must bound the maximum over all time subintervals of the first term on the left-hand side of equation (3.2.18), dropping the remaining terms. The right-hand side of equation (3.2.18) is bounded by $4\int_{t_0}^{t_0+T} |\sum_n R_n|\, dt$ by a recursive argument on m. Thus, after some tedious manipulation, one arrives at the result:

Theorem 3.2.4 (*A priori* error estimate)**.** *Assume that:*

1. *The bed porosity matrix* $\mathbf{K}$ *is constant,*
2. *The diffusion tensor* D *is constant,*
3. *The bottom friction coefficient* τ_{bf} *is constant,*
4. *Each component of* $\mathbf{q}$ *and* $\mathbf{q}_{hp}$*, the square of each component of* $\mathbf{q}$*, and also* Z_{41}*,* Z_{42}*,* $\partial_x P$*, and* $\partial_y P$ *are uniformly bounded from above (in space and time) for all partitions of* Ω_h*, and*
5. H *and* H_{hp} *are uniformly bounded from above and below (in space and time) for all partitions of* Ω_h*.*

Then:

1. *Each component of the inviscid flux* $\mathbf{F}$ *is Lipschitz-continuous in* $\mathbf{w}$*, and*

2. *For a sufficiently smooth solution* $\mathbf{w}$*, the semidiscrete formulation* (2.2.6) *of the initial-boundary value problem* (2.1.4) *satisfies*

$$\max_m \frac{1}{2} \sum_i K_{ii} \left\| \psi_i(t_{mi}, \cdot) \right\|_{0,h}^2 \leq \int_{t_0}^{t_0+T} h^{2p} \Big\{ \left(C + C^* h + C^{**} h^2 \right) \left\| \mathbf{w} \right\|_{p+1,h}^2 + C \left\| \mathbf{F} \right\|_{p,h}^2 + C^* h \left\| \sigma_{11}^{1/2} H \right\|_{p+1,h}^2 \Big\} \, dt, \quad (3.2.20)$$

where C*,* C^**, and* C^{**} *are constants that are independent of* h*.*

The bounding constants in equation (3.2.20) are given by

$$\begin{aligned} C &= 4K^2 \bigg(\epsilon C_{\mathrm{tr}}^2 + \frac{C_{\mathrm{tr}}^2}{2\epsilon} \Big(1 + \max\big\{ \nu_x^2 + \nu_y^2, \tilde{\nu}_x^2 + \tilde{\nu}_y^2 \big\} \Big) \\ &\qquad + \frac{1}{4\epsilon} \left| \mathsf{D} \right|_\infty C_{\mathrm{tr}}^4 C_{\mathrm{inv}} + \epsilon g \| H \|_\infty (\tilde{\nu}_x + \tilde{\nu}_y) \bigg), \\ C^* &= \frac{3K^2 C_{\mathrm{tr}}^2}{\epsilon}, \\ C^{**} &= 4K^2 \bigg(\frac{C_L^2}{4\epsilon} \Big(2 \left(\nu_x^{-2} + \nu_y^{-2} \right) + \tilde{\nu}_x^{-2} + \tilde{\nu}_y^{-2} \Big) + 6\epsilon C_L^2 C_{\mathrm{tr}}^2 C_{\mathrm{inv}} + \check{C}. \end{aligned}$$

3.3 Discussion and Remarks

In this preceding two sections, an *a priori* error estimate for the LDG method applied to the morphodynamics problem—that is, for the full nonlinear coupled SWE–Exner system—has been formulated, analyzed, and developed. The estimate obtained here is similar in form to that derived in [1], except that this result requires one fewer degree of regularity for the solution $\mathbf{w}$ and inviscid flux $\mathbf{F}$, and contains additional terms arising from the nonlinear components of $\mathbf{F}$, sedimentary diffusion, and penalty terms. The resulting

bounding constants are not exponentially dependent; Grönwall's lemma is neither applied nor needed.

An attempt has been made to explicitly track the bounding constants, in hopes of enhancing the usefulness of the result as a verification tool for LDG morphodynamic solvers. For a simple mesh with a known (or manufactured) solution, where enough parameters can be explicitly computed, this may serve as a simple check for solver correctness and, perhaps more importantly, h-convergence behavior. The h-convergence rate is seen in equation (3.2.20) to be p, as expected, although not optimal. More rapid convergence rates may be realized for problems with simple meshes and very smooth initial and boundary data.

The reader is cautioned that the estimate obtained herein applies only under the numerous assumptions regarding the smoothness of the coefficients stated above, as well as a rather simplistic choice of (pure Dirichlet) boundary conditions. In practice, most, if not all, of these coefficients, such as $\mathbf{K}$, D, and τ_{bf}, are spatially (and possibly temporally) dependent, and may exhibit nonlinear dependence on the solution. Also, many finite element domains used in numerical shallow water and/or morphodynamic solvers (such as the Advanced Circulation Model ADCIRC) possess many types of boundaries, such as those described in Section 2.5.1, each applying on distinct boundary segments, and none of which are pure Dirichlet for all components of $\mathbf{w}$. This, of course, affects the form of equation (3.1.11); the boundary term reappears. Treatment of variable material data, as well as more complex boundary data, will be addressed in future research.

Chapter 4

Numerical Examples and Results

In this chapter, numerical examples and results using the model implementation described in Chapter 2 are presented. The LDG method is applied to five problems: an evolving dune, a converging channel, a bridge pier, an idealized inlet, and a dry area protected by barriers. These cases are described and analyzed in Sections 4.1–4.5. These simulations were run in parallel (with the exception of the first and fifth test cases) on the Institute for Computational Engineering and Science's (ICES) `bevo2` cluster, as well as on the Texas Advanced Computing Center's `lonestar` (III) [174] cluster[1].

As a reminder to the reader, $\mathsf{D} = 0$ in all test cases described in this chapter. As such, the alternative DG formulation given by (2.4.6) is used. In addition, the split formulation of the numerical flux is used in Sections 4.1 through 4.4, while the NCP numerical flux described in Section 2.4.3 is used in Section 4.5.

It should be noted that the results and descriptions presented in Sections 4.1–4.4 and 4.6 appear in earlier work by the author [132]. Minor changes and clarifications appear in this work.

[1]The architecture of the `lonestar` (III) cluster has been upgraded since these test cases were run, and the machine relaunched in February 2011 as `lonestar` (IV) [175]. The effect on the results in Section 4.6 has yet to be tested.

4.1 Convergence Study: Evolution of a Dune

For this test case, a problem posed by Exner [70] in 1925 was examined. The problem considered the evolution of an initially symmetric mound, or dune, which was subjected to steady, unidirectional flow under the assumption of a rigid lid (meaning ζ was assumed constant in space and time). Solving this problem permitted the sediment transport model to be tested independently of the hydrodynamics. This was accomplished by comparing the numerical solution to a classical one derived in [70] for the purpose of verifying h- and p-convergence rates. A secondary benefit is the verification and expansion upon the results presented in [101] for second- and third-order RKDG schemes.

To properly compare the numerical solution to the exact solution, a simpler model was employed. Exner's model uncoupled the sediment transport equation from the SWE by setting $\zeta = 0$, which implies that $H = b$, and a constant, unidirectional discharge rate per unit width $\mathbf{q} = (q_f, 0)^\top$ where $q_f > 0$. Also, it was assumed that $\tilde{\mathbf{q}} = (Aq_f/b, 0)^\top$, where A is a nonnegative constant. When the porosity is zero ($\kappa = 1$), the diffusion is zero ($\mathsf{D} = 0$), and $\mathbf{s} = 0$, it is straightforward to show that the SWE degenerate, and thus equation (2.1.1) reduces to

$$\partial_t(-b) + \partial_x(Aq_f/b) = 0. \tag{4.1.1}$$

Let $b(0, \mathbf{x}) = b_0(x)$ be the initial data, which is assumed to be sufficiently smooth. Then the exact solution derived in [70] is given implicitly by

$$b(t, \mathbf{x}) = b_0(x - ct), \tag{4.1.2a}$$

$$c(b) = Aq_f/b^2, \tag{4.1.2b}$$

where c denotes the speed at which the top of the dune propagates. This is the same as the characteristic speed.

For this problem, the square domain $\Omega = (-\lambda/2, \lambda/2)^2$ is considered, and the initial data is given by

$$b_0(x) = A_0 + A_1 \cos\left(\frac{2\pi x}{\lambda}\right),$$

with $A_0 = 2$, $A_1 = -1$, and $\lambda = 20$. The boundary conditions are shown in Table 4.1. The solution is assumed periodic in the x-direction over Ω, and a land BC is imposed at $y = \pm\lambda/2$. Finally, it is assumed that $Aq_f = 1$ in equation (4.1.2b).

Boundary	BC type
$\{(\pm\lambda/2, y) : y \in (-\lambda/2, \lambda/2)\}$	Periodic
$\{(x, \pm\lambda/2) : x \in (-\lambda/2, \lambda/2)\}$	Land

Table 4.1: Boundary conditions for the dune test case

Nonlinear hyperbolic conservation laws have the well-known property that solutions typically develop very steep gradients and eventually discontinuities or shocks. This behavior can be seen in this problem when performing a characteristic analysis. Equation (4.1.1) may be written as

$$\partial_t(-b) + \partial_x f = 0,$$

with $f = Aq_f/b$, and carrying out the partial derivatives gives the nonconservative form

$$\partial_t(-b) + c\big(b(x)\big)\partial_x b = 0,$$

where $c\big(b(x)\big) = \partial f/\partial b$. Then it can be seen that the breaking time when the shock (or sediment bore) forms is given by

$$t_b = -\left[\min_{\xi} \frac{d}{d\xi} c\big(b_0(\xi)\big)\right]^{-1} = \frac{5(5-\sqrt{7})^3}{4\pi\sqrt{2\sqrt{7}-4}} \approx 4.5685\,\text{s}.$$

In this study, four meshes denoted h_1 through h_4 are considered. The coarsest mesh h_1 consists of 800 elements, arranged according to Figure 4.1(a). The value of h, defined here as the length of an element in the x-direction, is 1 m. Mesh h_2 is a 1:4 refinement of h_1, with $h = 1/2$ m and 3200 elements (see Figure 4.1(b)). This process is repeated to generate meshes h_3 and h_4.

The numerical model is then run until the breaking time t_b is reached. The time step size is set small enough so that the spatial errors dominate the overall error. The DG solution b_h is computed using piecewise constant, linear, quadratic, and cubic basis functions ($p = 0$, 1, 2, and 3) with the SSP(1,1), SSP(2,2), SSP(3,3), and SSP(5,4) time stepping schemes, respectively, and the errors are computed by comparing the approximate solution b_h to the exact solution given by equations (4.1.2a) and (4.1.2b). The h-convergence results using the $\mathcal{L}_\infty(\Omega_h)$-norm at $t = 2$ s and $t = 4$ s are shown in Figures 4.2(a) and 4.3(a), respectively, while the p-convergence results using mesh h_4 and the $\mathcal{L}_\infty(\Omega_h)$-norm at $t = 2$ s and $t = 4$ s are shown in Figures 4.2(b) and 4.3(b), respectively.

At $t = 2$ s, the solution is still smooth, as this time is well before the time of formation of the shock. Thus, the theoretical h-convergence rate of $p + 1$ is very nearly attained, as can clearly be seen in Figure 4.2(a) for the $\mathcal{L}_\infty(\Omega_h)$-norm. It should be noted that these rates are also attained for the $\mathcal{L}_1(\Omega_h)$- and $\mathcal{L}_2(\Omega_h)$-norms, though these results are not shown here. For p-convergence, the theoretical exponential rate is attained, and this is shown in Figure 4.2(b).

However, for $t = 4$ s, which is much closer to the breaking time t_b, the h-convergence rates are either seriously degraded (for the cases of $p = 0$, 2, and 3) or obliterated (for the case $p = 1$) when the error over the entire

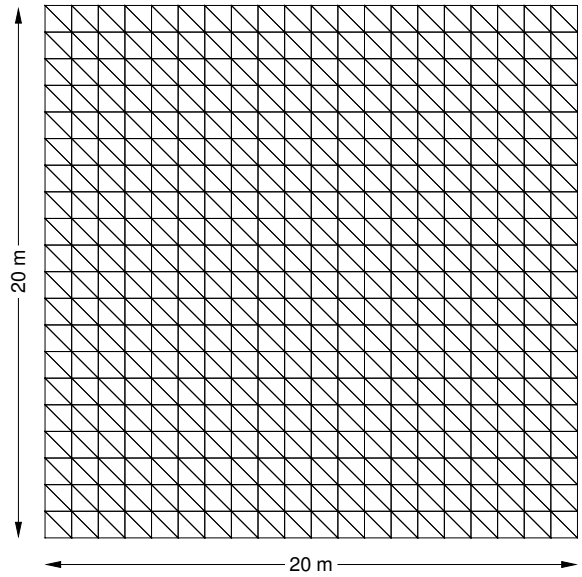

(a) Mesh h_1

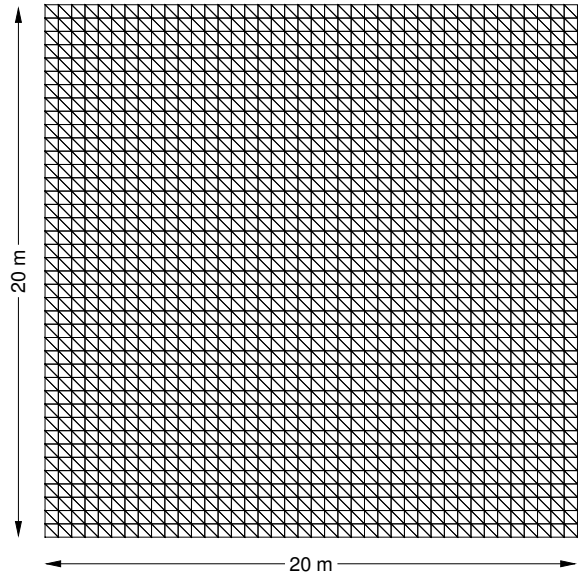

(b) Mesh h_2

Figure 4.1: Computational meshes (a) h_1 and (b) h_2

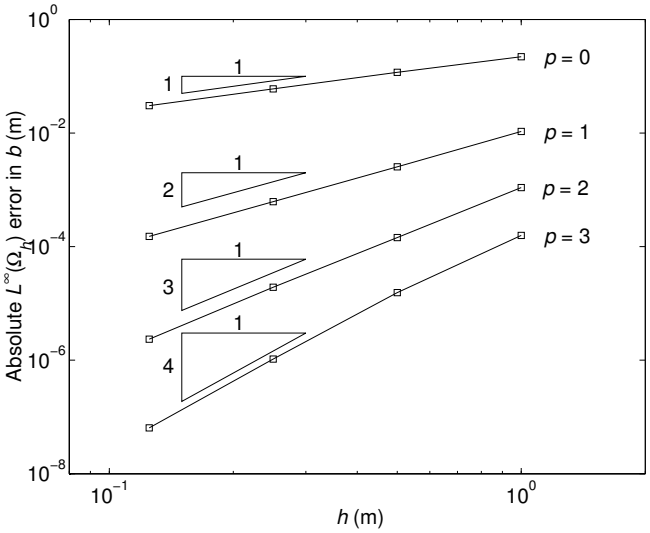

(a) Convergence rates in h

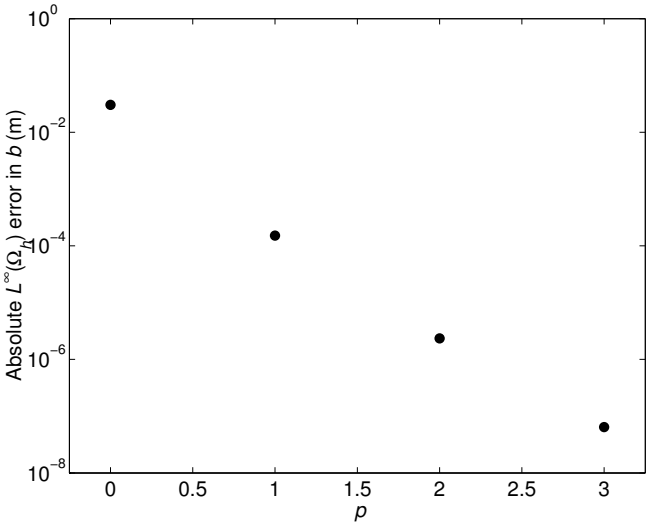

(b) Convergence rates in p

Figure 4.2: $\mathcal{L}_\infty(\Omega_h)$ convergence rates at $t = 2\,\mathrm{s}$

domain Ω_h is under consideration. This is shown in Figure 4.3(a) for the $\mathcal{L}_\infty(\Omega_h)$-norm, and similar results were obtained for the $\mathcal{L}_1(\Omega_h)$- and $\mathcal{L}_2(\Omega_h)$-norms. In this case, the largest portion of the error has accumulated within the narrow region $\{(x, y) : x \in (4, 6), y \in (-10, 10)\}$, which corresponds to the region containing the steepest gradients in the solution, and is also the region containing the shock when $t \geq t_b$. This issue demonstrates the need for further h-refinement in this region, as the results shown in Figure 4.3(a) appear to display pre-asymptotic behavior. However, when accuracy is considered only in the smooth region of the solution, taken here as

$$\Omega_{\text{sm}} = \{(x, y) : x \in (-10, 4), y \in (-10, 10)\},$$

it can be seen in Table 4.2 that nearly full order of convergence is restored for the cases of $p = 0$ and $p = 1$, while the convergence rates for the cases of $p = 2$ and $p = 3$, though not quite optimal, are much improved, and appear to be tending towards the theoretical rates pending further h-refinement. This verifies that the first- through fourth-order RKDG methods maintain their accuracy and theoretical order of convergence away from the region containing steep gradients and shocks.

In Figure 4.3(b), it is seen that the p-convergence rate at $t = 4\,\text{s}$ does not appear to seriously degrade until $p = 3$. Since the results on mesh h_4 were used here, the effects of the value of h being in the pre-asymptotic regime are mitigated; indeed, the convergence rate is further degraded when using mesh h_3, and no convergence is observed when using meshes h_1 or h_2 (not shown here). Despite these shortcomings, however, these results show that the model maintains its accuracy in p when h is small enough.

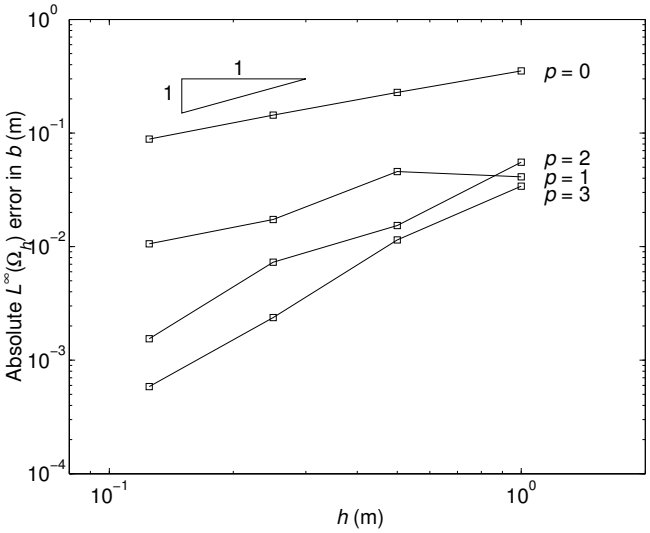

(a) Convergence rates in h

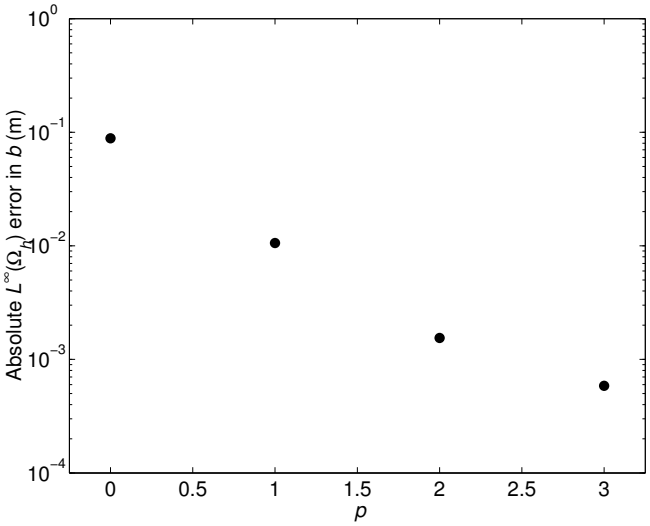

(b) Convergence rates in p

Figure 4.3: $\mathcal{L}_\infty(\Omega_h)$ convergence rates at $t = 4\,\mathrm{s}$

p	Mesh	$\mathcal{L}_\infty$ convergence rates	
		in Ω_h	in Ω_{sm}
0	h_1	$\cdots$	$\cdots$
	h_2	0.6305	0.9762
	h_3	0.6641	0.9892
	h_4	0.7001	0.9967
1	h_1	$\cdots$	$\cdots$
	h_2	-0.1522	1.8339
	h_3	1.4000	1.7602
	h_4	0.7128	1.8740
2	h_1	$\cdots$	$\cdots$
	h_2	1.8513	1.8512
	h_3	1.0743	2.3752
	h_4	2.2383	2.6923
3	h_1	$\cdots$	$\cdots$
	h_2	1.5706	3.4398
	h_3	2.2724	3.1037
	h_4	2.0180	3.5808

Table 4.2: Comparison of h-convergence rates at $t = 4\,\text{s}$

4.2 A Converging Channel

In [70], Exner extended the model presented for the previous test case to account for channels of varying width with vertical walls. He considered a converging or bottleneck channel with an initially flat bed. This is the computational domain considered in this test case, and it is shown in Figure 4.4. The channel considered is 2 km long, 500 m wide at the eastern and western ends, and narrows to 250 m wide at the center.

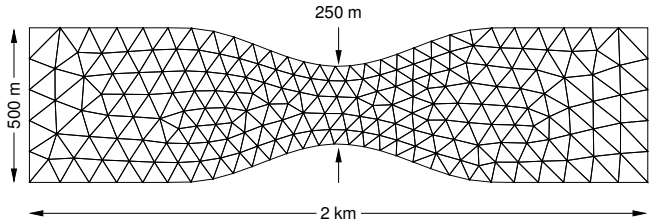

(a) Coarse-scale mesh, containing 378 elements

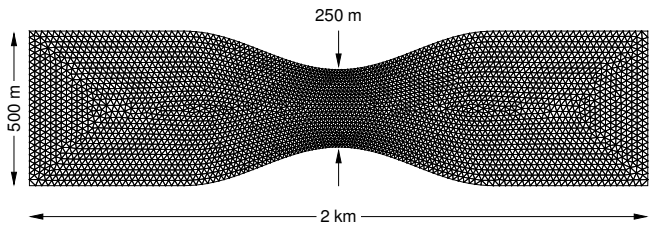

(b) Fine-scale mesh, containing 6804 elements

Figure 4.4: Unstructured computational meshes used in the channel test case. The ratio $h_{\text{coarse}}/h_{\text{fine}} \approx 4.88$, where h_{coarse} and h_{fine} are defined here as the longest edge lengths in the coarse and fine grids, respectively.

Rather than considering the evolution of the bed in a one-dimensional setting, as Exner did, the full morphological system is utilized to consider it in a two-dimensional setting. This allows simultaneously examining both the evolution of the bed and changes in the velocity and flow rate patterns over a 90-day period. For this case, a land BC is imposed for the northern and

southern channel walls, while a fixed inflow rate of $5\,\mathrm{m}^2/\mathrm{s}$ is imposed at the western end of the channel. This rate was chosen so that the flow speed is $0.5\,\mathrm{m/s}$ at either end of the channel, with a maximum speed of approximately $1\,\mathrm{m/s}$ in the throat of the channel. At the eastern boundary, the elevation is held fixed at $\zeta = 0$, chosen to enforce mass conservation. A summary of the BCs is shown in Table 4.3. The bed is initially flat, with a bathymetric depth of $10\,\mathrm{m}$. The bottom is also non-porous ($\kappa = 1$), and the sediment density is taken as $\varrho_s = 2000\,\mathrm{kg/m}^3$, while the median grain size is $d_{50} = 0.0002\,\mathrm{m}$. Nonlinear bottom friction given by $\tau_{\mathrm{bf}} = c_f \left|\mathbf{q}\right| / H^2$ is considered, where $c_f = 0.0025$ is the (dimensionless) friction or bed roughness coefficient.

Boundary	BC Type	Data
North & South walls	Land	
West	Flow	$\mathbf{q}_D = 0.5\,\mathrm{m}^2/\mathrm{s}$
East	Open	$\zeta_D = 0\,\mathrm{m}$

Table 4.3: Boundary conditions for the converging channel test case

For purposes of comparison, this test case is run using two different grids. The first is a coarse mesh, shown in Figure 4.4(a), and the second is a finer-scale mesh, shown in Figure 4.4(b). For each of these grids, numerical realizations of $\mathbf{w}_{hp}$ using piecewise constant, linear, and quadratic basis functions are considered. For the case of piecewise constant basis functions, time step sizes of $1.5\,\mathrm{s}$ (coarse grid) and $0.25\,\mathrm{s}$ (fine grid) are used with the forward Euler scheme SSP(1,1); for piecewise linear basis functions, $0.75\,\mathrm{s}$ and $0.1\,\mathrm{s}$, respectively, with SSP(2,2); for piecewise quadratics, $0.5\,\mathrm{s}$ and $0.1\,\mathrm{s}$, respectively, with SSP(3,3). Recall from Section 2.5 that a higher-order slope limiter described in [193] is applied when $p = 2$, which allows for taking slightly larger time step sizes than usual, though still well below the theoretical threshold

given by the CFL condition. For example, using the estimate for the CFL restriction given by

$$\Delta t \leq \min_{\Omega_E} \left(\frac{h_E}{\max_i |\lambda_{i,E}|} \frac{1}{2p+1} \right), \tag{4.2.1}$$

where $1/(2p+1)$ is an estimate of the CFL number [101], one finds that $\Delta t_{\text{CFL}} \approx 0.85\,\text{s}$ for the coarse grid and $\Delta t_{\text{CFL}} \approx 0.15\,\text{s}$ for the fine grid. In practice, however, time step sizes of approximately $\Delta t_{\text{CFL}}/2$ must be taken before the model becomes stable when the operator $(\Lambda\Pi) = I$; the ability to take time step sizes larger than $\Delta t_{\text{CFL}}/2$ is thus a welcomed feature of this slope limiter.

Plots of the bathymetry for $p = 0$, 1, and 2 on the coarse mesh at $t = 90\,\text{days}$ are shown in Figure 4.5, while Figure 4.6 shows the corresponding velocity magnitude. In Figure 4.5, it can be seen that the bottom undergoes erosion in the converging part of the channel because the flow is accelerating there (shown in Figure 4.6). Conversely, sediment accretion can be seen in the diverging part of the channel since the flow speed is decreasing there. The erosion and accretion patterns are not uniform across the width of the channel, however, as it can be observed in Figure 4.6 that the velocity is nonuniform across the channel width; it is slightly higher near the center. Since the sediment discharge rate $\tilde{\mathbf{q}}$ is a function of $|\mathbf{q}|^3$, the magnitude of the erosion and accretion is seen to vary considerably across the channel width.

The numerical solution exhibits qualitatively similar behavior on the fine-scale mesh, except with generally better resolution. Consider the bathymetric profiles shown in Figures 4.5 and 4.7. For the piecewise constant case, notice that the fine-scale solution reflects higher sediment mass transport rates. For the cases of $p = 1$ and $p = 2$, differences in resolution are more pronounced:

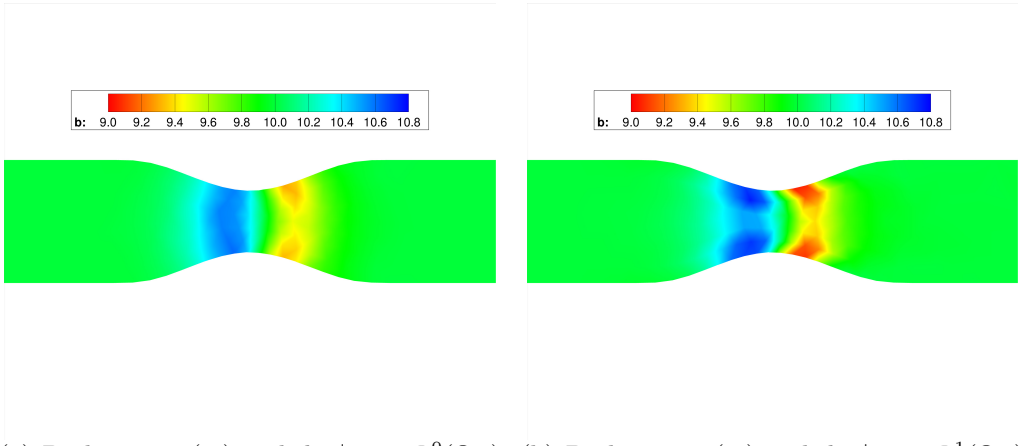

(a) Bathymetry (m) with $b_{hp}|_{\Omega_E} \in \mathcal{P}^0(\Omega_E)$ (b) Bathymetry (m) with $b_{hp}|_{\Omega_E} \in \mathcal{P}^1(\Omega_E)$

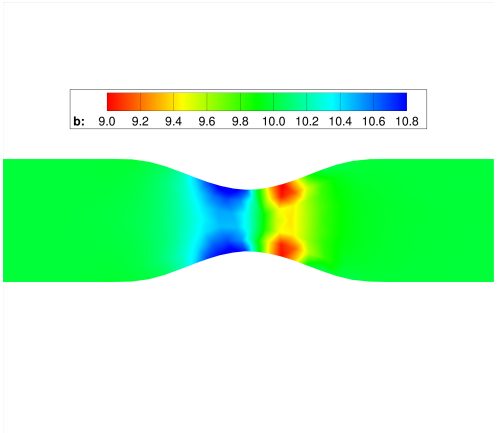

(c) Bathymetry (m) with $b_{hp}|_{\Omega_E} \in \mathcal{P}^2(\Omega_E)$

Figure 4.5: Bathymetry (m) after 90 days on the coarse mesh

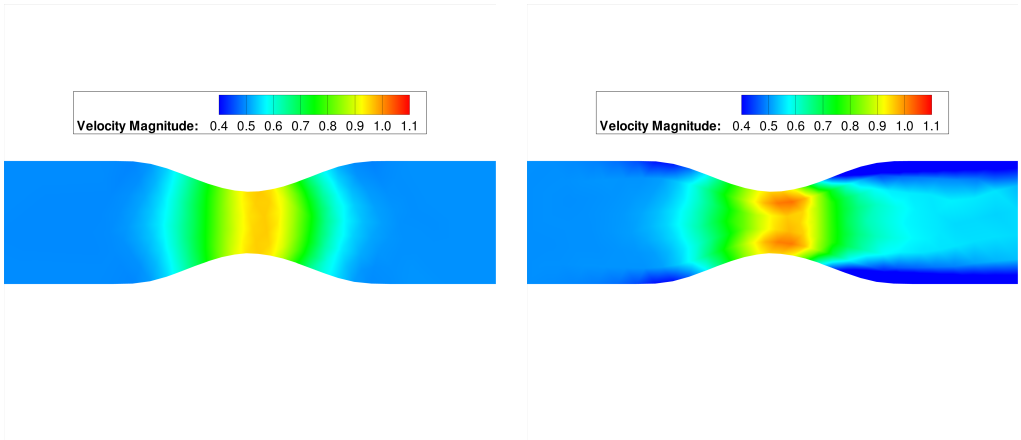

(a) Flow speed (m/s) with $p = 0$

(b) Flow speed (m/s) with $p = 1$

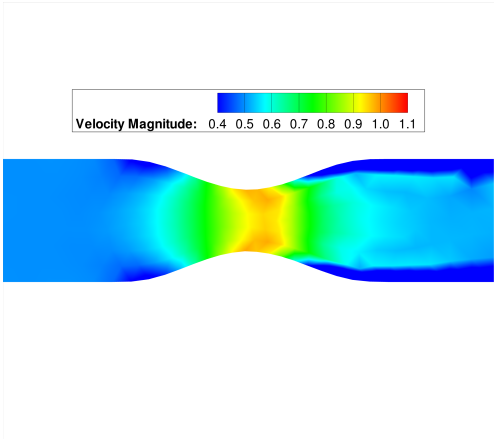

(c) Flow speed (m/s) with $p = 2$

Figure 4.6: Flow speed (m/s) after 90 days on the coarse mesh

the solution on the fine mesh appears to better account for the land boundaries, and the resolution in the transition regions (on the upstream edge of the scouring region, between the erosion and deposition zones, and just downstream of the deposition region) is much sharper. The piecewise quadratic solution on the fine mesh (Figure 4.5(c)) more sharply captures the transport behavior in the center of the channel; the cross-stream profile is not as well resolved on the coarse mesh, especially in the accretion zone.

Now consider the velocity profiles shown in Figures 4.6 and 4.8. For the case of $p = 0$, the fine-scale solution shows a slightly larger speed gradient, especially near the boundaries, explaining the differences in b_{hp} between Figures 4.5(a) and 4.7(a) as a result of the differing transport rates. For the cases of $p = 1$ and $p = 2$, one immediately spots the differences in the flow behavior near the land boundaries in the channel throat when comparing them with the piecewise constant results. The increase in velocity from the channel center to the boundary region is more well defined; this feature appears to be smeared in Figures 4.6(b) and 4.6(c). The highest speeds occur nearer to the boundaries in the throat, and the velocity gradient downstream of the throat is much higher compared to the coarse-grid solution.

When $p \geq 1$, a long, thin boundary layer is seen downstream of the channel throat. Its appearance is consistent with the results shown in [172], and may be partly due to the effect of the land BC there (recall from Section 2.5.1 that free tangential slip is specified there). However, it is noted that by comparing Figures 4.6(b) and 4.8(b), its thickness appears to depend on the grid size: as $h \downarrow 0$, this layer becomes thinner, and appears to be confined only to those elements next to the land boundary.

Comparing the DG solutions for b and $|\mathbf{u}|$ across the different values

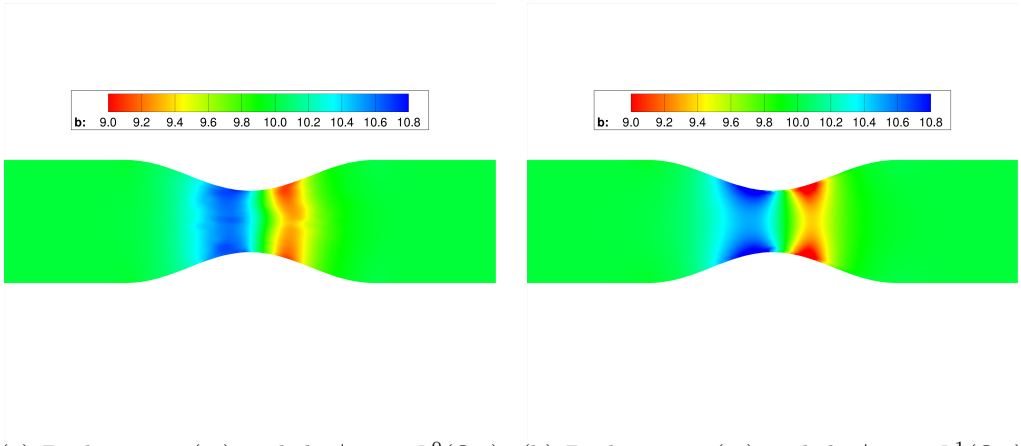

(a) Bathymetry (m) with $b_{hp}|_{\Omega_E} \in \mathcal{P}^0(\Omega_E)$ (b) Bathymetry (m) with $b_{hp}|_{\Omega_E} \in \mathcal{P}^1(\Omega_E)$

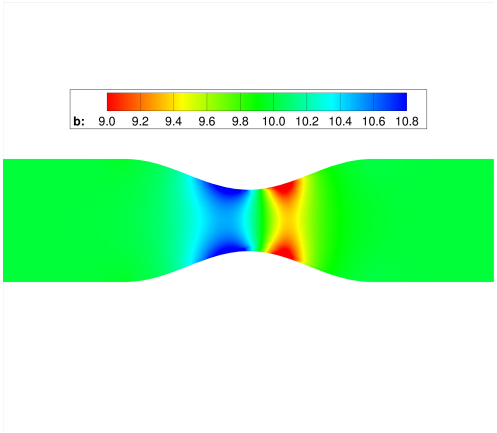

(c) Bathymetry (m) with $b_{hp}|_{\Omega_E} \in \mathcal{P}^2(\Omega_E)$

Figure 4.7: Bathymetry (m) after 90 days on the fine mesh

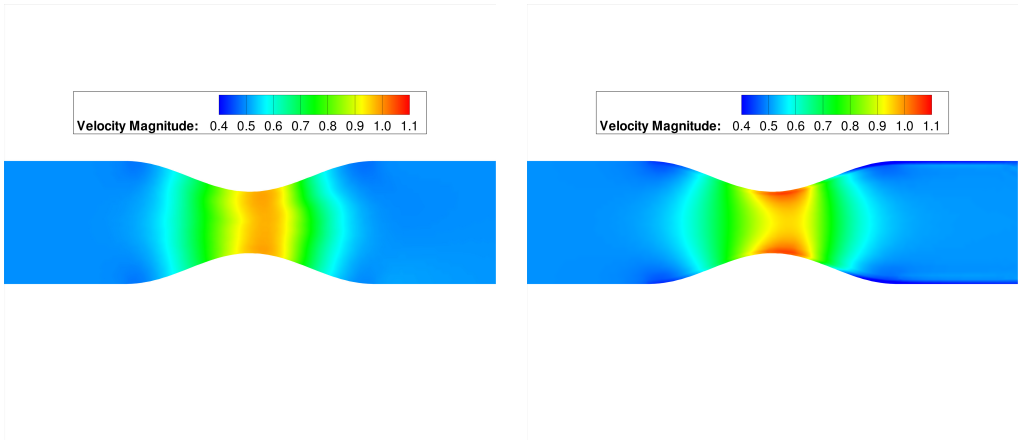

(a) Flow speed (m/s) with $p = 0$

(b) Flow speed (m/s) with $p = 1$

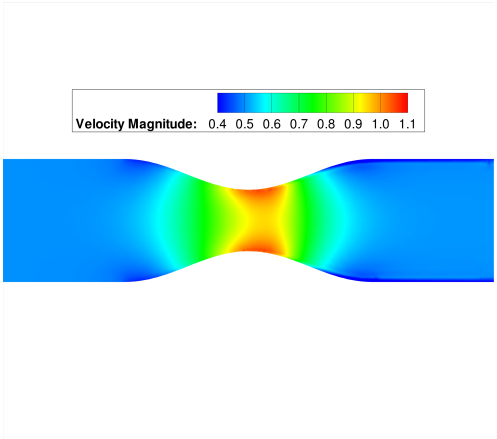

(c) Flow speed (m/s) with $p = 2$

Figure 4.8: Flow speed (m/s) after 90 days on the fine mesh

of p, it is immediately noticed that the $p = 0$ approximation of b only superficially captures the scouring and accretion behavior; the computed sediment transport rate in the converging region appears too high, while it is too low along the land boundaries. Thus, some numerical diffusion is evident here; the $p = 0$ approximation of b appears to be overly diffusive. Increasing p dramatically improves the resolution of b_{hp}, especially near the boundaries, in particular for $p = 2$, where the solution appears to sharply resolve the subgrid-scale features in the transition region. Figures 4.5(c) and 4.7(c) show that the higher-order slope limiter suppresses oscillations near the land boundaries in the throat of the channel when $p = 2$. Considering $|\mathbf{u}|$ now, a similar problem of resolution when $p = 0$ is observed: the cross-stream velocity profile appears to be nearly uniform in the throat of the channel, and the model fails to capture the behavior of the solution near the land boundaries in the channel throat; the predicted speed still appears to be too low.

Based on the issues pointed out thus far, it should be noted that the coarse-grid solutions do not seem to be satisfactory for any value of $p \in \{0, 1, 2\}$ when compared with some results shown in the literature [106, 172]. Results obtained using the fine-scale grid are still not well resolved when $p = 0$, but are generally very well resolved when $p \geq 1$. These observations, especially the final one, underscore the need for taking p of sufficient order in the DG approximations.

It is important to observe the interaction between the bathymetric and velocity profiles as both evolve in time: as the bed is eroding in the converging part of the channel, the total depth H increases, which in turn acts to decrease $|\mathbf{u}|$. Conversely, as a mound begins to form on the bed in the diverging part of the channel, H decreases, causing an increase in $|\mathbf{u}|$ in this region. This

ongoing (coupled) process results in the entire velocity profile slowly shifting slightly downstream with time. These results are shown in Figures 4.9 and 4.10 for $p = 2$.

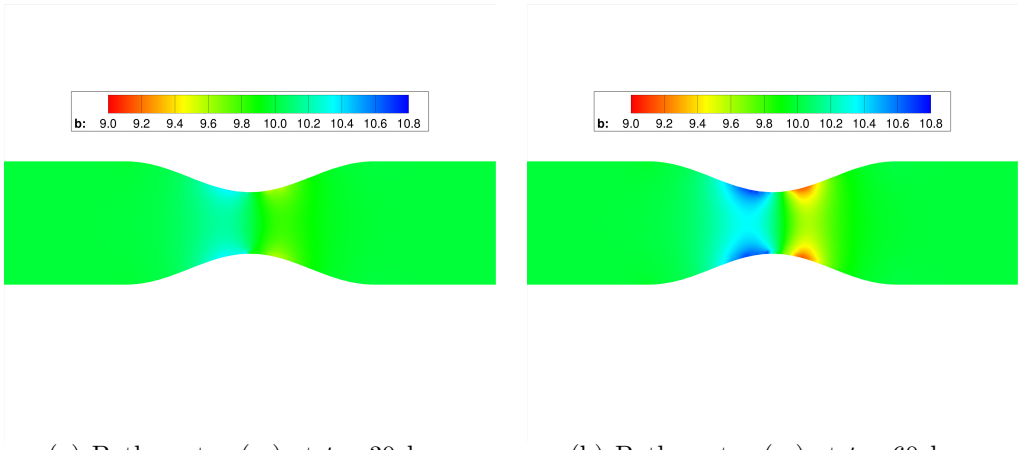

(a) Bathymetry (m) at $t = 30$ days

(b) Bathymetry (m) at $t = 60$ days

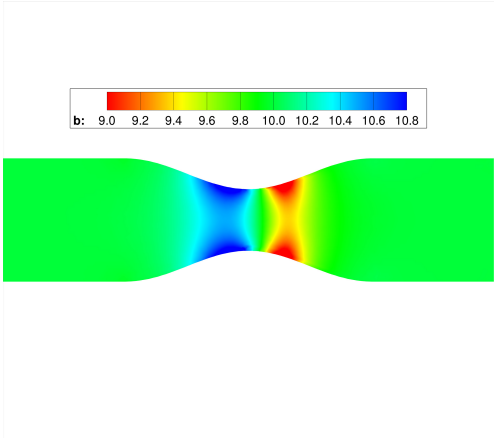

(c) Bathymetry (m) at $t = 90$ days

Figure 4.9: Bathymetry (m) at 30-day intervals on the fine mesh

Lastly, it should be noted that the results shown in Figures 4.5–4.8 all compare well qualitatively with an analytical solution derived by Exner in [70] for a problem with similar geometry, with results shown in Tassi *et al.* [172]

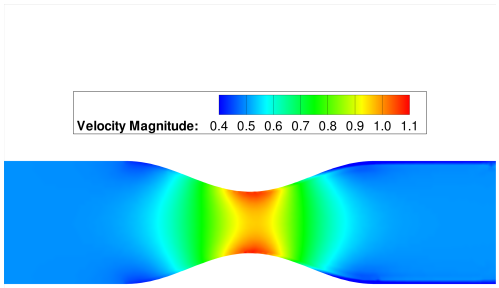

(a) Flow speed (m/s) at $t = 30$ days

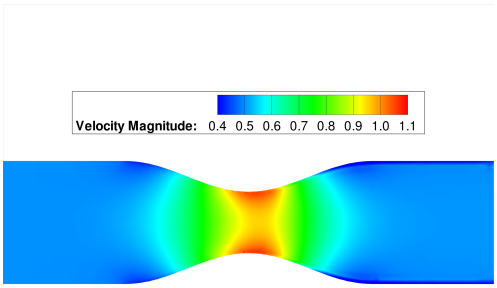

(b) Flow speed (m/s) at $t = 60$ days

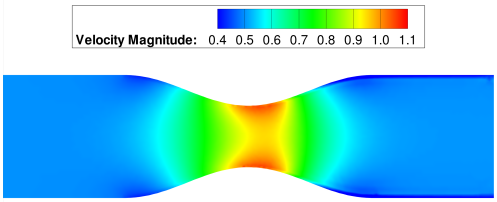

(c) Flow speed (m/s) at $t = 90$ days

Figure 4.10: Flow speed (m/s) at 30-day intervals on the fine mesh

for this problem posed in a non-dimensional setting, and with the computed results presented in Kubatko *et al.* [106] using a combined CG/DG model (for $p = 1$).

4.3 Scouring around a Bridge Pier

In this section, another well-known and well-studied problem in coastal engineering is examined: scouring, or bed erosion, around a vertical, cylindrical bridge pier, such as those commonly seen on roadway and railway bridges across rivers and estuaries. Applications of these problems to coastal engineering activities motivate this study, as scouring has been cited as one of the most common causes of bridge failures in these regions [87, 122, 123]. It is also wished to verify that the model accurately depicts the major flow features associated with the scouring process, at least in a qualitative sense. This problem would be more accurately simulated by a three-dimensional Navier–Stokes model, but an interesting question is to determine which features can be captured by a hydrostatic, depth-averaged model.

In this problem, an initially flat bed is subjected to a uniform, unidirectional flow originating from the western (upstream) boundary. This free stream or upstream velocity is denoted as $\mathbf{u}_\infty = (u_\infty, 0)^\top$. The domain under study in this test case is a square of side length 30 m with a circular island of diameter $D = 2$ m positioned at the origin. However, since the true solution $\mathbf{w}$ is symmetric about the x-axis, the domain is chosen as

$$\Omega = \{(x, y) \in \mathbb{R}^2 : x \in (-15, 15), y \in (0, 15), x^2 + y^2 > 1\}$$

in order to save computational time. Two computational meshes shall be used for this test case for comparison. These are shown in Figure 4.11. The fine-

scale mesh (Figure (b)) is a uniform 1:4 refinement of the coarse-scale mesh (Figure (a)). The bed is initially flat with a depth of 1 m. Boundary conditions are similar to those for the previous test case, and are shown in Table 4.4. That is, at $x = -15$, a flow BC is specified. At the bridge pile boundary, a land BC is imposed. A land BC is also imposed at the top ($y = 15$) and along the axis of symmetry ($y = 0$). At $x = 15$, zero free surface elevation is specified.

Boundary	BC type	Data
$\{(-15, y) : y \in (0, 15)\}$	Flow	$\mathbf{q}_D \cdot \mathbf{n} = 0.2\,\mathrm{m}^2/\mathrm{s}$
$\{(x, 0) : x \in (-15, -1) \cup (1, 15)\}$	Land	
$\{(x, \sqrt{1 - x^2}) : x \in [-1, 1]\}$	Land	
$\{(x, 15) : x \in (-15, 15)\}$	Land	
$\{(15, y) : y \in (0, 15)\}$	Open	$\zeta_D = 0\,\mathrm{m}$

Table 4.4: Boundary conditions for the pile test case

Values for κ, ϱ_s, d_{50}, and c_f were the same as for the test case in Section 4.2. However, in order to save computational time, the sediment transport rates were artificially inflated by a factor of 1000 so that the bed evolution may be examined after 1 day, well after the flow becomes fully developed.

Following the pattern begun with the previous test cases, the value of $\mathbf{w}_{hp}$ for $p = 0$, 1, and 2 for both meshes is desired. When $p = 0$, the time step sizes are set to 0.025 s (coarse mesh) and 0.01 s (fine mesh) and SSP(1,1) is employed; $p = 1$, 0.01 s and 0.005 s, respectively, with SSP(2,2); $p = 2$, 0.0075 s and 0.0025 s, respectively, with SSP(3,3). Recall from Section 2.5 that slope limiter 1 is applied to all components of $\mathbf{w}_{hp}$ in order to control and/or suppress oscillations when $p = 1$. For the piecewise quadratic case, limiter 4 is used, again for the purpose of enforcing some form of TVB-stability.

For this problem, experimental results show that the basic scouring process and flow profile evolution may be summarized as follows. The initial

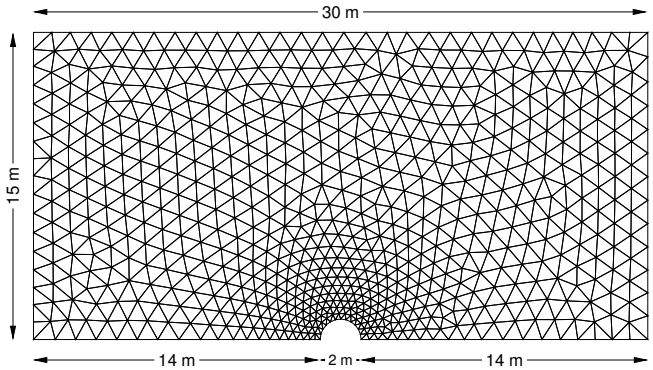

(a) Coarse-scale mesh, containing 1327 elements

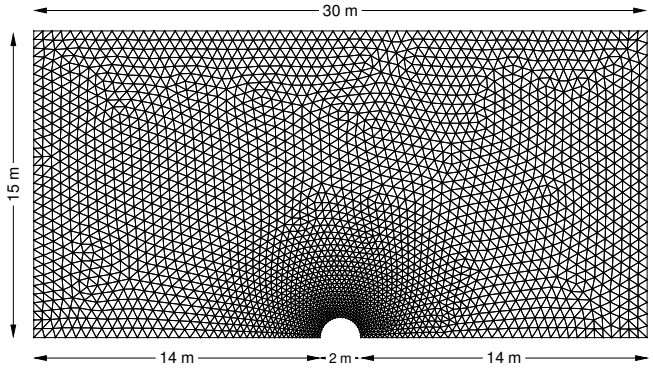

(b) Fine-scale mesh, containing 5308 elements

Figure 4.11: Unstructured meshes used for the pile test case

approach flow splits in the horizontal direction when reaching the pier into an upper and lower flow, leaving a stagnation point at the head of the pier (the point $(-1, 0)$ in Ω_h). A corresponding stagnation pressure results; fluid approaching the stagnation point decelerates, causing some pileup (and thus an increase in ζ) [87] and a bow wave, and then accelerates along the sides of the pier [58]. The fully developed flow speed along the pier perimeter reaches its maximum at an angle $\theta \approx 75^\circ$ from the pier head, but then separates in the region $90^\circ \leq \theta \leq 120^\circ$ as a result of the acceleration along the sides [181], and a long wake results. Meanwhile, scouring of the bed is initiated near $\theta \approx 75^\circ$, closely corresponding to the point where the (attached) accelerating flow reaches its maximum speed [181]. Sediment accretion occurs just downstream of the pier, and the mound slowly drifts downstream with time because of the growing scour hole [181].

However, it should be noted that in addition to this, the approach flow also splits in the vertical direction at the upstream stagnation point; the up-flow contributes to the formation of the bow wave, while the down-flow forms a vertical eddy or vortex [58]. Because of accelerating flow around the pile, a horseshoe vortex system is subsequently formed, and this has been deemed to be the main scouring agent upstream of the pier [58, 181]. Thus, in time, the scour hole advances upstream, eventually becoming U-shaped [58]. Note that this latter process is inherently a three-dimensional effect, and consequently cannot be properly simulated with a two-dimensional model. Testing will proceed with this caveat in mind.

The resulting bed profiles are shown in Figure 4.12 for the coarse-scale mesh and in Figure 4.14 for the fine-scale mesh. The corresponding velocity profiles are displayed in Figure 4.13 for the coarse-scale mesh and in Figure 4.15

for the fine-scale mesh. In all results, the locations of the stagnation points, scouring initiation points, points of maximum flow speed along the perimeter, and flow separation points appear to be in good agreement with the results presented in [87] and [181].

In Figures 4.12 and 4.14, it can be seen that scouring emanates from a point on the pier perimeter near $\theta = 75°$, which agrees with experimental data in [181], and then is deposited just downstream of the pile, as should be expected. However, the extent of the scouring varies considerably between the coarse- and fine-scale meshes, especially when $p \geq 1$; h-refinement near the bridge pier appears to play a significant role here in the accurate calculation of the sediment transport rate. Also, when $p \geq 1$, the resolution of the scour hole seems to be slightly improved, and its extent appears to be reduced. The same may be observed with the corresponding velocity profiles: the wake appears slightly sharper and more compact (although the flow seems to separate slightly too far downstream compared to the coarse-scale solution, which shows separation around $\theta = 120°$), as does the flow near the upstream stagnation point.

By closely observing the differences in the scouring and accretion profiles when $p \geq 1$, the following may be noted. When $p = 1$, differences between the coarse- and fine-scale solutions are quite apparent; the coarse-grid scour hole appears smeared, and simply emanates outward at $\theta \approx 75°$, while the fine-grid hole exhibits a downstream tail. Its visual appearance is similar to that of the $p = 2$ coarse-grid solution. While the corresponding fine-grid solution for $p = 2$ shown in Figure 4.15(c) displays some additional structure, it is not substantially qualitatively different. Consequently, the piecewise quadratic approximations of b may possibly be showing some signs of convergence (al-

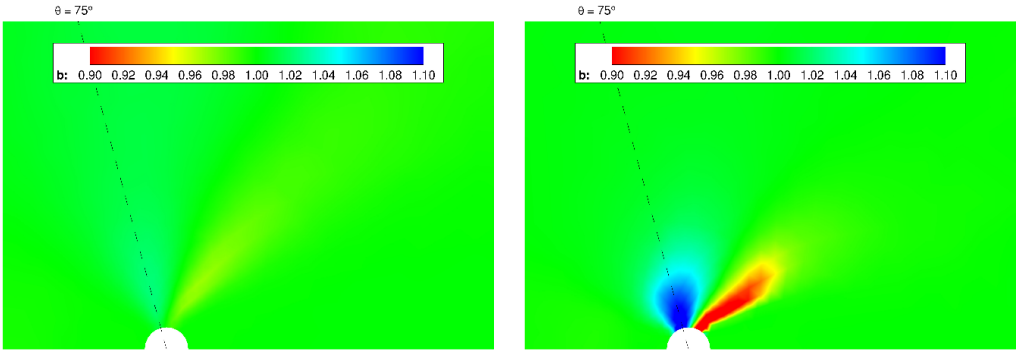

(a) Bathymetry (m) with $b_{hp}|_{\Omega_E} \in \mathcal{P}^0(\Omega_E)$ (b) Bathymetry (m) with $b_{hp}|_{\Omega_E} \in \mathcal{P}^1(\Omega_E)$

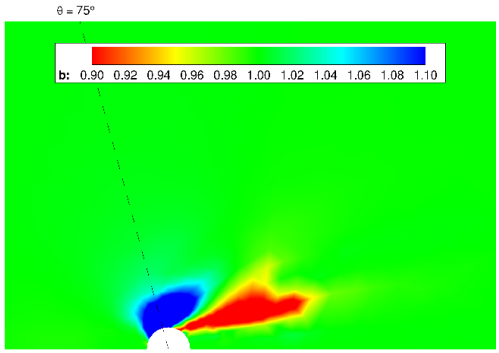

(c) Bathymetry (m) with $b_{hp}|_{\Omega_E} \in \mathcal{P}^2(\Omega_E)$

Figure 4.12: Bed profiles after 1 day on the coarse mesh

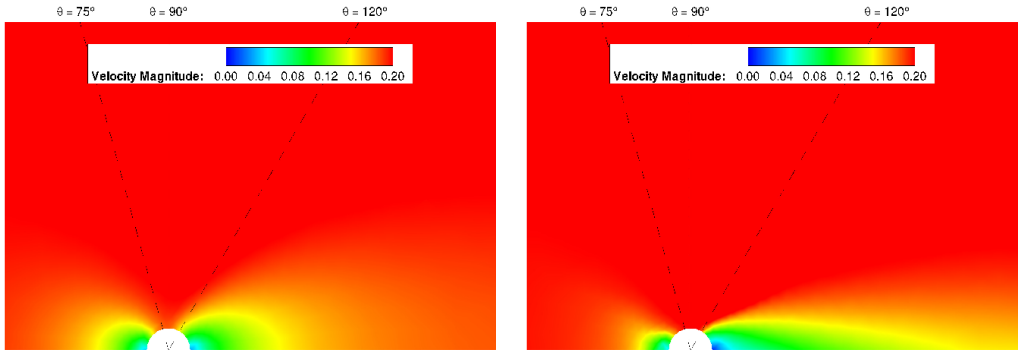

(a) Flow speed (m/s) with $p = 0$

(b) Flow speed (m/s) with $p = 1$

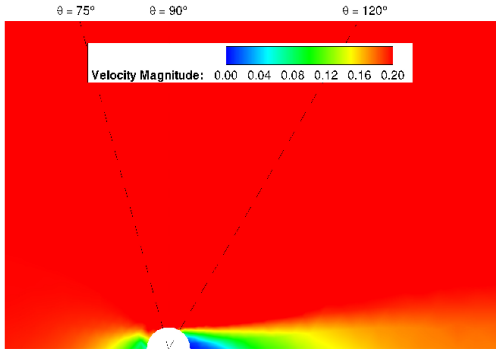

(c) Flow speed (m/s) with $p = 2$

Figure 4.13: Velocity profiles after 1 day on the coarse mesh

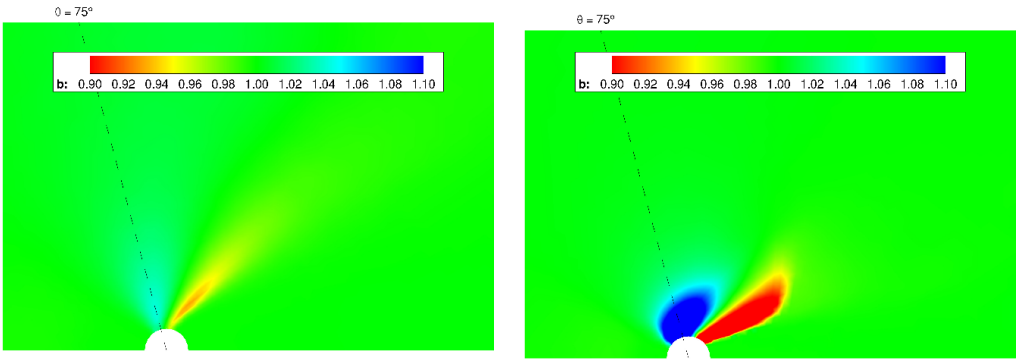

(a) Bathymetry (m) with $b_{hp}|_{\Omega_E} \in \mathcal{P}^0(\Omega_E)$ (b) Bathymetry (m) with $b_{hp}|_{\Omega_E} \in \mathcal{P}^1(\Omega_E)$

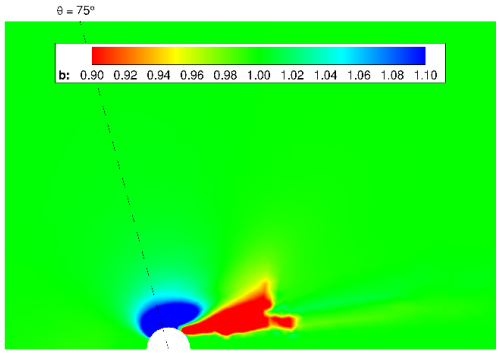

(c) Bathymetry (m) with $b_{hp}|_{\Omega_E} \in \mathcal{P}^2(\Omega_E)$

Figure 4.14: Bed profiles after 1 day on the fine mesh.

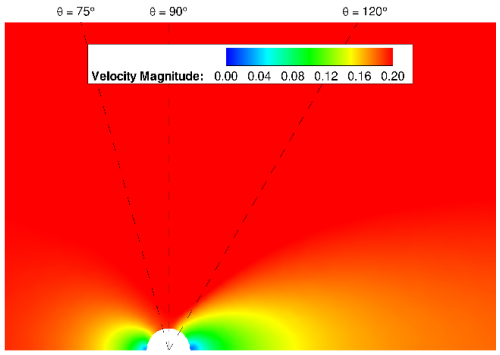

(a) Flow speed (m/s) with $p = 0$

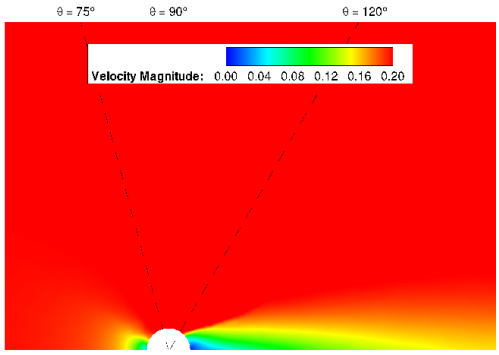

(b) Flow speed (m/s) with $p = 1$

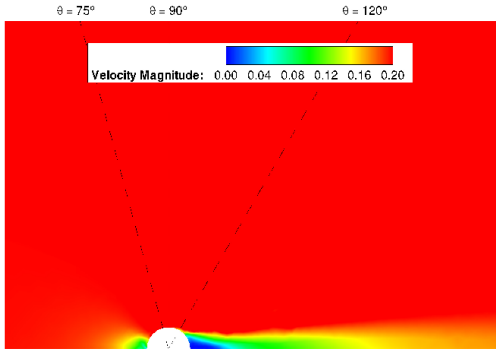

(c) Flow speed (m/s) with $p = 2$

Figure 4.15: Velocity profiles after 1 day on the fine mesh

though additional trials would be needed to verify this).

Many differences in the bed evolution can be remarked upon among the cases for $p = 0$, 1, and 2. For the piecewise constant case, notice that the eroding and accretion regions extend nearly two-thirds of the way to the domain boundary. This is clearly unrealistic, since both experimental and analytical investigations suggest that the boundary of the scour hole lies much closer to the pile [58]. Thus, the RKDG scheme with $p = 0$ seems to be much too diffusive, and this demonstrates the need for increasing p to sufficient order. Also, the maximum scour and sediment accumulations are far less than the maxima attained for the other two cases, possibly indicating that the calculated values of $\tilde{\mathbf{q}}$ may be too low. This agrees with our observations in Section 4.2. When p is increased to 1, a more realistic result emerges, as the area of erosion and deposition is constrained to a distance not exceeding approximately $2D$. The higher scouring and accretion rates may be attributed to the larger velocity gradients seen in Figures 4.13(b) and 4.15(b), especially in the wake, whose width is now much smaller; it is not smeared. The piecewise quadratic solutions appear even less diffusive, even with the use of the higher-order slope limiter: an even larger amount of sediment pick-up occurs in a still smaller scour hole located closer to the pier compared with the $p = 1$ case, and the ends of the U-shape attained by the scour hole are more evident. The wake and upstream stagnation regions are more compact as well. Additionally, observe that the accretion region emanates outward at a larger angle θ as p is increased. It should be noted, however, that the general lack of diffusion seen in these results for $p \geq 1$ is primarily a numerical phenomenon, and it is a consequence of setting $\mathsf{D} = 0$ in equation (2.1.1); some physical diffusion will be seen in reality.

Lastly, it is noted that examination of the elevation profile for all model runs revealed strong numerical evidence of a bow wave, as values of ζ were elevated near the upstream stagnation point where seawater pileup is expected. However, for the sake of brevity, these results are not shown here.

4.4 An Idealized Inlet

Attention is now turned toward a coastal modeling application. In this test case, an idealization of a typical coastline, channel, and bay or estuary is considered. For this case, it is wished to ensure that the model properly captures the twin eddy formation in the back bay during an incoming (flood) tide, the corresponding formation in the ocean during an outgoing (ebb) tide, the formation of an ebb shoal in the ocean off the ends of the jetties, and the formation of a corresponding flood shoal in the back bay. Ebb and flood shoal formation is very common in both coastal inlets and river deltas, and they form as a result of sediment accretion caused by decelerating flow exiting the channel during the ebb and flood tides, respectively. Though the time scales are generally on the order of months to many years (assuming fair weather), this process, left unchecked, can severely alter the flow patterns of an inlet and disrupt shipping operations, and the ensuing dredging operation may be very expensive. Thus, analysis of these systems serves an important purpose. An example of an ebb and flood shoal is shown in Figure 4.16.

The domain under consideration is shown in Figure 4.17. It is a simplified, or idealized, inlet containing a channel 300 m wide and 525 m long which connects a rectangular section (stretching 3 km north to south and 2.475 km out to sea) of open ocean to the west with a rectangular back bay (spanning 3 km north to south and 1.5 km inland) to the east. At the western end of the

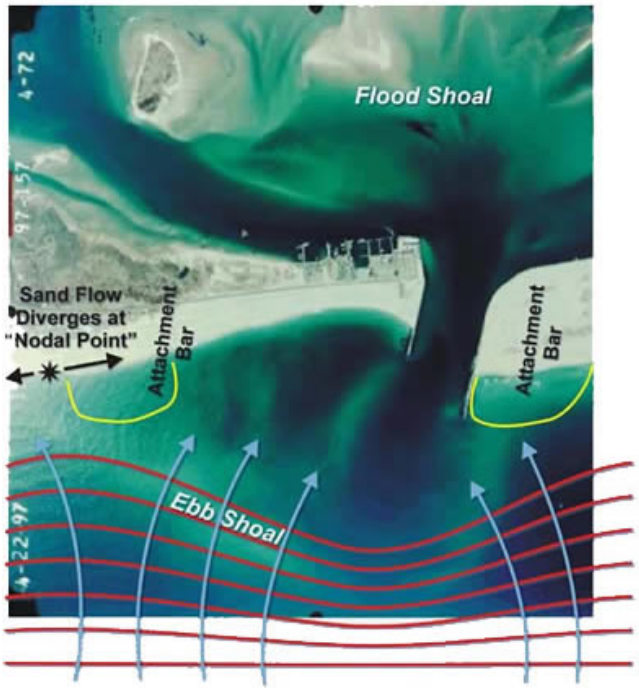

Figure 4.16: Ebb and flood shoal formation in Shinnecock Inlet, NY. Credit: NOAA Coastal Services Center

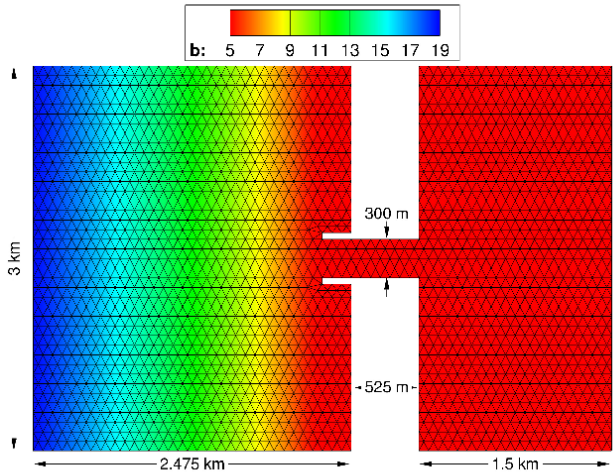

Figure 4.17: Computational domain of the idealized inlet system containing 4374 elements. The initial bathymetry (m) is shown as well. The jetties are 225 m long by 50 m wide.

channel are twin jetties 50 m wide and 225 m long. The initial bathymetry in the back bay and channel is flat and measures 5 m, while the bottom slopes linearly in the open ocean to the west, measuring 19 m at the western open ocean boundary. The water in the sea, channel, and back bay is initially tranquil.

The boundary conditions for this problem are as follows: a land BC is imposed at the northern, southern, and eastern edges of the open ocean, as well as at the jetties, channel walls, and all edges of the back bay. On the western open ocean boundary, a spatially uniform periodic normal discharge rate $\mathbf{q}_D \cdot \mathbf{n}$ is prescribed, with an amplitude of $0.75\,\mathrm{m}^2/\mathrm{s}$, and a frequency corresponding to that of the M_2 tide (period $12^{\mathrm{h}}25^{\mathrm{m}}14^{\mathrm{s}}$). This amplitude was chosen so that the maximum flow speed in the channel is approximately 1 m/s.

This test case is solved over a period of 10 days using piecewise constant,

linear, and quadratic basis functions for the purpose of comparison. For the piecewise constant approximation, a time step size of 1.25 s with SSP(1,1) is used; for the piecewise linear approximation, 0.5 s with SSP(2,2); for the piecewise quadratic approximation, 0.25 s with SSP(3,3). Recall once more from Section 2.5 that for the sediment transport equation, slope limiter 1 is applied when $p = 1$, and the higher-order slope limiting procedure of Xu *et al.* [193] is applied when $p = 2$. The bed remains non-porous, with the same value for d_{50} as in Section 4.2. However, the grain density is now increased to 2650 kg/m^3. The nonlinear bottom friction coefficient c_f is increased to 0.003 for this case. Additionally, the sediment transport rates were magnified 50 times in order to speed up the bed evolution process. This was done in the interest of saving computational time.

Figures 4.18(a)–4.18(c) show plots of the piecewise constant, linear, and quadratic approximations of b after 10 days, respectively, in the vicinity of the channel. The other areas of the domain experience negligible amounts of sediment transport, and so are not shown here; the most interesting flow features are found in the channel region. The most prominent of these is the formation of dual scour holes in the center of the channel—one located at the entrance to the back bay, the other just off the ends of the twin jetties. These scour holes are caused primarily by converging accelerating flow during the incoming tide (for the hole near the jetties) and during the outgoing tide (for the hole at the bay entrance). This dual scour hole formation is consistent with what is observed in real channel-inlet systems, such as Shinnecock Inlet, NY, where bathymetric soundings reveal dual scour holes in approximately the same locations as described above (though these are slightly off-center because the channel is not straight, as can be seen in Figure 4.16). The jagged shape

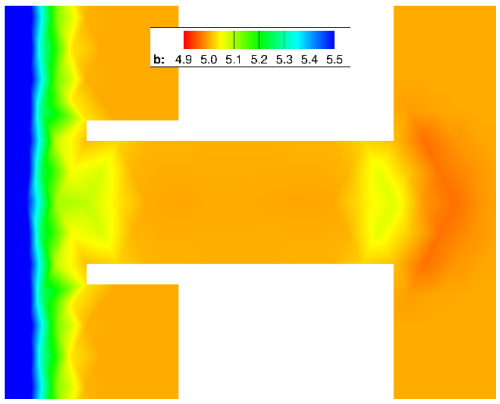

(a) Bathymetry (m) with $b_{hp}|_{\Omega_E} \in \mathcal{P}^0(\Omega_E)$

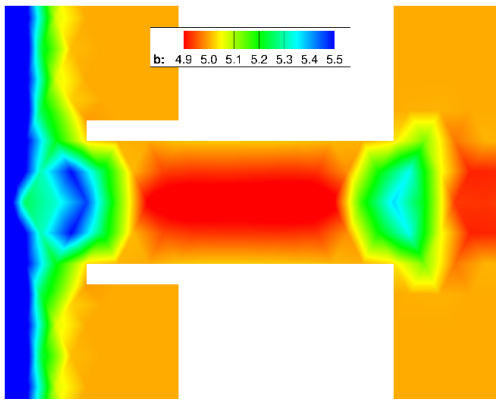

(b) Bathymetry (m) with $b_{hp}|_{\Omega_E} \in \mathcal{P}^1(\Omega_E)$

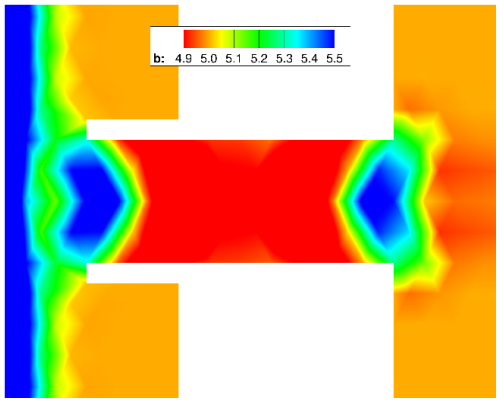

(c) Bathymetry (m) with $b_{hp}|_{\Omega_E} \in \mathcal{P}^2(\Omega_E)$

Figure 4.18: Bathymetry (m) in the channel region after 10 days.

of the scour holes is a direct result of the relative coarseness of the mesh in this region (see Figure 4.17); this grid size was chosen as a compromise between resolution and computational time.

Notice also in Figures 4.18(b) and 4.18(c) that sediment accretion occurs in the center of the channel. This phenomenon is due to the slightly negative velocity gradient existing there for most of the duration of the M_2 tidal cycle. See Figures 4.19 and 4.20, and observe the channel center. These results suggest a mechanism by which channels could fill in over longer time periods and possibly block the flow, posing a hazard to shipping interests, however, this requires further investigation. Finally, notice the formation of ebb and flood shoals beyond the scour holes, which are also caused in part by the negative velocity gradients in these regions during the ebb and flood tides, respectively.

Comparing the results across the different values of p, it is gleaned that the piecewise constant approximation of b once again fails to capture the full extent of the induced bed evolution: the scour hole depths are approximately 9 and 7 cm at the jetties and back end, respectively, compared with 49 and 36 cm for the piecewise linear case and approximately 55 cm (both ends) for the piecewise quadratic case. It should be noted, however, that values for the scour hole depths for $p \geq 1$ are highly dependent on the use of the slope limiter; it should be made clear that without the use of a slope limiter, runaway scouring will eventually occur, and the resulting scour hole depths will become non-physically large, leading to numerical instability. In any case, the depths were substantially higher than those obtained when $p = 0$.

The maximum speed in the channel is approximately 0.2 m/s lower when $p = 0$ compared with $p > 0$, and since the sediment discharge rate

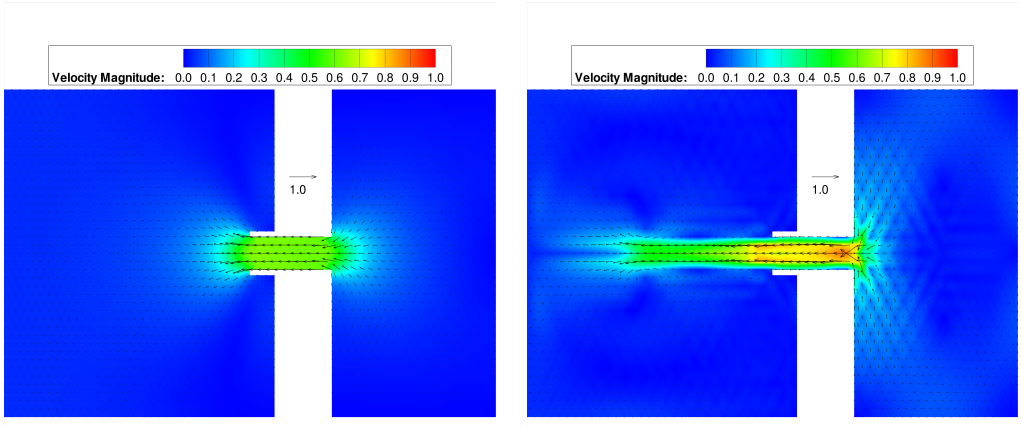

(a) Velocity profile (m/s) with $p = 0$

(b) Velocity profile (m/s) with $p = 1$

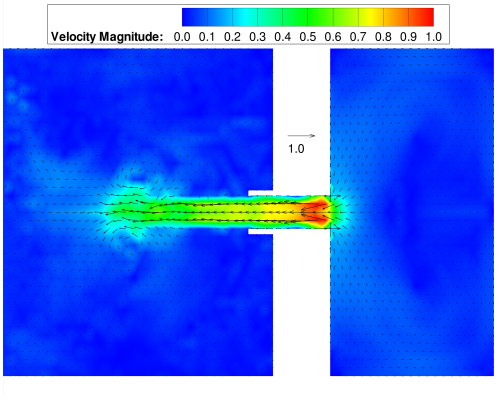

(c) Velocity profile (m/s) with $p = 2$

Figure 4.19: Velocity profiles during approximate maximum ebb

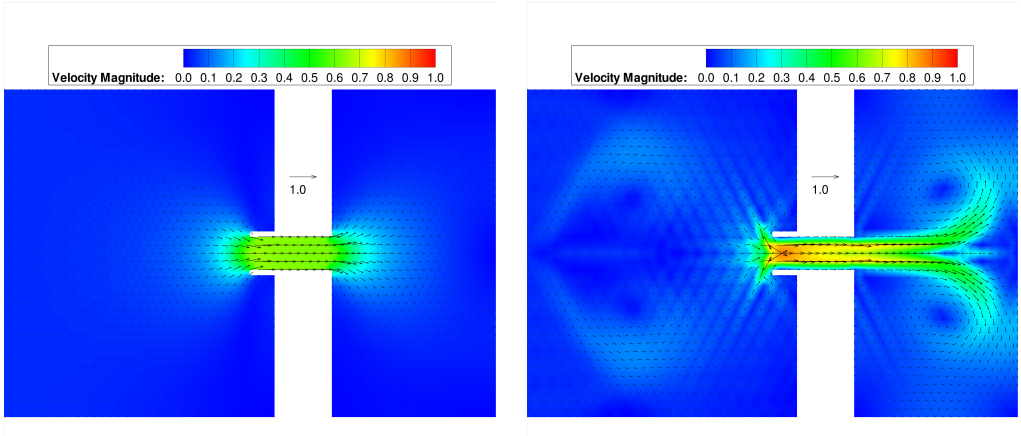

(a) Velocity profile (m/s) with $p = 0$

(b) Velocity profile (m/s) with $p = 1$

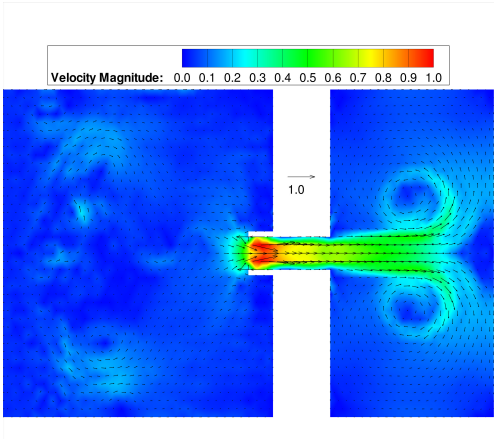

(c) Velocity profile (m/s) with $p = 2$

Figure 4.20: Velocity profiles during approximate maximum flood

depends on $\mathbf{q}^3$, the induced transport rate is lower. Low deposition rates for this case result in scant evidence of ebb and flood shoal formation, and of accretion in the channel center. These low observed rates of sediment transport compared to higher-order approximations are again consistent with what was seen in Sections 4.2 and 4.3.

Seeking a higher-order approximation of $\mathbf{w}$ yields a dramatic improvement in resolution, as numerical evidence for ebb and flood shoal formation is clearer, and sediment accretion in the center is more easily seen. The solution for the case of $p = 2$ appears to be even less diffusive; the scour holes are now very well defined, as is the accretion in the channel center.

For this test case, as alluded to earlier, it is worthwhile to examine the velocity profiles at two different times—during the approximate time of maximum ebb, which is the time in which the seaward current associated with the outgoing tide is the strongest, and during the approximate time of maximum flood, when the incoming tidal current is the strongest. Figure 4.19 shows the flow profile for $p = 0$, 1, and 2 at maximum ebb. Immediately it is seen that the numerical solution for the piecewise constant approximation of $|\mathbf{u}|$ is unrealistically simple; the model cannot resolve the dual eddies that form in the ocean as a result of interaction with the jetties. Even within the channel, the grid- and subgrid-scale flow features are not well resolved. This changes drastically when $p \geq 1$, as Figure 4.19(b) reveals two sets of dual eddies. One of these is a pair of jetty-scale eddies appearing in the ocean near the leading edge of the main seaward current coming from the channel. A pair of kilometer-scale eddies in the back bay is present as well, and these are residual eddies which contain remnants of the seawater transported into the bay during the previous incoming tide. They supply the seawater mass for the

return flow. The $p = 2$ solution appears to give slightly better resolution of these large-scale eddies. Notice also that the solutions for $p \geq 1$ reveal much greater detail within the channel, especially near the scour holes, where small regions of increased velocity are seen. In addition, long, thin tails of slow-moving seawater are present near the channel walls—a feature not seen in the $p = 0$ case, but consistent with results shown in [101]. Grid- and subgrid-scale velocity gradients are better resolved here, too, specifically in the piecewise quadratic case. All of these observations underscore the need to take $p \geq 1$ in order to obtain a reasonable flow profile.

The velocity profiles for the opposite tidal phase are shown in Figure 4.20. Similar remarks from the previous paragraph about the solutions for the different values of p apply here as well: the numerical solution for $p = 0$ is still far too simplistic, while the piecewise linear approximation only partially resolves the (now clearly visible) dual eddies in the back bay, which appear to be nearly fully resolved only when $p = 2$ (shown in Figure 4.20(c)). These observations and results are consistent with those in [101]. Note, however, that during the flood tide, a pair of unnatural residual kilometer-scale eddies remain in the ocean, which is likely a result of the interaction between the outgoing current (originating from the channel) and the flow-specified western boundary: they likely are deflected back into Ω_h and do not dissipate quickly enough since $\mathsf{D} = 0$. This not only highlights the issues relating to numerical diffusion, or lack thereof, but also highlights the ongoing issue of proper specification of open ocean boundary conditions in the framework of the DG method. Both issues require further investigation.

As was the case during maximum ebb, the cross-stream flow features are better resolved when p is increased to at least one, and they are very

well resolved when p is increased to two, which successfully captures the more complex features. Specifically, consider the flow between the jetties: the maximal speed occurs at two locations in this region, compared to just one when $p = 1$. Obviously, this phenomenon occurs during the outgoing tide as well, but is not quite as easily discerned in Figure 4.19(c) because the time does not correspond precisely with that of maximum ebb. Again, these results agree with those presented in [101], and the presence of multiple local maxima in $|\mathbf{u}|$ suggest the presence of multiple local maxima in b as well. This is indeed the case, and may be spotted in Figure 4.18(c). Thus, the corresponding bed profile may be thought of as possessing a dual-dual scour hole arrangement, rather than simply a dual setup as seen in Figure 4.18(b).

4.5 Surge into a Barrier-Protected Lowland

In this section, the objective is to test the ability of the wetting and drying algorithm described in Section 2.5.5 to capture the behavior of the flow and transport when a region of the computational domain contains dry elements. It also provides the opportunity to investigate the nature of sediment transport near man-made structures such as sea walls. Obtaining qualitatively reasonable results for test cases such as this one are a prerequisite for running simulations involving extreme storm events, in particular Hurricane Ike. This is because computational domains that encompass the Gulf of Mexico and other coastal areas often contain dry areas that lie below mean sea level, such as the city of New Orleans, which is protected by an extensive levee system.

Consider the domain and initial bathymetry shown in Figure 4.21. It is a structured grid containing two rectangular regions of elements separated by a barrier 45 km long, 3750 m wide, and 0.1 m high relative to the datum. That

is, $H_{\text{ibar}} = 0.1\,\text{m}$. The (initially) dry region is located to the west of the barrier; the wet region, to the east. On the western boundary lies another barrier, with a height of $H_{\text{ebar}} = -0.5\,\text{m}$. The two barriers are situated on either end of the (initially) dry region, and are meant to partially impede incoming flow from the wet region. Finally, the open ocean lies at the eastern boundary.

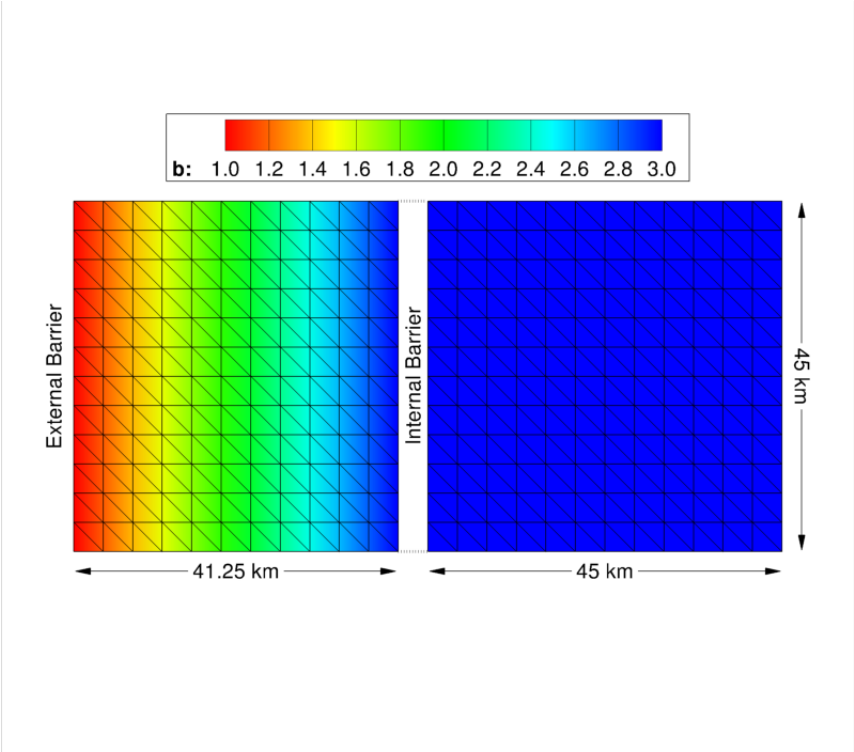

Figure 4.21: Computational mesh containing 552 elements used in the barrier test case. The initial bathymetry (m) is also shown.

The boundary conditions are summarized in Table 4.5 and are as follows: a land BC is imposed at the northern and southern boundaries. On the western boundary, an external barrier BC is enforced. An internal barrier BC is imposed on both sides of the barrier separating the wet and dry regions. Finally, on the eastern boundary, an open BC is specified, with ζ_D spatially

uniform with an amplitude of 1 m and a frequency corresponding to that of the M_2 tide (period $12^{\mathrm{h}}25^{\mathrm{m}}14^{\mathrm{s}}$). This amplitude was chosen so that the internal barrier is over-topped during each tidal cycle. However, in addition, ζ_D is controlled by a ramping function

$$R(t) = \begin{cases} \tanh\left(\frac{4(t-t_0)}{86400D}\right), & t - t_0 < 86400D, \\ 1, & t - t_0 \geq 86400D, \end{cases} \tag{4.5.1}$$

where D is the ramping duration (in days); in this case $D = 2$. This is done to prevent shocking the system. The internal and external barriers are ramped using equation (4.5.1) as well. The initial time t_0 is set to zero.

Boundary (Units: km)	BC type	Data
$\{(x, 0) : x \in (60, 150)\}$	Land	
$\{(x, 45) : x \in (60, 150)\}$	Land	
$\{(60, y) : y \in (0, 45)\}$	Ext. barrier	$D = 2\,\mathrm{days}$ $H_{\mathrm{ebar}} = -0.5\,\mathrm{m}$ $C^S_{\mathrm{ebar}} = 1$
$\{(101.25, y) : y \in (0, 45)\}$	Int. barrier (front)	$D = 2\,\mathrm{days}$ $H_{\mathrm{ibar}} = 0.1\,\mathrm{m}$ $C^s_{\mathrm{ibar}} = C^S_{\mathrm{ibar}} = 1$
$\{(105, y) : y \in (0, 45)\}$	Int. barrier (back)	$D = 2\,\mathrm{days}$ $H_{\mathrm{ibar}} = 0.1\,\mathrm{m}$ $C^s_{\mathrm{ibar}} = C^S_{\mathrm{ibar}} = 1$
$\{(150, y) : y \in (0, 45)\}$	Open	$\zeta_D = R(t)\cos(\omega_{M_2} t)$ $\omega_{M_2} \approx 1.405 \times 10^{-4}\,\mathrm{s}^{-1}$ $D = 2\,\mathrm{days}$

Table 4.5: Boundary conditions for the barrier test case

This test case is solved over a period of 5 days using piecewise constant and linear basis functions. Piecewise quadratic basis functions are not used here; this is a limitation of the wetting and drying algorithm. In both instances, the time step size was 20 s, which is well below the necessary threshold given

by the CFL condition. As with the previous test cases described in Sections 4.1–4.4, the forward Euler scheme SSP(1,1) was used when $p = 0$; the SSP(2,2) scheme, when $p = 1$.

The initial bathymetry (shown in Figure 4.21) is given by the piecewise linear function

$$b_0(x) = \begin{cases} 1 + (2/41250)x, & x \in (60000, 101250), \\ 3, & x \in (105000, 150000). \end{cases}$$

That is, the bed initially lies 0.5 m below the top of the external barrier, slopes linearly to the east, lying 3.1 m below the top of the internal barrier. The initial depth is $H_{\min} = 0.2\,\text{m}$ in the initially dry region, and 3 m in the wet region to the east of the internal barrier. Note that when $p = 0$, the bed in the dry region cannot be faithfully represented; the consequences of this will be apparent below.

The sediment transport function used for this case is given by $\tilde{\mathbf{q}} = AH^{-3}|\mathbf{q}|^2\mathbf{q}$, where $A = 0.05$, which was chosen to simplify the implementation of the NCP numerical flux described in Section 2.4.3. As with previous test cases, $\kappa = 1$, but now, for simplicity, linear bottom friction is used, with $\tau_{\text{bf}} = 0.003$. Lastly, the slope limiting operator $(\Lambda\Pi) = I$.

Figure 4.22 shows the difference in bathymetric depth (denoted Δb) since the start of the simulation; $\Delta b > 0$ indicates erosion; $\Delta b < 0$, deposition. In Figure 4.22(a), where $p = 0$, it can be seen that after 5 days, significant deposition has occurred on the western side of the internal barrier. Also, the bed has undergone very slight erosion near the open boundary and external barrier. Negligible amounts of sediment transport occur elsewhere. However, since $Hu < 0$ and $Hv \approx 0$ for nearly the duration of the simulation, and since bed load transport is in the direction of the flow, the deposition occurring

along the internal barrier is both unexpected and unrealistic. This is likely a consequence of the bed not being represented accurately in this region, which introduces artificial jumps along element boundaries, thus initiating sediment transport when it would otherwise not occur once the elements in question become wet.

On the other hand, when $p = 1$, significant scouring occurs along the front edge of the internal barrier, while small amounts of deposition occur near the external barrier (and near the southern land boundary), as shown in Figure 4.22(b). Scouring near the barrier is a more realistic effect, compared with the accumulation seen when $p = 0$, because it is a result of accelerating westward flow, which takes place whenever the barrier is over-topped (from the back, or eastern, side), which occurs every tidal cycle. More noticeable erosion (compared with the piecewise constant case) occurs near the open boundary, although this phenomenon is likely an artifact of the BC. Notice also that the bed profile is smooth and nearly symmetric[2] seaward of the barrier, but contains oscillations in the protected region. A portion of this "noise" can be attributed to the wetting and drying algorithm itself; a known side effect of the scheme is the high-frequency "flickering" of elements from wet to dry and *vice versa* between time steps [24].

Turning attention to the elevation profiles, it is seen in Figure 4.23(b) that the initially dry region has now flooded, with the elevation increasing by approximately 80 cm near the internal barrier. Smaller increases are present as one moves west toward the external barrier. Comparing this with Fig-

[2]The asymmetry observed in Figures 4.22(a), 4.22(b) (near the open boundary), and 4.23 is spatial interpolation error introduced by the visualization software, which only accepts the first degree of freedom as data.

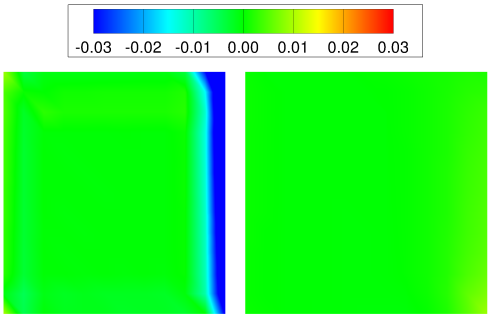

(a) Bathymetry difference (m) with $p = 0$

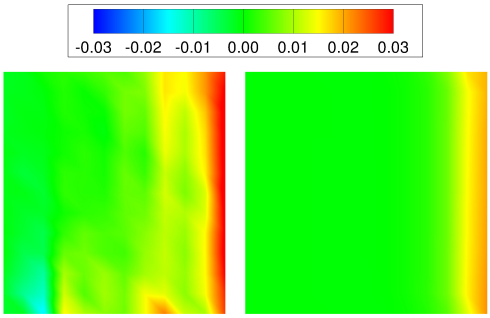

(b) Bathymetry difference (m) with $p = 1$

Figure 4.22: Bathymetry difference (m) after 5 days with $p = 0$ and $p = 1$

ure 4.23(c), an immediate observation is that elevation changes are far less drastic when p is increased to one; the scheme appears to be far less numerically diffusive. As a consequence, rapidly accelerating flow caused by over-topping induces high erosion rates there, because the seawater is much more shallow than when $p = 0$. The flood wave does not dissipate in the protected region, but instead over-tops the external barrier, leaving Ω_h and carrying bed load with it. Finally, it should be pointed out that although Figures 4.23(b) and 4.23(c) appear to display a loss of seawater mass on the seaward side of the internal barrier, this is in fact simply the stage of the tidal cycle, combined with the effect of bottom friction.

Before leaving this example, a few closing remarks seem appropriate. It should be stressed that the results shown in this section are preliminary as of publication time, and that work is currently ongoing. Yet even so, as the behavior of the bed near the internal barrier is inconsistent with the local flow profile when $p = 0$, the dangers of utilizing FV-based models in cases such as this are exposed. As regards the case of $p = 1$, the limitations of the wetting and drying scheme are revealed, as not only do elements sometimes "flicker", but they tend to wet and dry in waves, wetting when the flood wave from the over-topped barrier reaches them, drying after it has passed. Yet the results do suggest that the scouring of the seabed along the internal barrier, if left unchecked, would eventually damage the structure, and potentially even destroy it.

4.6 Parallel Performance

This chapter concludes with some brief remarks on the performance aspect of the model when run in parallel. The numerical results presented in

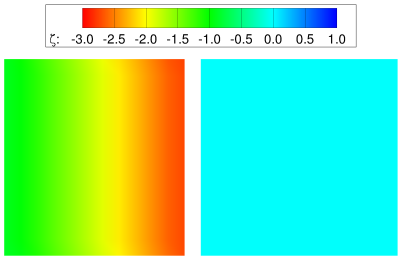

(a) Initial elevation (m)

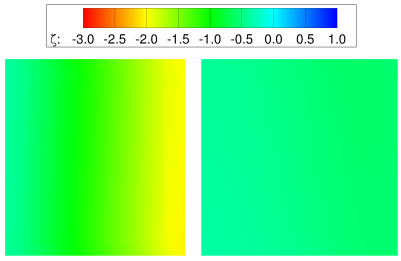

(b) Elevation (m) with $p = 0$

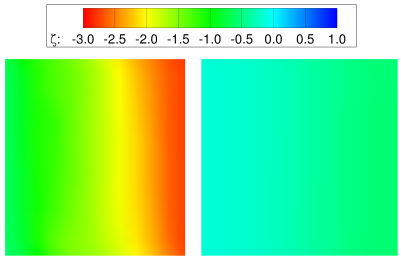

(c) Elevation (m) with $p = 1$

Figure 4.23: Elevation (m) for (a) the initial time (b) after 5 days with $p = 0$ and (c) after 5 days with $p = 1$

the previous four sections have focused on the improved accuracy in $\mathbf{w}_{hp}$ with increasing p. However, this improvement in accuracy comes with the price of additional computational costs as p is increased. For example, increasing p from zero to one triples the number of degrees of freedom, and, in the case of the converging channel with the coarse grid, requires twice as many time steps. Also, additional computational work is needed to evaluate the interior and edge integrals, as more quadrature points are required. An attempt is made to quantify the amount of extra work required in the test case that follows.

Consider once again the converging channel test case described in Section 4.2. For this trial, only the coarse grid is considered. The objective is to measure the relative CPU times when the model is run for $p = 0$, 1, and 2. The model is run using the same parameters as those described in Section 4.2, except that the model is run for 1 day, instead of 90 days. For each run, 4 processors were utilized on a Dell PowerEdge cluster located at the Institute for Computational Engineering and Sciences (ICES) at The University of Texas at Austin (`bevo2`).

The results of these three model runs are shown in Table 4.6. As can be observed there, using piecewise linear basis functions instead of piecewise constant ones results in a nearly six-fold increase in CPU time, and using piecewise quadratic basis functions leads to a sixteen-fold increase. Both values are well below estimates which account for increases in the number of degrees of freedom, Runge–Kutta stages, time steps, and quadrature points. Since the run-time optimization process is sophisticated, this phenomenon requires additional investigation; the reader is cautioned that the results shown here are preliminary; a much more thorough scaling and performance analysis is

p	Δt (s)	SSP(s,k)	CPU time (s)	Ratio
0	1.50	1, 1	24.56	1.00
1	0.75	2, 2	139.40	5.68
2	0.50	3, 3	394.42	16.06

Table 4.6: Relative computational costs for solving the channel test case

currently planned.

4.7 Discussion and Remarks

In this chapter, a well-balanced (as demonstrated in [153]) DG morphological model was implemented within the ADCIRC modeling framework by following an extended approach which specially treats the nonconservative products through the addition of stabilizing terms in the numerical flux. An investigation of the resulting RKDG method was made, and it was verified that the scheme maintains first- through fourth-order accuracy away from shocks prior to their formation, provided that the mesh is sufficiently h-refined in the shock vicinity; the theoretical convergence rates were nearly attained in these cases.

Effects of h- and p-refinement were readily seen in the test cases: numerical solutions appeared to converge to those with the lowest values of h and highest values of p, with the highly-refined approximations able to capture subgrid-scale features, especially in the transition regions near scour hole boundaries. Moreover, it was observed that sufficient p-refinement (and to a lesser extent, sufficient h-refinement) is necessary for the accurate computation of sediment transport rates. That is, very low-order p approximations resulted in artificially low sediment pick-up, even with highly amplified transport formulæ, and the method appeared to be too diffusive. This latter point must be

emphasized: since finite volume models are in fact equivalent to DG models with $p = 0$, the numerical results in Sections 4.1–4.6 suggest that FV-based models can yield poorly-resolved sediment solutions.

Although it is clear that a three-dimensional model is required to accurately resolve all the flow features around structures such as bridge piers, it was discovered that this morphological model does capture a surprising number of flow characteristics, including those of the wake, scour hole shape and location, accretion region, and points of flow separation.

Additionally, it was demonstrated that the use and selection of a slope limiter plays a crucial role in improving the solution quality in these cases. This was especially true for higher-order approximations, as its omission resulted in significant spurious oscillations in the solution, and even instability in some extreme cases. Inclusion of a higher-order slope limiter is therefore critically important for DG morphological models which accommodate arbitrary-order solution approximation.

Lastly, it was verified that the wetting and drying algorithm proposed in [24], although prone to generate somewhat noisy solutions, stably rectifies the problem of meshes containing dry elements and regions, even when bed movement is allowed. The model was also shown to handle artificial flow controls reasonably well, and was shown to possess the ability to capture interaction between the barriers and seabed.

Chapter 5

Concluding Remarks and Future Directions

In this final chapter, some general observations about the analytical and numerical results discussed in the previous chapters are given. These concluding remarks appear in Section 5.1. This is followed by a discussion of potential future research directions, short- and long-term goals, and open problems in Section 5.2.

5.1 Concluding Remarks

This dissertation describes the development of a tightly-coupled hydrodynamic and bed morphology model that utilizes the LDG finite element method from both a theoretical and computational viewpoint. As a result of the present study, the following observations are made:

- An alternative (L)DG formulation is required, which properly accounts for the nonconservative product appearing in the momentum equations, whenever the true solution becomes discontinuous, especially if $\mathbf{Z} = \mathbf{0}$. Additional regularity in the solution introduced by the diffusive terms does not necessarily eliminate the need for this; special treatment of $\mathbf{g}$, which gives rise to additional stabilization terms in the numerical flux, is still crucial.

- The split formulation of the numerical flux described in Section 2.4.2 is

less computationally expensive, although possibly more diffusive, than the NCP formulation described in Section 2.4.3. This is especially important if the (empirical) sediment discharge function is complicated, which many are in practice.

- A higher-order WENO-type slope limiting algorithm was implemented in order to define the operator ($\Lambda\Pi$), and was shown to perform reasonably well in practice when used with DG solutions of order two. However, as applying the algorithm to $\mathbf{w}_{hp}$ can be computationally expensive, especially as p increases, some care must be taken as to which components of $\mathbf{w}_{hp}$ the operator should be applied; it is not always necessary to apply ($\Lambda\Pi$) to all solution components.

- A wetting and drying algorithm was implemented in order to define the operator ($M\Pi$), and was shown to perform reasonably well in practice. However, it is currently designed to handle $p \leq 1$, which limits the model's robustness. This algorithm is also fairly computationally expensive, as each element must be checked at every RK stage of every time step, requiring modal-nodal transformations (and *vice versa*) each time.

- In deriving the error estimate, it was not necessary to apply Grönwall's lemma (as is typically done in the literature, *e.g.* [1, 38]), thus producing a much lower bound than would otherwise result. The price paid for this is additional tediousness in the proof.

- The estimate obtained here is similar in form to that derived in [1], except that this result requires one fewer degree of regularity for the solution $\mathbf{w}$ and inviscid flux $\mathbf{F}$, and contains additional terms arising from the nonlinear components of $\mathbf{F}$, sedimentary diffusion, and penalty

terms. As much of the work in Chapter 3 is an extension of work done in [1] and [38], this is not unexpected.

- It was verified that the scheme maintains first- through fourth-order accuracy away from shocks prior to their formation, provided that the mesh is sufficiently h-refined in the shock vicinity.

- In each of the test cases presented in Sections 4.1–4.4, the effects of h- and p-refinement were readily seen, which included the ability to capture several complex two-dimensional (but not three-dimensional) flow features near obstacles, as well as subgrid-scale features. It seems necessary to increase p to at least one in order to properly resolve many of these phenomena; piecewise constant solutions, and hence FVMs, appear much too diffusive, underestimating the transport rates and, in the case presented in Section 4.5, producing very misleading, physically inconsistent results.

5.2 Future Research Directions and Open Problems

Development of the tightly-coupled morphodynamic model described in the preceding chapters is an ongoing research effort. It should be emphasized that there are many possible research directions that could be taken by investigators in the years to come; the following is merely a small listing of recommended development paths and strategies. At present, significant future research is planned in the following areas:

- The proper formulation of BCs for all boundary types remains the subject of ongoing work by several investigators [101]. Proper BCs for $\mathbf{Z}$

appear to be even less well understood, especially on artificial flow controls such as weirs and dikes.

- An attempt should be made to consider more realistic BCs, such as those described in Section 2.5.1, as well as variable data (D, τ_{bf}, etc.) in the analysis performed in Chapter 3. This will introduce additional terms into the auxiliary equation. In addition, it would be worthwhile to consider the effect of the NCP numerical flux, as opposed to the generic one used in Chapter 3.

- A short-term, almost immediate goal is to weaken and/or eliminate the assumptions of uniform *a priori* bounds on the discrete solution in Theorem 3.2.4. An attempt should be made to show that the discrete solution components are indeed bounded from above, and that H_{hp} is bounded from below.

- Another short-term goal is to extend the higher-order slope limiter to handle polynomial approximations of degree higher than two. The algorithm described in [193] is valid for any value of $p \geq 2$, but this has not yet been fully implemented. This will make further convergence studies possible for cases in which $(M\Pi) = I$.

- As mentioned in Sections 4.5 and 5.1, a higher-order wetting and drying algorithm is not, to the best of the author's knowledge, generally available at present, although work in this area is ongoing.

- Although fully implemented, the test cases presented in Chapter 4 utilize neither hydrodynamic nor sedimentary diffusion. Since some physical diffusion is seen in reality, largely because of turbulent effects, its effect

on the numerical solutions demands further investigation. This is a short-term goal, but will require careful selection and tuning of ν_x, ν_y, $\tilde{\nu}_x$, and $\tilde{\nu}_y$; preliminary tests have revealed that model stability is highly sensitive to these parameters.

- A long-term goal is to investigate the use of quadrature-free schemes for area and edge integral computations. This may be desirable because of the growing computational cost of evaluating the numerical fluxes at each RK stage and at each time step as p increases and as problem sizes increase. Although these schemes have shown promise in terms of dramatically reducing computational costs [9, 10], questions have been raised regarding accuracy. Implementation will require an overhauling of the parallel (MPI) communication paradigm used in the model.

- A significant limitation of the current implementation is underestimation of the sediment discharge rates, particularly for low values of p, where the problem is acute. In the coastal environment, transport due to waves can play a dominating role, but this effect is neglected in this work. Therefore, alternative sediment transport models which include the effects of waves and suspended load should be investigated, such as those mentioned in Section 1.2.2.4, or that developed by Kobayashi *et al.* (2010) [98], or that implemented within SEDLIB [182], which additionally accounts for sediments containing multiple grain types and sizes (the current model assumes the bed is composed only of fine sand). Note, however, that the choice of discharge function will require some care; a delicate balance between computational cost and accuracy must be attained.

- Lastly, perhaps the most important long-term goal of model development revolves around the simultaneous simulation of storm surges and coastal morphology taking place during a hurricane. An attempt has been made in this work to lay some of the necessary groundwork for such a task to be completed. However, achieving this goal will require substantial investment of time and effort by many investigators, as the challenges remain many-fold. To name just one example, although storm surge data from previous hurricanes is available in the form of hydrographs through agencies such as the USGS, along with LiDAR soundings and charts, the issue of model validation remains unresolved because of a lack of recent bathymetric data. It is hoped that this and other problems can be overcome in the near future.

As already noted, these are just a few of the ideas worth pursuing in future studies; the list above is by no means meant to be complete. A number of other interesting directions could be taken. For example, as formulated in Chapter 2, equation (2.1.1) may be easily extended to accommodate one or more passive tracers, which may be used to simulate simultaneous hydrodynamic, sedimentary, and contaminant transport processes.

In any case, it is hoped that at some point in the future, the advantages of using a tightly-coupled model of flow and transport can be fully exploited, and the use of LDG methods for this purpose fully realized.

Bibliography

[1] V. Aizinger, *A Discontinuous Galerkin Method for Two- and Three-Dimensional Shallow-Water Equations*, PhD thesis, The University of Texas at Austin, Austin, TX, May 2004.

[2] V. Aizinger and C. Dawson, *A discontinuous Galerkin method for two-dimensional flow and transport in shallow water*, Adv. Water Resour., 25 (2002), pp. 67–84.

[3] ——, *The local discontinuous Galerkin method for three-dimensional shallow water flow*, Comput. Methods Appl. Mech. Engrg., 196 (2007), pp. 734–746.

[4] D. N. Arnold, *An interior penalty finite element method with discontinuous elements*, SIAM J. Numer. Anal., 19 (1982), pp. 742–760.

[5] D. N. Arnold, F. Brezzi, B. Cockburn, and L. D. Marini, *Unified analysis of discontinuous Galerkin methods for elliptic problems*, SIAM J. Numer. Anal., 39 (2002), pp. 1749–1779.

[6] J.-P. Aubin, *Approximation des problèmes aux limites non homogènes pour des opérateurs non linéaires*, J. Math. Anal. Appl., 30 (1970), pp. 510–521. In French.

[7] I. Babuška, *The finite element method with penalty*, Math. Comput., 27 (1973), pp. 221–228.

[8] I. Babuška and M. Zlámal, *Nonconforming elements in the finite element method with penalty*, SIAM J. Numer. Anal., 10 (1973), pp. 863–875.

[9] A. Baggag, H. Atkins, and D. Keyes, *Parallel implementation of the discontinuous Galerkin method*, ICASE Report 99-35, ICASE, Hampton, VA, Aug. 1999.

[10] A. Baggag, H. Atkins, C. Özturan, and D. Keyes, *Parallelization of an object-oriented unstructured aeroacoustics solver*, ICASE Report 99-11, ICASE, Hampton, VA, Feb. 1999.

[11] R. A. Bagnold, *An approach to the sediment transport problem from general physics*, Professional Paper 422-I, US Geological Survey, Washington, DC, 1966.

[12] J. A. Bailard, *An energetics total load sediment transport model for a plane sloping beach*, J. Geophys. Res., 86 (1981), pp. 10938–10954.

[13] A. J. C. Barré de Saint-Venant, *Note à joindre au mémoire sur la dynamique des fluides*, C.R. Acad. Sci., 17 (1843), pp. 1240–1243. In French.

[14] ——, *Théorie du mouvement non permanent des eaux, avec application aux crues des rivières et à l'introduction des marées dans leur lit*, C.R. Acad. Sci., 73 (1871), pp. 147–154, 237–240. In French.

[15] F. Bassi and S. Rebay, *A high-order accurate discontinuous finite element method for the numerical solution of the compressible Navier–Stokes equations*, J. Comput. Phys., 131 (1997), pp. 267–279.

[16] C. Berthon, B. Braconnier, and B. Nkonga, *Numerical approximation of a degenerated non-conservative multifluid model: relaxation scheme*, Int. J. Numer. Meth. Fluids, 48 (2005), pp. 85–90.

[17] K. Black, *A numerical sediment transport model for application to natural estuaries, harbours and rivers*, North-Holland Mathematics Studies, 145 (1987), pp. 77–105.

[18] J. Boussinesq, *Théorie de l'intumescence liquide appelée* onde solitaire *ou* de translation*, se propageant dans un canal rectangulaire*, C.R. Acad. Sci., 72 (1871), pp. 755–759. In French.

[19] ——, *Théorie de l'Écoulement Tourbillonnant et Tumultueux des Liquides dans les Lits Rectilignes a Grande Section*, Gauthier-Villars, Paris, 1897. In French.

[20] S. C. Brenner and L. R. Scott, *The Mathematical Theory of Finite Element Methods*, no. 15 in Texts in Applied Mathematics, Springer-Verlag, New York, third ed., 2008.

[21] N. H. Brooks, *Calculation of suspended load discharge from velocity and concentration parameters*, in Proceedings of the Federal Inter-Agency Sedimentation Conference, no. 970 in Misc. Pub., Washington, DC, Jan. 1963, US Dept. of Agriculture, US Govt. Printing Office, pp. 229–237.

[22] C. B. Brown, *Sediment transportation*, in Engineering Hydraulics, H. Rouse, ed., Wiley, New York, 1950, ch. XII, pp. 769–857.

[23] E. W. Brown, *Tables of the Motion of the Moon*, Yale Univ. Press, New Haven, 1919.

[24] S. Bunya, E. J. Kubatko, J. J. Westerink, and C. Dawson, *A wetting and drying treatment for the Runge–Kutta discontinuous Galerkin solution to the shallow water equations*, Comput. Methods Appl. Mech. Engrg., 198 (2009), pp. 1548–1562.

[25] V. Caleffi, A. Valiani, and A. Bernini, *High-order balanced CWENO scheme for movable bed shallow water equations*, Adv. Water Resour., 30 (2007), pp. 730–741.

[26] B. Camenen and M. Larson, *A general formula for non-cohesive bed load sediment transport*, Estuarine Coastal Shelf Sci., 63 (2005), pp. 249–260.

[27] Z. Cao, G. Pender, S. Wallis, and P. Carling, *Computational dam-break hydraulics over erodible sediment bed*, J. Hydraul. Eng., 130 (2004), pp. 689–703.

[28] D. E. Cartwright, *Tides: A Scientific History*, Cambridge Univ. Press, Cambridge, UK, 1999.

[29] P. Castillo, B. Cockburn, D. Schötzau, and C. Schwab, *Optimal A Priori error estimates for the hp-version of the local discontinuous Galerkin method for convection-diffusion problems*, Math. Comput., 71 (2002), pp. 455–478.

[30] M. Castro, J. M. Gallardo, and C. Parés, *High order finite volume schemes based on reconstruction of states for solving hyperbolic systems with nonconservative products. Applications to shallow-water systems*, Math. Comput., 75 (2006), pp. 1103–1134.

[31] M. J. Castro, A. Pardo, C. Parés, and E. F. Toro, *On some fast well-balanced first order solvers for nonconservative systems*, Math. Comput., 79 (2010), pp. 1427–1472.

[32] M. J. Castro Díaz, E. D. Fernández-Nieto, and A. M. Ferreiro, *Sediment transport models in shallow water equations and numerical approach by high order finite volume methods*, Comput. Fluids, 37 (2008), pp. 299–316.

[33] F. M. Chang, D. B. Simons, and E. V. Richardson, *Total bed-material discharge in alluvial channels*, Water-Supply Paper 1498-I, US Geological Survey, Washington, DC, 1965.

[34] J. G. Charney, R. Fjörtoft, and J. von Neumann, *Numerical integration of the barotropic vorticity equation*, Tellus, 2 (1950), pp. 237–254.

[35] G. Chavent and G. Salzano, *A finite-element method for the 1-D water flooding problem with gravity*, J. Comput. Phys., 45 (1982), pp. 307–344.

[36] C. Chen et al., *The unstructured grid finite volume coastal ocean model (FVCOM)*. World Wide Web, July 2011.

[37] P. G. Ciarlet, *The Finite Element Method for Elliptic Problems*, no. 40 in Classics in Applied Mathematics, SIAM, Philadelphia, second ed., Apr. 2002.

[38] B. Cockburn and C. Dawson, *Some extensions of the local discontinuous Galerkin method for convection-diffusion equations in multidi-*

mensions, ICES Report 99-27, Institute for Computational Engineering and Sciences, Austin, TX, Aug. 1999.

[39] B. Cockburn, S. Hou, and C.-W. Shu, *The Runge-Kutta local projection discontinuous Galerkin finite element method for conservation laws IV: The multidimensional case*, Math. Comput., 54 (1990), pp. 545–581.

[40] B. Cockburn, S.-Y. Lin, and C.-W. Shu, *TVB Runge-Kutta local projection discontinuous Galerkin finite element method for conservation laws III: One-dimensional systems*, J. Comput. Phys., 84 (1989), pp. 90–113.

[41] B. Cockburn and C.-W. Shu, *TVB Runge-Kutta local projection discontinuous Galerkin finite element method for conservation laws II: General framework*, Math. Comput., 52 (1989), pp. 411–435.

[42] ——, *The Runge-Kutta local projection $\mathcal{P}^1$-discontinuous-Galerkin finite element method for scalar conservation laws*, RAIRO Modél. Math. Anal. Numér., 25 (1991), pp. 337–361.

[43] ——, *The local discontinuous Galerkin method for time-dependent convection-diffusion systems*, SIAM J. Numer. Anal., 35 (1998), pp. 2440–2463.

[44] ——, *The Runge–Kutta discontinuous Galerkin method for conservation laws V: Multidimensional systems*, J. Comput. Phys., 141 (1998), pp. 199–224.

[45] M. B. Collins and P. S. Balson, *Coastal and shelf sediment transport: an introduction*, in Coastal and Shelf Sediment Transport, P. S.

Balson and M. B. Collins, eds., no. 274 in Geological Society Special Publications, The Geological Society, Bath, UK, 2007, pp. 1–5.

[46] G. Crasta and P. G. LeFloch, *Existence result for a class of nonconservative and nonstrictly hyperbolic systems*, Comm. Pure Appl. Anal., 1 (2002), pp. 513–530.

[47] N. Črnjarić-Žic, S. Vuković, and L. Sopta, *Extension of ENO and WENO schemes to one-dimensional sediment transport equations*, Comput. Fluids, 33 (2004), pp. 31–56.

[48] А. И. Вольперт, Пространства BV и квазилинейные уравнения, Математический Сборник, 73 (1967), pp. 225–267. In Russian.

[49] G. Dal Maso, P. G. LeFloch, and F. Murat, *Definition and weak stability of nonconservative products*, J. Math. Pures Appl., 74 (1995), pp. 483–548.

[50] G. H. Darwin, *Report of a committee, consisting of Professors G. H. Darwin and J. C. Adams, for the harmonic analysis of tidal observations*, Rep. Br. Assoc. Advmt. Sci., 53 (1884), pp. 49–117.

[51] C. Dawson et al., *Discontinuous Galerkin methods for modeling hurricane storm surge*, Adv. Water Resour., (2010). In press.

[52] C. Dawson and J. Proft, *Discontinuous and coupled continuous/discontinuous Galerkin methods for the shallow water equations*, Comput. Methods Appl. Mech. Engrg., 191 (2002), pp. 4721–4746.

[53] ——, *Discontinuous/continuous Galerkin methods for coupling the primitive and wave continuity equations of shallow water*, Comput. Methods Appl. Mech. Engrg., 192 (2003), pp. 5123–5145.

[54] ——, *Coupled discontinuous and continuous Galerkin finite element methods for the depth-integrated shallow water equations*, Comput. Methods Appl. Mech. Engrg., 193 (2004), pp. 289–318.

[55] A. de Chézy, *Formule pour trouver la vitesse de l'eau conduit dan une rigole donnée.* Dossier 847 (MS 1915), École National des Ponts et Chaussées, Paris, 1776. In French.

[56] P.-S. de la Place, *Recherches sur plusieurs points du système du monde*, Hist. Acad. Roy. Sci., 88 (1778), pp. 75–182. In French.

[57] ——, *Suite des recherches sur plusieurs points du système du monde*, Hist. Acad. Roy. Sci., 89 (1779), pp. 177–267, 525–552. In French.

[58] S. Dey, *Sediment pick-up for evolving scour near circular cylinders*, Appl. Math. Modell., 20 (1996), pp. 534–539.

[59] M. Dibajnia and A. Watanabe, *Sheet flow under nonlinear waves and currents*, in Proceedings of 23rd International Conference on Coastal Engineering, Venice, 1992, ASCE, pp. 2015–2029.

[60] J. Donat, *Über sohlangriff und geschiebetrieb*, Wasserwirtschaft, 26 (1929), pp. 27–36. In German.

[61] A. T. Doodson, *The harmonic development of the tide-generating potential*, Proc. R. Soc. Lond. A, 100 (1921), pp. 305–329.

[62] J. Douglas, B. L. Darlow, R. P. Kendall, and M. F. Wheeler, *Self-adaptive Galerkin methods for one-dimensional, two-phase immiscible flow*, in Proceedings 5th SPE Symposium on Reservoir Simulation (Denver), Dallas, 1979, Society of Petroleum Engineers, pp. 65–72.

[63] P. Du Boys, *Le Rhône et les rivières a lit affouillable*, Ann. Ponts Chaussées, 2 (1879), pp. 141–195. In French.

[64] C. Du Buat, *Principes d'Hydraulique, Vérifiés par un grand nombre d'Experiénces faites par ordre du Gouvernement*, Self-published, Paris, second ed., 1786. In French.

[65] M. Dubiner, *Spectral methods on triangles and other domains*, J. Sci. Comput., 6 (1991), pp. 345–390.

[66] J. Dupuit, *Traité Théorique et Pratique de la Conduite et de la Distribution des Eaux*, Carilian-Goeury et Vor Dalmont, Paris, 1854. In French.

[67] H. A. Einstein, *The bed-load function for sediment transportation in open channel flows*, Technical Bulletin 1026, USDA Soil Conservation Service, Washington, DC, Sept. 1950.

[68] L. Euler, *Principes généraux du mouvement des fluides*, Hist. Acad. Roy. Sci. Berlin, 11 (1757), pp. 274–315. In French.

[69] L. C. Evans, *Partial Differential Equations*, vol. 19 of Graduate Studies in Applied Mathematics, AMS, Providence, second ed., 2010.

[70] F. M. Exner, *Über die wechselwirkung zwischen wasser und geschiebe in flüssen*, Sitzungsber. Akad. Wiss. Wien, 134 (1925), pp. 165–203. In German.

[71] R. A. Falconer and P. H. Owens, *Numerical modelling of suspended sediment fluxes in estuarine waters*, Estuarine Coastal Shelf Sci., 31 (1990), pp. 745–762.

[72] W. Ferrel, *Tidal Researches (Appendix)*, US Coast Survey Report, Govt. Printing Office, Washington, DC, 1874.

[73] S. Fortier and F. C. Scobey, *Permissible canal velocities*, ASCE Trans., 89 (1926), pp. 940–956.

[74] L. Fraccarollo, H. Capart, and Y. Zech, *A Godunov method for the computation of erosional shallow water transients*, Int. J. Numer. Meth. Fluids, 41 (2003), pp. 951–976.

[75] J. Fredsøe and R. Deigaard, *Mechanics of Coastal Sediment Transport*, vol. 3 of Advanced Series on Ocean Engineering, World Scientific, Singapore, Apr. 1992.

[76] J. R. Garratt, *Review of drag coefficients over oceans and continents*, Mon. Weather Rev., 105 (1977), pp. 915–929.

[77] J. Gessler, *Der geschiebetriebbeginn bei mischungen untersucht an natürlichen abpflästerungserscheinungen in kanälen*, Mitteilungen der Versuchsanstalt für Wasserbau und Erdbau an der ETH in Zürich 69, ETH Zürich, Zürich, 1965. In German.

[78] S. Goldstein, *The forces on a solid body moving through viscous fluid*, Proc. R. Soc. Lond. A, 123 (1929), pp. 216–225.

[79] ——, *The steady flow of viscous fluid past a fixed spherical obstacle at small Reynolds numbers*, Proc. R. Soc. Lond. A, 123 (1929), pp. 225–235.

[80] W. H. Graf, *Hydraulics of Sediment Transport*, McGraw-Hill Series in Water Resources and Environmental Engineering, McGraw-Hill, New York, 1971.

[81] W. D. Grant and O. S. Madsen, *Combined wave and current interaction with a rough bottom*, J. Geophys. Res., 84 (1979), pp. 1797–1808.

[82] W. Hansen, *Theorie zur errechnung des wasserstandes und der strömungen in randmeeren nebst anwendungen*, Tellus, 8 (1956), pp. 287–300. In German, with English abstract.

[83] A. Harten, P. D. Lax, and B. van Leer, *On upstream differencing and Godunov-type schemes for hyperbolic conservation laws*, SIAM Rev., 25 (1983), pp. 35–61.

[84] M. C. Henderschott, *Evolution of Physical Oceanography: Scientific Surveys in Honor of Henry Stommel*, MIT Press, Cambridge, MA, 1981, ch. 10, pp. 292–341.

[85] F. M. Henderson, *Open Channel Flow*, no. 4 in Macmillan Series in Civil Engineering, Macmillan, New York, June 1966.

[86] F. Hjulström, *Studies of the morphological activity of rivers as illustrated by the River Fyris*, Bull. Geol. Inst. Upsala, 25 (1935), pp. 221–527.

[87] W. Huang, Q. Yang, and H. Xiao, *CFD modeling of scale effects on turbulence flow and scour around bridge piers*, Comput. Fluids, 38 (2009), pp. 1050–1058.

[88] J. Hudson and P. K. Sweby, *Formulations for numerically approximating hyperbolic systems governing sediment transport*, J. Sci. Comput., 19 (2003), pp. 225–252.

[89] ——, *A high-resolution scheme for the equations governing 2D bed-load sediment transport*, Int. J. Numer. Meth. Fluids, 47 (2005), pp. 1085–1091.

[90] J. John D. Anderson, *A History of Aerodynamics*, no. 8 in Cambridge Aerospace Series, Cambridge Univ. Press, Cambridge, UK, 1997.

[91] C. Johnson and J. Pitkäranta, *An analysis of the discontinuous Galerkin method for a scalar hyperbolic equation*, Math. Comput., 46 (1986), pp. 1–26.

[92] A. A. Kalinske, *Movement of sediment as bed load in rivers*, AGU Trans., 28 (1947), pp. 615–620.

[93] L. H. Kantha and C. A. Clayson, *Numerical Models of Oceans and Oceanic Processes*, vol. 66 of International Geophysics Series, Academic Press, San Diego, 2000.

[94] I. Kinnmark, *The Shallow Water Wave Equations: Formulation, Analysis, and Application*, vol. 15 of Lecture Notes in Engineering, Springer-Verlag, Berlin, Jan. 1986.

[95] I. P. E. Kinnmark and W. G. Gray, *An implicit wave equation model for the shallow water equations*, Adv. Water Resour., 7 (1984), pp. 168–171.

[96] J. A. Knauss, *Introduction to Physical Oceanography*, Prentice Hall, Upper Saddle River, NJ, second ed., 1996.

[97] D. E. Knuth, *Fundamental Algorithms*, vol. 1 of The Art of Computer Programming, Addison–Wesley, Reading, MA, third ed., 1997.

[98] N. Kobayashi, A. Payo, and B. D. Johnson, *Handbook of Coastal and Ocean Engineering*, World Scientific, Singapore, 2010, ch. 28, pp. 807–823.

[99] C. Koutitas and B. O'Connor, *Numerical modelling of suspended sediments*, Adv. Water Resour., 3 (1980), pp. 51–57.

[100] D. L. Kriebel and R. G. Dean, *Numerical simulation of time-dependent beach and dune erosion*, Coastal Eng., 9 (1985), pp. 221–245.

[101] E. J. Kubatko, *Development, Implementation, and Verification of hp-Discontinuous Galerkin Models for Shallow Water Hydrodynamics and Transport*, PhD thesis, University of Notre Dame, Notre Dame, IN, Dec. 2005.

[102] E. J. Kubatko, S. Bunya, C. Dawson, and J. J. Westerink, *Dynamic p-adaptive Runge–Kutta discontinuous Galerkin methods for the shallow water equations*, Comput. Methods Appl. Mech. Engrg., 198 (2009), pp. 1766–1774.

[103] E. J. Kubatko, S. Bunya, C. Dawson, J. J. Westerink, and C. Mirabito, *A performance comparison of continuous and discontinuous finite element shallow water models*, J. Sci. Comput., 40 (2009), pp. 315–339.

[104] E. J. Kubatko and J. J. Westerink, *Exact discontinuous solutions of Exner's bed evolution model: Simple theory for sediment bores*, J. Hydraul. Eng., 133 (2007), pp. 305–311.

[105] E. J. Kubatko, J. J. Westerink, and C. Dawson, *hp discontinuous Galerkin methods for advection dominated problems in shallow water flow*, Comput. Methods Appl. Mech. Engrg., 196 (2006), pp. 437–451.

[106] ——, *An unstructured grid morphodynamic model with a discontinuous Galerkin method for bed evolution*, Ocean Modelling, 15 (2006), pp. 71–89.

[107] E. W. Lane and A. A. Kalinske, *Engineering calculations of suspended sediment*, AGU Trans., 22 (1941), pp. 603–607.

[108] P. Lasaint and P.-A. Raviart, *On a finite element method for solving the neutron transport equation*, in Mathematical Aspects of Finite Elements in Partial Differential Equations, C. de Boor, ed., no. 33 in MRC Publications, Univ. of Wisc.–Madison, Academic Press, New York, Apr. 1974, pp. 89–123.

[109] P. D. Lax, *Hyperbolic Systems of Conservation Laws and the Mathematical Theory of Shock Waves*, vol. 11 of CBMS-NSF Regional Conference Series in Applied Mathematics, SIAM, Philadelphia, 1973.

[110] P. Le Floch, *Shock waves for nonlinear hyperbolic systems in nonconservative form*, IMA Preprint Series 593, IMA, Univ. of Minnesota, Minneapolis, Oct. 1989.

[111] ——, *An existence and uniqueness result for two nonstrictly hyperbolic systems*, in Nonlinear Evolution Equations that Change Type, B. L. Keyfitz and M. Shearer, eds., vol. 27 of The IMA Volumes in Mathematics and its Applications, Springer-Verlag, New York, 1990, pp. 126–138.

[112] P. Le Floch and T.-P. Liu, *Existence theory for nonlinear hyperbolic systems in nonconservative form*, Forum Math., 5 (1993), pp. 261–280.

[113] J. J. Leendertse, *Aspects of a computational model for long-period water-wave propagation*, Memorandum RM-5294-PR, The Rand Corp., Santa Monica, CA, May 1967.

[114] ——, *Aspects of SIMSYS2D: A system for two-dimensional flow computation*, Tech. Rep. R-3572-USGS, The Rand Corp., Santa Monica, CA, Dec. 1987.

[115] S. Leliavsky, *An Introduction to Fluvial Hydraulics*, Dover Publications, New York, 1955.

[116] J. P. Lepetit and A. Hauguel, *A numerical model for sediment transport*, in Marine Forecasting: Predictability and Modelling in Ocean Hydrodynamics: Proceedings of the 10th International Liège Colloquium on Ocean Hydrodynamics, J. C. J. Nihoul, ed., no. 25 in Elsevier Oceanography Series, New York, 1979, Elsevier, pp. 453–463.

[117] R. J. LeVeque, *Numerical Methods for Conservation Laws*, Lectures in mathematics ETH Zürich, Birkhäuser Verlag, Basel, Switzerland, second ed., 1992.

[118] ——, *Finite-Volume Methods for Hyperbolic Problems*, Cambridge texts in Applied Mathematics, Cambridge Univ. Press, Cambridge, UK, 2002.

[119] Q. Lin and A. H. Zhou, *Convergence of the discontinuous Galerkin method for a scalar hyperbolic equation*, Acta Math. Sci., 13 (1993), pp. 207–210.

[120] J.-L. Lions, *Problèmes aux limites non homogènes à donées irrégulières: Une méthode d'approximation*, in Numerical Analysis of Partial Differential Equations, J.-L. Lions, ed., Ispra, 1968, C.I.M.E., pp. 283–292. In French.

[121] J. H. List, A. S. Farris, and C. Sullivan, *Reversing storm hotspots on sandy beaches: Spatial and temporal characteristics*, Marine Geology, 226 (2006), pp. 261–279.

[122] X. Liu and M. H. García, *Three-dimensional numerical model with free surface and mesh deformation for local sediment scour*, J. Waterw. Port Coastal Ocean Eng., 134 (2008), pp. 203–217.

[123] X. Liu, B. J. Landry, and M. H. García, *Two-dimensional scour simulations based on coupled model of shallow water equations and sediment transport on unstructured meshes*, Coastal Eng., 55 (2008), pp. 800–810.

[124] W. Long, J. T. Kirby, and Z. Shao, *A numerical scheme for morphological bed level calculations*, Coastal Eng., 55 (2008), pp. 167–180.

[125] M. S. Longuet-Higgins and R. W. Stewart, *Radiation stresses in water waves; a physical discussion, with applications*, Deep-Sea Res., 11 (1964), pp. 529–562.

[126] R. A. Luettich, Jr., J. J. Westerink, and N. W. Scheffner, *ADCIRC: An advanced three-dimensional circulation model for shelves, coasts, and estuaries, Report 1: Theory and methodology of ADCIRC-2DDI and ADCIRC-3DL*, Dredging Research Program Tech. Rep. DRP-92-6, US Army Corps of Engineers, Vicksburg, MS, Nov. 1992.

[127] D. R. Lynch and W. G. Gray, *Analytic solutions for computer flow model testing*, J. Hydraul. Div., 104 (1978), pp. 1409–1428.

[128] O. Madsen and W. Grant, *Sediment transport in the coastal environment*, Technical Report 209, Massachusetts Institute of Technology, Cambridge, MA, 1976.

[129] R. Manning, *On the flow of water in open channels and pipes*, Transactions of the Institute of Civil Engineers of Ireland, 20 (1891), pp. 161–209.

[130] E. Meyer-Peter and R. Müller, *Formulas for bed-load transport*, in Proceedings of the Second Meeting of the IAHSR, Stockholm, June 1948, International Association for Hydraulic Structures Research, pp. 39–64.

[131] C. Mirabito, C. Dawson, and V. Aizinger, *An a priori error estimate for the local discontinuous Galerkin method applied to two-dimensional shallow water and morphodynamic flow*, Math. Comput., (2011). In review.

[132] C. Mirabito, C. Dawson, E. J. Kubatko, J. J. Westerink, and S. Bunya, *Implementation of a discontinuous Galerkin morphological model on two-dimensional unstructured meshes*, Comput. Methods Appl. Mech. Engrg., 200 (2011), pp. 189–207.

[133] C.-L. Navier, *Mémoire sur les lois du mouvement des fluides*, Mem. Acad. Sci. Inst. France, 6 (1827), pp. 389–440. In French.

[134] I. M. Navon, *FEUDX: A two-stage, high-accuracy, finite-element FORTRAN program for solving shallow-water equations*, Comput. Geosci., 13 (1987), pp. 255–285.

[135] U. Neumeier, C. Ferrarin, C. L. Amos, G. Umgiesser, and M. Z. Li, *Sedtrans05: An improved sediment-transport model for continental shelves and coastal waters with a new algorithm for cohesive sediments*, Comput. Geosci., 34 (2008), pp. 1223–1242.

[136] I. Newton, *De Motu Corporum*, vol. 1 of Philosophiæ Naturalis Principia Mathematica, The Royal Society, London, July 1687. In Latin.

[137] ——, *De Mundi Systemate*, vol. 3 of Philosophiæ Naturalis Principia Mathematica, The Royal Society, London, July 1687. In Latin.

[138] J. Nitsche, *Über ein variationsprinzip zur lösung von Dirichlet-problemen bei verwendung von teilräumen, die keinen randbedingungen unterworfen sind*, Abh. Math. Sem. Univ. Hamburg, 36 (1971), pp. 9–15. In German.

[139] M. P. O'Brien and B. D. Rindlaub, *The transportation of bed-load by streams*, AGU Trans., 15 (1934), pp. 593–603.

[140] C. W. Oseen, *Über die Stokes'sche formel, und über eine vermandte aufgabe in der hydrodynamik*, Arkiv för Matematik, Astronomi och Fysik, 6 (1910), pp. 1–20. In German.

[141] ——, *Neuere Methoden und Ergebnisse in der Hydrodynamik*, Akademische Verlagsgesellschaft, Leipzig, 1927. In German.

[142] C. Paola and V. R. Voller, *A generalized Exner equation for sediment mass balance*, J. Geophys. Res., 110 (2005).

[143] C. Parés, *Numerical methods for nonconservative hyperbolic systems: A theoretical framework*, SIAM J. Numer. Anal., 44 (2006), pp. 300–321.

[144] C. Parés and M. Castro, *On the well-balance property of Roe's method for nonconservative hyperbolic systems. Applications to shallow-water systems*, ESAIM: Math. Model. Numer. Anal., 38 (2004), pp. 821–852.

[145] P. W. Partridge and C. A. Brebbia, *Quadratic finite elements in shallow water problems*, J. Hydraul. Div., 102 (1976), pp. 1299–1313.

[146] T. E. Peterson, *A note on the convergence of the discontinuous Galerkin method for a scalar hyperbolic equation*, SIAM J. Numer. Anal., 28 (1991), pp. 133–140.

[147] G. W. Platzman, *The lattice structure of the finite-difference primitive and vorticity equations*, Mon. Weather Rev., 86 (1958), pp. 285–292.

[148] I. Proudman and J. R. A. Pearson, *Expansions at small Reynolds numbers for the flow past a sphere and a circular cylinder*, J. Fluid Mech., 2 (1957), pp. 237–262.

[149] W. H. Reed and T. R. Hill, *Triangular mesh methods for the neutron transport equation*, Technical Report LA-UR-73-479, Los Alamos Scientific Laboratory, Los Alamos, NM, 1973.

[150] O. Reynolds, *An experimental investigation of the circumstances which determine whether the motion of water shall be direct or sinuous, and of the law of resistance in parallel channels*, Philos. Trans. R. Soc. Lond., 174 (1883), pp. 935–982.

[151] ——, *On the dynamical theory of incompressible viscous fluids and the determination of the criterion*, Philos. Trans. R. Soc. Lond. A, 186 (1895), pp. 123–164.

[152] S. Rhebergen, *Discontinuous Galerkin Finite Element Methods for (Non)conservative Partial Differential Equations*, PhD thesis, University of Twente, Enschede, Neth., Feb. 2010.

[153] S. Rhebergen, O. Bokhove, and J. J. W. van der Vegt, *Discontinuous Galerkin finite element methods for hyperbolic nonconservative partial differential equations*, J. Comput. Phys., 227 (2008), pp. 1887–1922.

[154] J. S. Ribberink, *Bed-load transport for steady flows and unsteady oscillatory flows*, Coastal Eng., 34 (1998), pp. 59–82.

[155] G. R. Richter, *An optimal-order error estimate for the discontinuous Galerkin method*, Math. Comput., 50 (1988), pp. 75–88.

[156] P. L. Roe, *Approximate Riemann solvers, parameter vectors, and and difference schemes*, J. Comput. Phys., 43 (1981), pp. 357–372.

[157] J. Rottner, *A formula for bed-load transportation*, La Houille Blanche, 14 (1959), pp. 285–307.

[158] H. Rouse, *Modern conceptions of the mechanics of fluid turbulence*, ASCE Trans., 102 (1937), pp. 463–505.

[159] ——, *An analysis of sediment transportation in the light of fluid turbulence*, Report SCS-TP-25, USDA Soil Conservation Service, Washington, DC, July 1939.

[160] R. Saurel and R. Abgrall, *A multiphase Godunov method for compressible multifluid and multiphase flows*, J. Comput. Phys., 150 (1999), pp. 425–467.

[161] A. Schoklitsch, *Über Schleppkraft und Geschiebebewegung*, Engelmann, Leipzig, 1914. In German.

[162] A. Shields, *Anwendung der Aehnlichkeitsmechanik und der Turbulenzforschung auf die Geschiebebewegung*, PhD thesis, Preußischen Versuchsanstalt für Wasserbau und Schiffbau, Berlin, June 1936. In German.

[163] C.-W. Shu and S. Osher, *Efficient implementation of essentially non-oscillatory shock-capturing schemes*, J. Comput. Phys., 77 (1988), pp. 439–471.

[164] G. Simpson and S. Castelltort, *Coupled model of surface water flow, sediment transport and morphological evolution*, Comput. Geosci., 32 (2006), pp. 1600–1614.

[165] J. F. A. Sleath, *Sea Bed Mechanics*, Ocean Engineering, Wiley, New York, Sept. 1984.

[166] J. D. Smith, *Marine Modeling*, vol. 6, Wiley, New York, 1977, ch. 13, pp. 539–576.

[167] R. Soulsby, *Dynamics of Marine Sands, A Manual For Practical Applications*, Thomas Telford Publications, London, Jan. 1998.

[168] J. Steppeler, *FE2DY: A finite element FORTRAN program for the solution of the shallow-water equations with energy conservation*, Comput. Geosci., 16 (1990), pp. 645–667.

[169] G. G. Stokes, *On the theories of the internal friction of fluids in motion, and of the equilibrium and motion of elastic solids*, Trans. Cambridge Philos. Soc., 8 (1849), pp. 287–320.

[170] ——, *On the effect of the internal friction of fluids on the motion of pendulums*, Trans. Cambridge Philos. Soc., 9 (1856), pp. 8–106.

[171] J. P. M. Syvitski and J. M. Alcott, *RIVER3: Simulation of river discharge and sediment transport*, Comput. Geosci., 21 (1995), pp. 89–151.

[172] P. A. Tassi, S. Rhebergen, C. A. Vionnet, and O. Bokhove, *A discontinuous Galerkin finite element model for river bed evolution under shallow flows*, Comput. Methods Appl. Mech. Engrg., 197 (2008), pp. 2930–2947.

[173] C. Taylor and P. Hood, *A numerical solution of the Navier–Stokes equations using the finite element technique*, Comput. Fluids, 1 (1973), pp. 73–100.

[174] Texas Advanced Computing Center, *Lonestar (III) user guide*. World Wide Web, Feb. 2009.

[175] ——, *Lonestar (IV) user guide*. World Wide Web, Mar. 2011.

[176] The ROMS Group, *Regional ocean modeling system (ROMS)*. World Wide Web, July 2011.

[177] I. Toumi, *A weak formulation of Roe's approximate Riemann solver*, J. Comput. Phys., 102 (1992), pp. 360–373.

[178] I. Toumi and A. Kumbaro, *An approximate linearized Riemann solver for a two-fluid model*, J. Comput. Phys., 124 (1996), pp. 286–300.

[179] TU Delft, *The official SWAN home page*. World Wide Web, Mar. 2011.

[180] UNESCO, *Tenth Report of the joint panel on oceanographic tables and standards*, vol. 36 of UNESCO Technical Papers in Marine Science, UNESCO, Paris, 1981.

[181] J. Unger and W. H. Hager, *Down-flow and horseshoe vortex characteristics of sediment embedded bridge piers*, Exp. Fluids, 42 (2007), pp. 1–19.

[182] US Army Corps of Engineers, *ADH: Main page*. World Wide Web, July 2011.

[183] ——, *Services*. World Wide Web, Mar. 2011.

[184] ——, *STWAVE - STeady state spectral WAVE*. World Wide Web, Mar. 2011.

[185] L. C. van Rijn, *Prediction of dune erosion due to storms*, Coastal Eng., 56 (2009), pp. 441–457.

[186] V. A. Vanoni, ed., *Sedimentation Engineering*, no. 54 in ASCE Manuals and Reports on Engineering Practice, ASCE, Reston, VA, second ed., June 2006.

[187] C. B. Vreugdenhil, *Numerical Methods for Shallow-Water Flow*, no. 13 in Water Science and Technology Library, Klüwer, Dordrecht, 1994.

[188] J. M. Wahr, *Body tides on an elliptical, rotating, elastic and oceanless earth*, Geophys. J. R. Astr. Soc., 64 (1981), pp. 677–703.

[189] J. D. Wang and J. J. Connor, *Mathematical modeling of near coastal circulation*, Report MITSG 75-13, Massachusetts Institute of Technology, Cambridge, MA, Apr. 1975.

[190] M. F. Wheeler, *An elliptic collocation-finite element method with interior penalties*, SIAM J. Numer. Anal., 15 (1978), pp. 152–161.

[191] C. M. White, *The equilibrium of grains on the bed of a stream*, Proc. R. Soc. Lond. A, 174 (1940), pp. 322–338.

[192] Y. Xing and C.-W. Shu, *High order well-balanced finite volume WENO schemes and discontinuous Galerkin methods for a class of hyperbolic systems with source terms*, J. Comput. Phys., 214 (2006), pp. 567–598.

[193] Z. Xu, Y. Liu, and C.-W. Shu, *Hierarchical reconstruction for discontinuous Galerkin methods on unstructured grids with a WENO-type*

linear reconstruction and partial neighboring cells, J. Comput. Phys., 228 (2009), pp. 2194–2212.

[194] C. T. Yang, *Sediment Transport: Theory and Practice*, McGraw-Hill Series in Water Resources and Environmental Engineering, McGraw-Hill, New York, 1996.

Vita

Christopher Michael Mirabito graduated from Grafton High School in Grafton, Massachusetts in June 2002. He attended Carnegie Mellon University, where he received his Bachelor of Science degree in Mathematics in May 2006. The following fall, he began his graduate studies at the University of Texas at Austin. There he received his Master of Science degree in Computational and Applied Mathematics in December 2008. He began his research on discontinuous Galerkin methods applied to the shallow water equations and sediment transport in January 2007.

Email address: chris.mirabito35@gmail.com

This dissertation was typeset with LaTeX[†] by the author.

[†]LaTeX is a document preparation system developed by Leslie Lamport as a special version of Donald Knuth's TeX Program.